



**Calhoun: The NPS Institutional Archive**  
**DSpace Repository**

---

Theses and Dissertations

1. Thesis and Dissertation Collection, all items

---

2014-12

# Co-channel interference mitigation using satellite based receivers

Patterson, John E.

Monterey, California: Naval Postgraduate School

---

<http://hdl.handle.net/10945/44642>

---

This publication is a work of the U.S. Government as defined in Title 17, United States Code, Section 101. Copyright protection is not available for this work in the United States.

*Downloaded from NPS Archive: Calhoun*



Calhoun is the Naval Postgraduate School's public access digital repository for research materials and institutional publications created by the NPS community. Calhoun is named for Professor of Mathematics Guy K. Calhoun, NPS's first appointed -- and published -- scholarly author.

**Dudley Knox Library / Naval Postgraduate School**  
**411 Dyer Road / 1 University Circle**  
**Monterey, California USA 93943**

<http://www.nps.edu/library>



# **NAVAL POSTGRADUATE SCHOOL**

**MONTEREY, CALIFORNIA**

## **THESIS**

**CO-CHANNEL INTERFERENCE MITIGATION USING  
SATELLITE BASED RECEIVERS**

by

John E. Patterson

December 2014

Thesis Advisor:

Frank E. Kragh

Second Reader:

Herschel H. Loomis

Second Reader:

Ric Romero

**Approved for public release; distribution is unlimited**

THIS PAGE INTENTIONALLY LEFT BLANK

<b>REPORT DOCUMENTATION PAGE</b>			Form Approved OMB No. 0704-0188	
Public reporting burden for this collection of information is estimated to average 1 hour per response, including the time for reviewing instruction, searching existing data sources, gathering and maintaining the data needed, and completing and reviewing the collection of information. Send comments regarding this burden estimate or any other aspect of this collection of information, including suggestions for reducing this burden to Washington headquarters Services, Directorate for Information Operations and Reports, 1215 Jefferson Davis Highway, Suite 1204, Arlington, VA 22202-4302, and to the Office of Management and Budget, Paperwork Reduction Project (0704-0188) Washington DC 20503.				
1. AGENCY USE ONLY (Leave Blank)		2. REPORT DATE 12-19-2014		3. REPORT TYPE AND DATES COVERED Master's Thesis 07-02-2012 to 12-19-2014
4. TITLE AND SUBTITLE CO-CHANNEL INTERFERENCE MITIGATION USING SATELLITE BASED RECEIVERS			5. FUNDING NUMBERS	
6. AUTHOR(S) John E. Patterson				
7. PERFORMING ORGANIZATION NAME(S) AND ADDRESS(ES) Naval Postgraduate School Monterey, CA 93943			8. PERFORMING ORGANIZATION REPORT NUMBER	
9. SPONSORING / MONITORING AGENCY NAME(S) AND ADDRESS(ES) N/A			10. SPONSORING / MONITORING AGENCY REPORT NUMBER	
11. SUPPLEMENTARY NOTES  The views expressed in this document are those of the author and do not reflect the official policy or position of the Department of Defense or the U.S. Government. IRB Protocol Number: N/A.				
12a. DISTRIBUTION / AVAILABILITY STATEMENT Approved for public release; distribution is unlimited			12b. DISTRIBUTION CODE	
13. ABSTRACT (maximum 200 words)  This thesis investigates a means to mitigate co-channel interference from fourth generation cellular signals in order to support passive synthetic aperture radar (SAR) imaging using those same signals. Synthetic aperture radar is a staple of the military and intelligence communities, but the active transmission required for such images informs the target of the imaging process. Use of passive signals, such as the orthogonal frequency-division multiplexing (OFDM) signals of fourth generation cellular systems, is an attractive option, but co-channel interference mitigation is required. A method to separate the transmitted signals that leverages the estimated signal delays between multiple transmitters and receivers is examined for narrowband and wideband signals. Multiple methods of assessing recovery performance are proposed. The impact of noise is considered, as is the impact of collection geometry on recovery performance, and recovery of OFDM signals is evaluated. Signal interpolation is a critical element of the proposed recovery process, and two methods are compared for accuracy and speed of computation.				
14. SUBJECT TERMS Co-channel interference, orthogonal frequency-division multiplexing (OFDM), Passive Synthetic Aperture Radar, Interpolation			15. NUMBER OF PAGES 111	
			16. PRICE CODE	
17. SECURITY CLASSIFICATION OF REPORT Unclassified	18. SECURITY CLASSIFICATION OF THIS PAGE Unclassified	19. SECURITY CLASSIFICATION OF ABSTRACT Unclassified	20. LIMITATION OF ABSTRACT UU	

NSN 7540-01-280-5500

Standard Form 298 (Rev. 2-89)  
Prescribed by ANSI Std. Z39-18

THIS PAGE INTENTIONALLY LEFT BLANK

**Approved for public release; distribution is unlimited**

**CO-CHANNEL INTERFERENCE MITIGATION USING SATELLITE BASED  
RECEIVERS**

John E. Patterson  
Commander, United States Navy  
S.B., Massachusetts Institute of Technology, 1998

Submitted in partial fulfillment of the  
requirements for the degrees of

**ELECTRICAL ENGINEER**  
and  
**MASTER OF SCIENCE IN ELECTRICAL ENGINEERING**  
from the  
**NAVAL POSTGRADUATE SCHOOL**  
**December 2014**

Author: John E. Patterson

Approved by: Frank E. Kragh  
Thesis Advisor

Herschel H. Loomis  
Second Reader

Ric Romero  
Second Reader

Clark Robertson  
Chair, Department of Electrical and Computer Engineering

THIS PAGE INTENTIONALLY LEFT BLANK

## **ABSTRACT**

This thesis investigates a means to mitigate co-channel interference from fourth generation cellular signals in order to support passive synthetic aperture radar (SAR) imaging using those same signals. Synthetic aperture radar is a staple of the military and intelligence communities, but the active transmission required for such images informs the target of the imaging process. Use of passive signals, such as the orthogonal frequency-division multiplexing (OFDM) signals of fourth generation cellular systems, is an attractive option, but co-channel interference mitigation is required. A method to separate the transmitted signals that leverages the estimated signal delays between multiple transmitters and receivers is examined for narrowband and wideband signals. Multiple methods of assessing recovery performance are proposed. The impact of noise is considered, as is the impact of collection geometry on recovery performance, and recovery of OFDM signals is evaluated. Signal interpolation is a critical element of the proposed recovery process, and two methods are compared for accuracy and speed of computation.



THIS PAGE INTENTIONALLY LEFT BLANK

---

---

# Table of Contents

---

<b>1</b>	<b>Introduction</b>	<b>1</b>
1.1	Overview . . . . .	1
1.2	Literature Review and Prior Work. . . . .	3
1.3	Outline . . . . .	4
<b>2</b>	<b>Signal Recovery</b>	<b>7</b>
2.1	General Approach . . . . .	7
2.2	Geometry and Delay Overview . . . . .	9
2.3	Narrowband Evaluation. . . . .	10
2.4	Frequency Response Analysis . . . . .	17
2.5	Wideband Test . . . . .	25
2.6	Performance in the Presence of Noise . . . . .	28
<b>3</b>	<b>Recovery Using Orthogonal Frequency-Division Multiplexing Signals</b>	<b>31</b>
3.1	OFDM Signal Generation . . . . .	31
3.2	Recovery Performance with OFDM . . . . .	32
<b>4</b>	<b>Collection Geometry Analysis</b>	<b>37</b>
4.1	Geometry Assessment . . . . .	37
4.2	Layout Overview and Test Signal . . . . .	38
4.3	Results . . . . .	38
<b>5</b>	<b>Conclusion</b>	<b>45</b>
5.1	Summary of Results and Identified Limitations . . . . .	45
5.2	Future Work . . . . .	45
	<b>Appendix A Signal Interpolation</b>	<b>51</b>
A.1	Ideal Low Pass Filter Interpolation . . . . .	51
A.2	Fourier Phase Shifting for Interpolation . . . . .	56

A.3	Computation Time Comparison . . . . .	60
A.4	Summary . . . . .	60
<b>Appendix B Additional Analysis Tables and Figures</b>		<b>63</b>
B.1	OFDM Signal Recovery . . . . .	63
B.2	Geometry Analysis . . . . .	69
<b>Appendix C Code Listings</b>		<b>77</b>
C.1	delays_from_laydown.m . . . . .	77
C.2	block_deltas_from_delays.m. . . . .	77
C.3	calc_signals_nb.m . . . . .	78
C.4	recover_from_delays.m. . . . .	79
C.5	calc_signals_wb.m. . . . .	80
C.6	interp_time.m. . . . .	84
<b>List of References</b>		<b>85</b>
<b>Initial Distribution List</b>		<b>87</b>

---



---

## List of Figures

---

Figure 1	Overview of test geometry. . . . .	xix
Figure 2	Time domain of transmitted and recovered signals. . . . .	xxi
Figure 3	Frequency domain of transmitted and recovered signals. . . . .	xxi
Figure 4	Error of recovered signals. . . . .	xxii
Figure 1.1	Frequency reuse in adjacent cells. . . . .	3
Figure 2.1	Geometry determines the signal delay. . . . .	9
Figure 2.2	Frequency-domain plot of narrowband signals as transmitted and recovered, $f_1 = 32$ kHz. . . . .	15
Figure 2.3	Narrowband tests, transmitted and recovered signals. . . . .	16
Figure 2.4	Frequency-domain plot of narrowband signals as transmitted and recovered, $f_1 = 47,685$ Hz. . . . .	17
Figure 2.5	Delay analysis of the $f_1 = 32$ kHz signal. . . . .	19
Figure 2.6	Delay analysis of the $f_1 = 47.7$ kHz signal. . . . .	20
Figure 2.7	Delay analysis of the AWGN signal, $N = 32$ . . . . .	21
Figure 2.8	Delay analysis of the AWGN signal, $N = 2048$ . . . . .	22
Figure 2.9	Delay analysis of the AWGN signal, $N = 32$ , with zero-padding. . . . .	24
Figure 2.10	Delay analysis of the AWGN signal, $N = 2048$ , with zero-padding. . . . .	24
Figure 2.11	Wideband test signal, time domain. . . . .	28
Figure 2.12	Frequency domain of wideband test transmitted and recovered signals. . . . .	29
Figure 2.13	Error of recovered signals. . . . .	29
Figure 2.14	Recovery performance versus noise level. . . . .	30

Figure 3.1	OFDM test signal, time domain. . . . .	34
Figure 3.2	Frequency domain of OFDM test transmitted and recovered signals.	35
Figure 3.3	Error of recovered OFDM signals. . . . .	35
Figure 4.1	Overview of geometry test laydowns. . . . .	41
Figure 4.2	Geometry induced recovery errors, layout 1. . . . .	42
Figure 4.3	Geometry induced recovery errors, layout 2. . . . .	42
Figure 4.4	Geometry induced recovery errors, layout 3. . . . .	43
Figure 4.5	Geometry induced recovery errors, layout 4. . . . .	43
Figure 4.6	Geometry induced recovery errors, layout 5. . . . .	44
Figure A.1	Sampling a continuous time signal. . . . .	52
Figure A.2	Ideal low pass filter. . . . .	53
Figure A.3	Signal interpolation as a sum of scaled and shifted sinc() pulses. .	54
Figure A.4	Signals and error from shifting via interpolation. . . . .	56
Figure A.5	Signals and error from integer phase shifts in the frequency domain.	57
Figure A.6	Signals and error from fractional phase shifts in the frequency domain. . . . .	58
Figure A.7	Signals and error from fractional phase shifts with forced symmetry.	60
Figure B.1	OFDM test signal, time domain, parameter set 1. . . . .	63
Figure B.2	Frequency domain of OFDM test transmitted and recovered signals, parameter set 1. . . . .	63
Figure B.3	Error of recovered OFDM signals, parameter set 1. . . . .	64
Figure B.4	OFDM test signal, time domain, parameter set 2. . . . .	64
Figure B.5	Frequency domain of OFDM test transmitted and recovered signals, parameter set 2. . . . .	65

Figure B.6	Error of recovered OFDM signals, parameter set 2. . . . .	65
Figure B.7	OFDM test signal, time domain, parameter set 3. . . . .	66
Figure B.8	Frequency domain of OFDM test transmitted and recovered signals, parameter set 3. . . . .	66
Figure B.9	Error of recovered OFDM signals, parameter set 3. . . . .	67
Figure B.10	OFDM test signal, time domain, parameter set 4. . . . .	67
Figure B.11	Frequency domain of OFDM test transmitted and recovered signals, parameter set 4. . . . .	68
Figure B.12	Error of recovered OFDM signals, parameter set 4. . . . .	68
Figure B.13	Geometry induced recovery errors, layout 1. . . . .	70
Figure B.14	Geometry induced recovery errors, layout 2. . . . .	70
Figure B.15	Geometry induced recovery errors, layout 3. . . . .	71
Figure B.16	Geometry induced recovery errors, layout 4. . . . .	71
Figure B.17	Geometry induced recovery errors, layout 5. . . . .	71
Figure B.18	Frequency domain of recovered signals, layout 1. . . . .	72
Figure B.19	Frequency domain of recovered signals, layout 2. . . . .	72
Figure B.20	Frequency domain of recovered signals, layout 3. . . . .	73
Figure B.21	Frequency domain of recovered signals, layout 4. . . . .	73
Figure B.22	Frequency domain of recovered signals, layout 5. . . . .	73
Figure B.23	Time-domain signals and error, layout 1. . . . .	74
Figure B.24	Time-domain signals and error, layout 2. . . . .	74
Figure B.25	Time-domain signals and error, layout 3. . . . .	75
Figure B.26	Time-domain signals and error, layout 4. . . . .	75
Figure B.27	Time-domain signals and error, layout 5. . . . .	75

THIS PAGE INTENTIONALLY LEFT BLANK

---



---

## List of Tables

---

Table 1	Transmitter and receiver geometries. . . . .	xix
Table 2	OFDM test signal parameter summary. . . . .	xix
Table 3	Recovery performance figures. . . . .	xx
Table 2.1	Summary of geometry parameters. . . . .	11
Table 2.2	Signal and sampling parameters, narrowband tests. . . . .	12
Table 2.3	Performance figures for $f_1 = 32$ kHz. . . . .	15
Table 2.4	Performance figures for $f_1 = 47,685$ Hz. . . . .	17
Table 2.5	Frequency response test normalized phase errors. . . . .	25
Table 2.6	Signal and sampling parameters, wideband tests. . . . .	27
Table 2.7	Recovery performance figures for AWGN, $N = 2048$ . . . . .	28
Table 3.1	OFDM test signal parameter summary. . . . .	33
Table 3.2	Recovery performance figures for OFDM, set 1. . . . .	33
Table 3.3	Recovery performance figures for OFDM, set 2. . . . .	34
Table 3.4	Recovery performance figures for OFDM, set 3. . . . .	34
Table 3.5	Recovery performance figures for OFDM, set 4. . . . .	34
Table 4.1	Transmitter and receiver geometries, by layout. . . . .	39
Table 4.2	Geometry analysis test signal parameter summary. . . . .	39
Table 4.3	Correlation coefficient summary by layout number. . . . .	40
Table A.1	Energy summary for shifting via interpolation. . . . .	56
Table A.2	Energy summary for integer phase shifts in the frequency domain. . . . .	58



Table A.3	Energy summary for fractional phase shifts in the frequency domain.	58
Table A.4	Energy summary for fractional phase shifts with forced symmetry.	60
Table A.5	Calculation times for various shifting methods. . . . .	61
Table B.1	Recovery performance figures for layout 1. . . . .	69
Table B.2	Recovery performance figures for layout 2. . . . .	69
Table B.3	Recovery performance figures for layout 3. . . . .	69
Table B.4	Recovery performance figures for layout 4. . . . .	69
Table B.5	Recovery performance figures for layout 5. . . . .	70

---

## List of Acronyms and Abbreviations

---

<b>AWGN</b>	additive white Gaussian noise
<b>BSS</b>	blind source separation
<b>CFT</b>	continuous Fourier transform
<b>DFT</b>	discrete Fourier transform
<b>DTFT</b>	discrete time Fourier transform
<b>FDM</b>	frequency-division multiplexing
<b>FFT</b>	fast Fourier transform
<b>ICA</b>	independent component analysis
<b>IDFT</b>	inverse discrete Fourier transform
<b>IFFT</b>	inverse fast Fourier transform
<b>LTE</b>	long term evolution
<b>LTI</b>	linear time invariant
<b>OFDM</b>	orthogonal frequency-division multiplexing
<b>QPSK</b>	quadrature phase-shift keying
<b>SAR</b>	synthetic aperture radar
<b>SNR</b>	signal-to-noise ratio

THIS PAGE INTENTIONALLY LEFT BLANK

---

# Executive Summary

---

## Introduction

Imaging of the earth by synthetic aperture radar (SAR) provides a number of advantages over the more traditional electro-optical methods, as SAR operates without a requirement for daylight illumination of the target area and can image through clouds, providing visibility to targets that would not otherwise be possible to image [1]. Traditional monostatic SAR systems require illumination of the target area with a transmitter, which, in the case of military or intelligence targets, can serve to alert the target area to the imaging process. This affords the opportunity to shelter equipment or obscure the target area with an active radar jammer, negating some of the benefits of the SAR imaging approach [2].

Passive radar systems exploit signals that already exist in the target area, mitigating the warning provided by the monostatic SAR system [3]. The proliferation of fourth generation cellular communications networks coupled with the performance of their orthogonal frequency-division multiplexing (OFDM) waveform makes those transmitters an appealing source to exploit for passive SAR imaging.

Unfortunately, that same proliferation poses difficulty to the SAR imaging process from the satellite-based receivers in the form of co-channel interference. Cellular networks rely upon spatial frequency reuse in order to make the best possible use of the limited spectrum available. By dividing a larger geographic area into smaller cells and assigning each cell a subset of the available frequencies, it is possible to ensure that nearby cells do not reuse a particular frequency. Satellite-based receivers view many of these transmitters simultaneously, and a means other than line-of-sight is required to isolate the individual transmitter signals.

## Recovery Process

Consider a small system, consisting of two transmitters (transmitting the signals  $s_1(t)$  and  $s_2(t)$ ) and two receivers (which receive the signals  $r_1(t)$  and  $r_2(t)$ ). In that case, the signals

received are described by

$$r_1(t) = s_1(t - \tau_{11}) + s_2(t - \tau_{12}) \quad (1)$$

and

$$r_2(t) = s_1(t - \tau_{21}) + s_2(t - \tau_{22}), \quad (2)$$

where  $\tau_{mn}$  is the delay between transmitter  $n$  and receiver  $m$ . In the frequency domain, (1) and (2) become

$$R_1(f) = S_1(f)e^{-j\omega\tau_{11}} + S_2(f)e^{-j\omega\tau_{12}} \quad (3)$$

and

$$R_2(f) = S_1(f)e^{-j\omega\tau_{21}} + S_2(f)e^{-j\omega\tau_{22}}, \quad (4)$$

where  $S_n(f)$  and  $R_m(f)$  are the frequency-domain representations of  $s_n(t)$  and  $r_m(t)$ , respectively, and  $\omega = 2\pi f$ . Generalizing to a system of  $m$  receivers and  $n$  transmitters gives

$$\begin{bmatrix} e^{-j\omega\tau_{11}} & \dots & e^{-j\omega\tau_{1n}} \\ \vdots & \ddots & \vdots \\ e^{-j\omega\tau_{m1}} & \dots & e^{-j\omega\tau_{mn}} \end{bmatrix} \begin{bmatrix} S_1(f) \\ \vdots \\ S_n(f) \end{bmatrix} = \begin{bmatrix} R_1(f) \\ \vdots \\ R_m(f) \end{bmatrix}. \quad (5)$$

With an understanding of the delays  $\tau_{mn}$  between each transmitter and receiver, it is possible to solve (5) for the transmitted signals  $S_1(f) \dots S_n(f)$ . It is important to recognize that each element of (5) is a function of frequency and must be solved for each frequency. Application of the fast Fourier transform (FFT) to the sampled time-domain signals yields signal descriptions in the discrete frequency domain and facilitates this solution.

## OFDM Signal Recovery

A basic system of two receivers collecting the signals of two OFDM transmitters is adequate to demonstrate the potential recovery performance. The transmitter and receiver geometry is depicted in Figure 1, and the corresponding distances used to compute the signal propagation delays are provided in Table 1. The OFDM signal parameters for each of the transmitters are summarized in Table 2.

Table 1. Transmitter and receiver geometries. (In kilometers.)

Element	$x$	$y$	$alt$
Tx 1	0	0	0
Tx 2	0	30	0
Rx 1	146.2	0	400
Rx 2	146.2	50	400

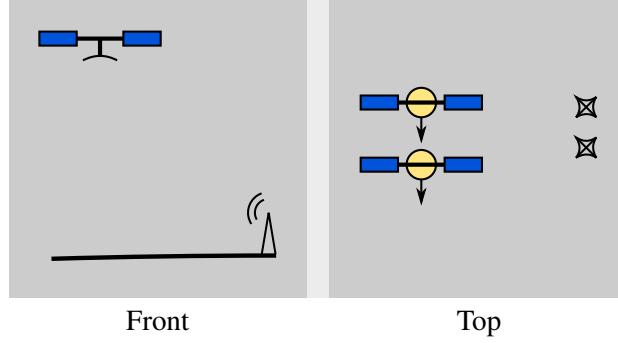


Figure 1. Overview of test geometry.

Table 2. OFDM test signal parameter summary.

	Value
Subcarriers	6
Modulation Scheme	QPSK
Bandwidth (kHz)	600
Symbols	16

In order to quantitatively assess recovery performance, the correlation coefficient

$$\chi(\hat{\mathbf{s}}, \mathbf{s}) = \frac{\hat{\mathbf{s}}^* \mathbf{s}}{\sqrt{P_{\hat{\mathbf{s}}} P_{\mathbf{s}}}} \quad (6)$$

is used to compare the original signal  $\mathbf{s}$  with the recovered signal  $\hat{\mathbf{s}}$ . The scalar product of two signals is a means of assessing the similarity of two signals [4]. The correlation coefficient normalizes the scalar product by signal powers, such that  $\chi()$  varies from -1 to 1, where a value of 1 indicates proportional signals, 0 indicates orthogonality, and -1 indicates proportional signals with different sign convention [5].

The correlation coefficients of the recovered signals are provided in Table 3 and indicate that the recovered signals are very closely matched to the original signals. A graphical

comparison of a subset of the time-domain samples of the original and recovered signals<sup>1</sup> is provided in Figure 2, and a frequency-domain comparison, a subset of the total signal spectrum, is provided in Figure 3. Both the time and frequency perspectives indicate excellent recovery performance. The frequency-domain perspective does indicate a discrepancy at the  $f = 0$  point, which is expected as the delay matrix in (5) is singular at that point.

Recovered signal error is computed using

$$\mathbf{S}_\delta = \mathbf{S} - \hat{\mathbf{S}} \quad (7)$$

in the frequency domain, where  $\mathbf{S}$  is the vector of original signal samples and  $\hat{\mathbf{S}}$  is a vector of the recovered signal samples. Similarly, time-domain error is computed using

$$\mathbf{s}_\delta = \mathbf{s} - \hat{\mathbf{s}}, \quad (8)$$

where  $\mathbf{s}$  and  $\hat{\mathbf{s}}$  are the time-domain samples of the original and recovered signals. Frequency- and time-domain recovery error plots are provided in Figure 4. Given the known singularity at  $f = 0$ , that point is omitted from the frequency-domain error plot. Both error plots indicate good recovery performance, with frequency-domain errors on the order of computer rounding error. The steady-state error in Figure 4b is likely a result of the singularity at  $f = 0$ .

## Conclusion

The above results show good correlation between the original and recovered signals. While additional work is required to ensure that the recovered signals sufficiently isolate desired signals from co-channel interference, the method appears to demonstrate the potential to support that isolation in a passive SAR system.

Table 3. Recovery performance figures.

	Correlation
Signal 1	$0.9995 - 4.6035 \times 10^{-16}i$
Signal 2	$0.9993 + 3.0037 \times 10^{-16}i$

---

<sup>1</sup> All signals are simulated and assumed to be either voltage or current. Units are unspecified in the figure.

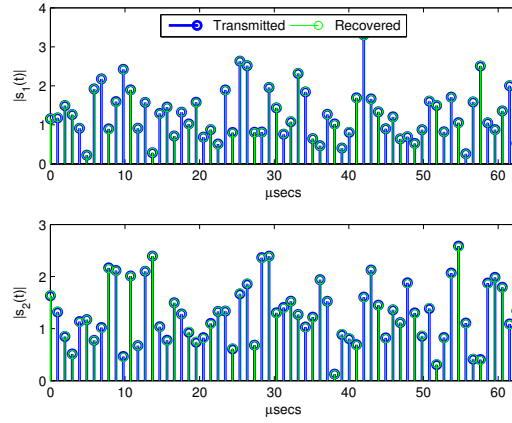
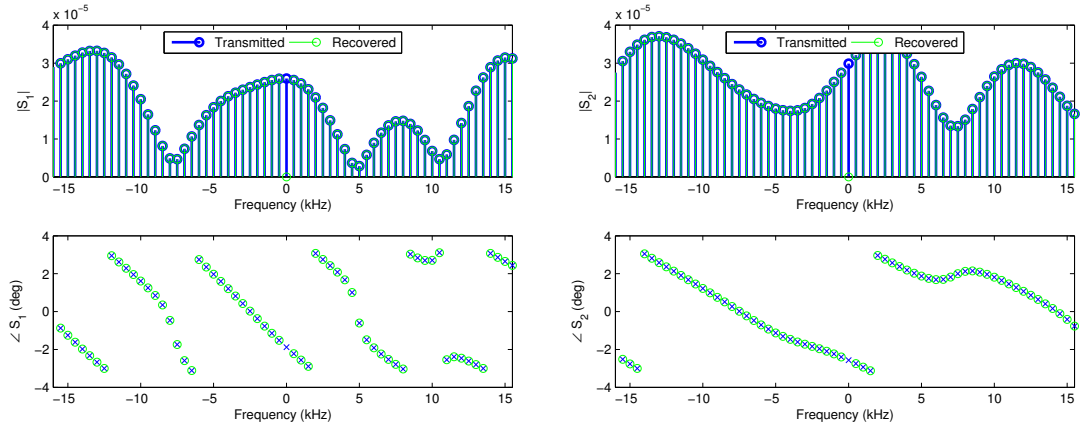


Figure 2. Time domain of transmitted and recovered signals.



(a) First signal

(b) Second signal

Figure 3. Frequency domain of transmitted and recovered signals.



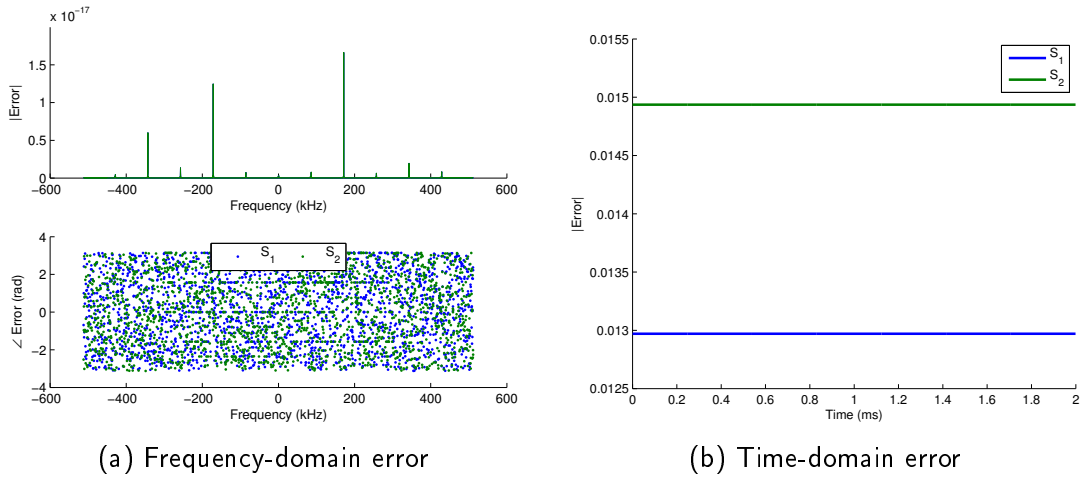


Figure 4. Error of recovered signals.

## List of References

- [1] American Society for Photogrammetry and Remote Sensing, *Manual of Remote Sensing*, 3rd ed., R. A. Ryerson, Ed. New York: J. Wiley, 1998.
- [2] M. I. Skolnik, *Radar Handbook*, 3rd ed. New York: McGraw-Hill, 2008.
- [3] J. R. Gutierrez del Arroyo, "Passive synthetic aperture radar imaging using commercial OFDM communication networks," Ph.D. dissertation, Graduate School Eng. Manage., Air Force Inst. Technology, Wright-Patterson Air Force Base, OH, 2012. [Online]. Available: <http://oai.dtic.mil/oai/oai?verb=getRecord&metadataPrefix=html&identifier=ADA564648>
- [4] A. B. Carlson, *Communication Systems: An Introduction to Signals and Noise in Electrical Communication*, 5th ed. Boston: McGraw-Hill, 2010.
- [5] A. Papoulis, *Probability, Random Variables, and Stochastic Processes*, 2nd ed. New York: McGraw-Hill, 1984.

---

# CHAPTER 1:

## Introduction

---

Synthetic aperture radar (SAR) imaging was conceived in 1951 by Carl Wiley, and the utility of the technique was quickly recognized. The early work in the field depended upon the ability to finely resolve the Doppler characteristics, or changes in the signal return due to the relative motion between radar and target, of the received radar signal [1]. Initial approaches relied upon optical processing techniques and utilized a variety of spherical, conical and cylindrical lenses to create the radar image [1]. Advances in modern computing and digital signal processing in the 1980s facilitated the more modern wavefront reconstruction techniques that commonly see use today [2]. SAR technological developments have facilitated a proliferation of SAR imaging systems including the Shuttle Imaging Radar (SIR-C/X-SAR) and Canada's RADARSAT mission, which are both examples of SAR satellites developed for Remote Sensing missions studying the earth [1]. Regardless of the ultimate use, SAR provides a unique means to monitor the earth that is capable of overcoming some considerable limitations of the more commonly known electro-optical systems. As an example, the study of tropical regions by remote sensing scientists was particularly hampered by cloud cover in those tropical regions as even after a decade of imaging with the electro-optical and infrared sensors on the LANDSAT satellites, there were still regions of the earth that had not been imaged without cloud cover [1]. SAR provides a means to collect useful data for those regions despite the near constant cloud coverage.

### 1.1 Overview

Much like the benefits afforded to the remote sensing community, SAR offers a number of advantages over electro-optical imaging systems to the military and intelligence communities. The ability to image a target area when obscured by clouds is of equal importance to the military and intelligence communities. The ability to image a target without a dependence on illumination from the sun allows targets to be monitored at all hours of the day.

Unfortunately, and unlike the imaging provided by electro-optical systems, the transmitter required for traditional monostatic SAR systems reveals the imaging process when that

signal is detected in the target area, affording the target the opportunity to employ countermeasures to prevent the imaging of sensitive target area information. In addition to sheltering equipment, the use of an active jammer when the SAR transmitter is detected might also preclude the successful imaging of the target area [3].

By exploiting transmissions that already exist in the target area, a passive SAR system mitigates some of the risks associated with operations targeting an adversary aware of the collection. Gutierrez del Arroyo [4] highlights a number of potential advantages of a passive SAR system, including both covertness and decreased susceptibility to electronic attack. The passive exploitation of existing signals necessitates a radar designed to operate with its receiver well separated from the transmitter. Radar systems that exhibit this separation between the radar transmitter and receiver are known as bistatic radars [5].

A variety of signal sources might be considered for use with such a passive SAR system. Two commercially developed systems, Lockheed Martin's Silent Sentry and Thales' Homeland Alerter 100, utilize analog FM-radio transmissions for the detection and tracking of aircraft. These are the first two known commercial systems to utilize passive radar techniques, and the random nature of the FM transmissions that they utilize as illuminators provides a signal processing challenge [4]. Orthogonal frequency-division multiplexing (OFDM) is a digital waveform that enjoys wide use in communications applications. It has also been proposed and extensively studied as a potential radar waveform, with a number of characteristics that make it well suited to the radar application [4], [6]. One of the more prevalent uses of the OFDM waveform is in fourth generation cellular communication networks including the IEEE 802.16 Wireless Metropolitan Area Networks compliant WiMax technology and long term evolution (LTE) [7], [8]. The proliferation of this signal coupled with the low range and doppler sidelobes of its ambiguity function makes it an excellent source for passive SAR imaging [9], [10].

That is not to say, however, that using OFDM-based cellular transmissions is without challenges. Fundamental to cellular technology is the concept of spatial frequency reuse. In order to support a large number of users with a limited amount of available spectrum, the cellular systems must make use of the same frequencies multiple times in a given geographic area. As explained in [11], a given coverage area is subdivided into cells (often modeled as hexagons, but much more irregular in reality). See Figure 1.1 for an illustration

of potential cell layouts. Each cell is assigned a subset of the available frequencies, such that no adjacent cells utilize the same frequencies. A frequency reuse distance is established such that co-channel interference does not impact the communication channel, and only outside of that distance from a cell may the frequencies be used again. This cellular allocation of frequencies facilitates an increased density of transmitters, which in turn allows the cell phones and transmitters to operate at lower power levels. This, in combination with line-of-sight limitations, mitigates interference between cells [12].

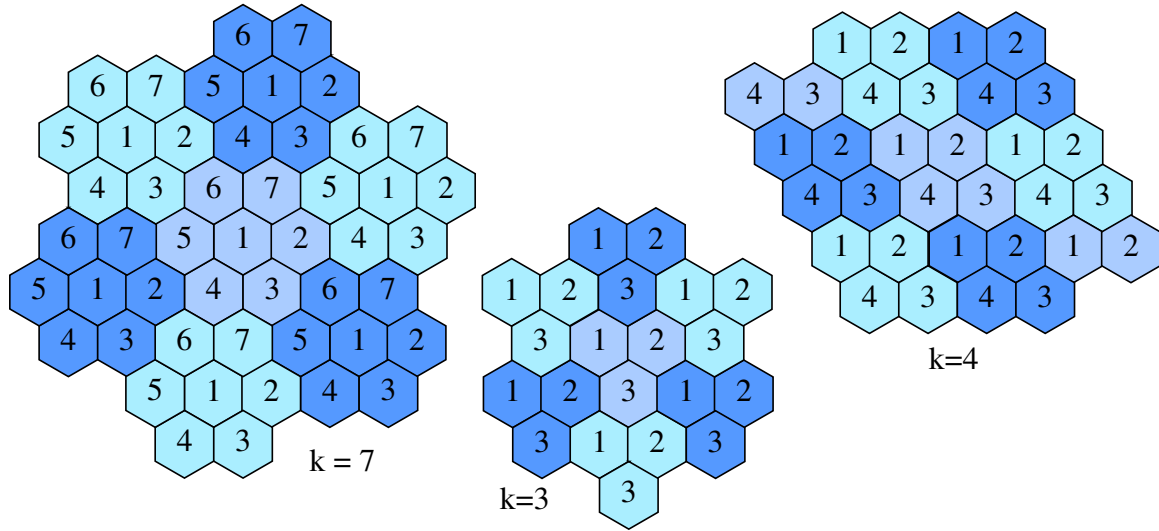


Figure 1.1. Frequency reuse in adjacent cells, after [11].

While spatial frequency reuse is a convenient way to maximize the utilization of the available spectrum, it poses a challenge to an asset attempting to use such a signal as an illuminator for a SAR image. The SAR image reconstruction process utilizes a matched filter and, therefore, requires a detailed understanding of the signal used as the illuminator for the image. It is likely that the signals from surrounding transmitters will also be received, presenting a co-channel interference issue that must be mitigated before the SAR image can be formed. That mitigation is the focus of this effort.

## 1.2 Literature Review and Prior Work

Levanon introduced the use of multi-carrier phase coded signals (now more commonly referred to as OFDM) and presented an analysis of their characteristics as a radar illuminator [10]. Gutierrez del Arroyo and Jackson have published a number of papers related to

the use of commercial transmitters as illuminators for passive SAR, including the development of a bistatic ambiguity function for WiMax emitters [9], collection and processing of WiMax transmissions for bistatic imaging [6], and analysis of the impact of WiMax-specific signal characteristics [4]. That work assumes that interference from neighboring cells is mitigated through network design, which is reasonable at low collection altitudes but becomes problematic with collections from higher altitude given the increased line-of-sight to numerous cells in the network.

Blind source separation (BSS) is a field dedicated to the recovery of original signals when numerous signals have been combined prior to receipt. There are a number of approaches to signal separation that might be applied to this problem. Stone presents an overview of one BSS approach known as independent component analysis (ICA) [13]. While some work in the BSS field has been with a limited number of receivers [14], the bulk of that research is for situations with equal numbers of transmitters and receivers as well as for real-valued signals, often from audio sources. Douglas has extended blind separation to complex valued signals [15], and many of the leading algorithms for blind source separation are collected in [16]. Those techniques often depend upon the non-Gaussianity of the original signals, and OFDM signals were not readily separated in initial attempts to apply those tools.

Fason [17] and Holder [18] developed a SAR model in MATLAB that can be used for analysis of various parameters that impact SAR performance. The work described in this thesis is intended as a precursor to the extension of that model to the bistatic case and performance analysis using recovered OFDM-based signals.

### **1.3 Outline**

An overview of the separation approach is provided in Chapter 2, including a description of the methods used for calculating the necessary signal delays. A number of signal recovery performance parameters are proposed, and separation is evaluated with both narrowband and wideband signals. The frequency response that results from delayed or shifted versions of those signals is evaluated. Recovery performance under noisy conditions is also evaluated.

A description of the OFDM signal model used is provided in Chapter 3 along with an

analysis of the recovery of a number of OFDM signals with various constituent parameters. That work is extended to several collection geometries in Chapter 4, and a means to evaluate potential collection geometries prior to signal collection in order to increase the likelihood of viable signal recovery is also discussed.

Results are summarized in Chapter 5, and a number of areas requiring further study are identified and discussed.

An analysis of two different methods of imposing a time delay on a sampled signal is provided in Appendix A. Figures detailing the results of the signal recovery efforts in Chapters 3 and 4 are provided in Appendix B. MATLAB functions that implement critical elements of the work described throughout this thesis are provided in Appendix C.

THIS PAGE INTENTIONALLY LEFT BLANK

---

## CHAPTER 2:

### Signal Recovery

---

Cellular technologies capitalize on line-of-sight limitations in order to use available spectrum efficiently. These line-of-sight limitations are negated when the receiver is elevated, with potential to receive multiple signals simultaneously. In many applications, use of those signals requires the ability to isolate a single transmission from a multitude of co-channel transmitters, often without detailed knowledge of the transmitted signals.

The main contribution of the work described in this thesis is a method to separate co-channel signals by leveraging the known positional information of both the transmitters and receivers to facilitate the recovery of the desired signal.

### 2.1 General Approach

Given a transmitter sending a signal  $s(t)$ , a receiver will receive  $r(t) = s(t - \tau)$ , where  $\tau$  is the delay due to propagation between the transmitter and receiver, a function of the distance and propagation rate of the intervening medium, and attenuation and noise effects are neglected. Considering a small system of two transmitters and two receivers, the signals received are

$$r_1(t) = s_1(t - \tau_{11}) + s_2(t - \tau_{12}) \quad (2.1)$$

and

$$r_2(t) = s_1(t - \tau_{21}) + s_2(t - \tau_{22}), \quad (2.2)$$

where  $\tau_{mn}$  represents the delay between receiver  $m$  and transmitter  $n$ . Any differences in signal losses across receivers are assumed to be negligible.

Applying the Fourier Transform to (2.1) and (2.2) gives

$$R_1(f) = S_1(f)e^{-j\omega\tau_{11}} + S_2(f)e^{-j\omega\tau_{12}} \quad (2.3)$$

and

$$R_2(f) = S_1(f)e^{-j\omega\tau_{21}} + S_2(f)e^{-j\omega\tau_{22}}, \quad (2.4)$$



where  $\omega = 2\pi f$  and  $S_n(f)$  and  $R_m(f)$  are the Fourier transforms of the transmitted and received signals, respectively. In matrix form, and extended for  $m$  receivers and  $n$  transmitters, (2.3) and (2.4) become

$$\begin{bmatrix} e^{-j\omega\tau_{11}} & \dots & e^{-j\omega\tau_{1n}} \\ \vdots & \ddots & \vdots \\ e^{-j\omega\tau_{m1}} & \dots & e^{-j\omega\tau_{mn}} \end{bmatrix} \begin{bmatrix} S_1(f) \\ \vdots \\ S_n(f) \end{bmatrix} = \begin{bmatrix} R_1(f) \\ \vdots \\ R_m(f) \end{bmatrix}. \quad (2.5)$$

Given adequate estimates of the delays  $\tau_{mn}$ , (2.5) can be viewed as the canonical  $\mathbf{Ax} = \mathbf{b}$  linear algebra problem for all points in  $f$ , where  $\mathbf{A}$  and  $\mathbf{b}$  are known, and linear algebra techniques can be applied to recover  $\mathbf{x}$ , which holds the frequency-domain description of each transmitted signal.

Working with sampled data of length  $N$ , the discrete Fourier transform (DFT), typically implemented via the fast Fourier transform (FFT), yields  $N$  frequency bins, with the frequency of each bin given by

$$\omega = 2\pi \frac{i-1}{N} f_s, \quad (2.6)$$

in radians per second (rad/sec), where  $i$  is the bin number and  $f_s$  is the sampling frequency, in Hertz (Hz). This means that there are  $N$  separate instances of (2.5) to solve. It is convenient to reshape the problem from  $N$  unique matrix equations to a single equation that incorporates all  $N$  frequencies. In that case, the exponential delay terms are arranged in  $m \times n$  blocks on the diagonal of a sparse matrix and (2.5) becomes

$$\begin{bmatrix} \mathbf{\Delta}(1) & & 0 \\ & \ddots & \\ 0 & & \mathbf{\Delta}(N) \end{bmatrix} \begin{bmatrix} \bar{\mathbf{S}}(1) \\ \vdots \\ \bar{\mathbf{S}}(N) \end{bmatrix} = \begin{bmatrix} \bar{\mathbf{R}}(1) \\ \vdots \\ \bar{\mathbf{R}}(N) \end{bmatrix}, \quad (2.7)$$

where

$$\mathbf{\Delta}(i) = \begin{bmatrix} e^{-j2\pi \frac{i-1}{N} f_s \tau_{11}} & \dots & e^{-j2\pi \frac{i-1}{N} f_s \tau_{1n}} \\ \vdots & \ddots & \vdots \\ e^{-j2\pi \frac{i-1}{N} f_s \tau_{m1}} & \dots & e^{-j2\pi \frac{i-1}{N} f_s \tau_{mn}} \end{bmatrix} \quad (2.8)$$

and  $\bar{\mathbf{S}}$  and  $\bar{\mathbf{R}}$  are column vectors of  $\bar{\mathbf{S}}(i) = [S_1(i) \dots S_n(i)]^T$  and  $\bar{\mathbf{R}}(i) = [R_1(i) \dots R_m(i)]^T$ .

For convenient reference, (2.7) is summarized as

$$\mathbf{\Delta S} = \mathbf{R} \quad (2.9)$$

where  $\mathbf{\Delta}$ , written without an index, refers to the complete set of  $\mathbf{\Delta}(i)$  blocks arranged on the diagonal, as in (2.7), while  $\mathbf{S}$  and  $\mathbf{R}$  are the complete columns of  $\tilde{\mathbf{S}}$  and  $\tilde{\mathbf{R}}$ , respectively.

## 2.2 Geometry and Delay Overview

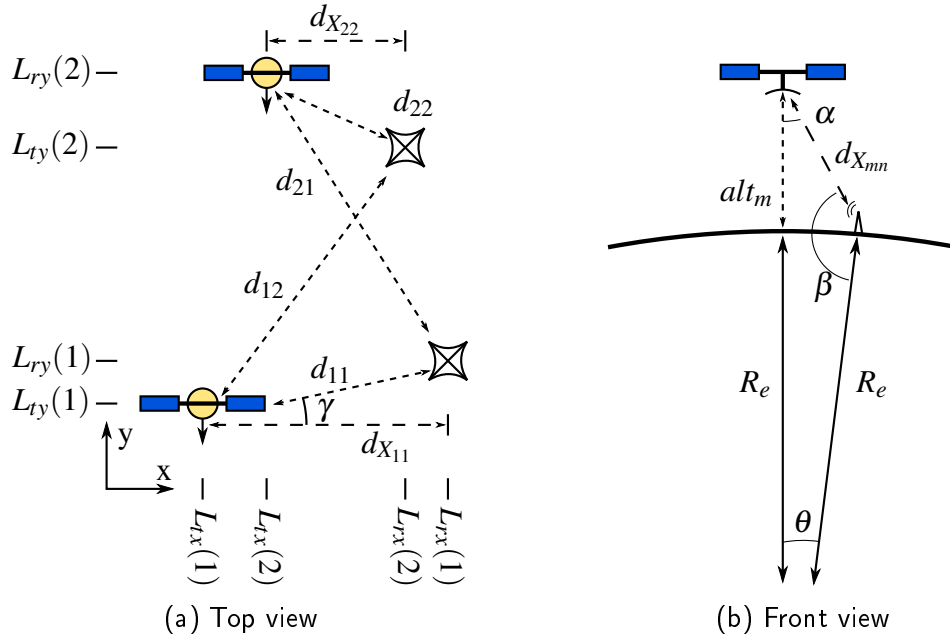


Figure 2.1. Geometry determines the signal delay.

The delay  $\tau$  in the above equations is the propagation delay, which is a function of the geometric relationship of the transmitters and receivers. An example configuration of two transmitters and two receivers is depicted in Figure 2.1, but this is readily extended to accommodate additional transmitters and receivers. For simplicity of the distance calculation, this configuration assumes that the receivers travel on parallel paths, though there is no requirement for such a geometry. The configuration measures transmitter and receiver location from an origin point and records those locations either in column vectors  $L_{rx}$  and  $L_{ry}$  for receivers or  $L_{tx}$  and  $L_{ty}$  for transmitters. The perpendicular slant distance between

the receiver path and transmitter  $d_{x_{mn}}$  is computed first, using the law of cosines as

$$d_{x_{mn}} = \sqrt{(alt_m + R_e)^2 + R_e^2 - 2(alt_m + R_e)R_e \cos(\theta)}, \quad (2.10)$$

where

$$\theta = \frac{L_{rx}(m) - L_{tx}(n)}{R_e} \quad (2.11)$$

is the interior angle between the receiver path and the transmitter location, as depicted in Figure 2.1b. With the perpendicular distance, the angle  $\gamma$  is defined by

$$\tan \gamma = \frac{L_{ry}(m) - L_{ty}(n)}{d_{x_{mn}}}, \quad (2.12)$$

and the desired distance  $d_{mn}$  can be determined using

$$\cos \gamma = \frac{d_{x_{mn}}}{d_{mn}}. \quad (2.13)$$

Substituting (2.12) into (2.13), the direct distance between the transmitter and receiver is provided by

$$d_{mn} = \frac{d_{x_{mn}}}{\cos \left[ \tan^{-1} \left( \frac{L_{ry}(m) - L_{ty}(n)}{d_{x_{mn}}} \right) \right]}. \quad (2.14)$$

The propagation delay is then calculated using  $\tau_{mn} = d_{mn}/c$ , where  $c$  is the speed of light. A MATLAB implementation of this approach is provided in Appendix C.1.

A straightforward solution to the canonical  $\mathbf{Ax} = \mathbf{b}$  problem requires an invertible  $\mathbf{A}$  matrix. In this scenario, that requires both a cooperative geometry and an equal number of transmitters and receivers. Geometry can be evaluated in advance, which should enable the identification and avoidance of unfavorable collection geometries. The approach is first evaluated in the  $m = n$  case, but the proliferation of transmitters coupled with the limited receiver assets makes the  $m < n$  condition worthy of additional consideration.

## 2.3 Narrowband Evaluation

For  $m = n$ , the transmitted signals can be recovered as long as the matrix of phase delays is invertible. Such a geometry was used to evaluate the approach using narrowband signals

in an effort to evaluate the validity of the approach.

### 2.3.1 Test Geometry

The values used in the following analysis are summarized in Table 2.1. The receiver locations along the  $x$ -axis were calculated to give a look angle  $\alpha$  of  $20^\circ$  from nadir. Locations along the  $y$ -axis were selected to avoid complementary delays. While such delays would have resulted in a delay matrix with orthogonal eigenvectors and simplified the analysis somewhat, that is not necessarily representative and was, therefore, avoided.

Table 2.1. Summary of geometry parameters.

Description	Parameter	Value
Number of transmitters	$n$	2
Number of receivers	$m$	2
Receiver altitude	$alt$	400 km
Earth radius	$R_e$	6371 km
Look angle from nadir	$\alpha$	$20^\circ$
Transmitter location (x)	$L_{tx}$	[ 0 0 ] km
Transmitter location (y)	$L_{ty}$	[ 0 30 ] km
Receiver location (x)	$L_{rx}$	[ 146.2 146.2 ] km
Receiver location (y)	$L_{ry}$	[ 0 50 ] km

The geometry calculations, as described in Section 2.2, and construction of the  $\Delta$  matrix defined in (2.8) were implemented in a MATLAB functions `delays_from_laydown()` and `block_deltas_from_delays()`, which are provided in Appendix C.1 and Appendix C.2.

### 2.3.2 Signal Generation and Recovery

Once the delays between transmitter and receiver pairs  $\tau_{mn}$  are established, it is possible to generate the test signals as both transmitted and received. The MATLAB function `calc_signals_nb()` is used to generate both the transmitted and received signals and is included in Appendix C.3. For the narrowband tests, signals were generated of the form

$$s_n(t) = A_n \cos(\omega_n t) \quad (2.15)$$

where  $A_n$  is the signal amplitude for the  $n$ th transmitter ( $A_n = 1$  for all of the cases discussed below) and  $\omega_n = 2\pi f_n$  is the corresponding signal frequency. For the first test, signals were selected that consisted solely of a single fundamental frequency of the Fourier transform

domain – that is, frequencies that conform to integer values of  $i$  in (2.6). In that case, an integer number of waveforms appears in the time-domain signal, and the frequency-domain representation has two non-zero values, corresponding to  $\pm\omega_n$ . That restriction was not applied to  $\omega_1$  in the second narrowband test described below. Specific parameters for each test are provided in Table 2.2. The transmitted signals were then sampled at  $F_s$ , and a corresponding frequency-domain set of samples was created using the FFT.

The sampled received signals can be constructed as the sum of the transmitted signals, appropriately delayed, while neglecting any attenuation, and ignoring any noise effects temporarily. As the transmitted signals are defined in continuous time, the delayed versions can be computed directly for each of the sample points. Each received signal is then

$$r_m(t) = \sum_{i=1}^n s_i(t - \tau_{mi}), \quad (2.16)$$

and the corresponding frequency-domain signal is computed with the FFT.

Table 2.2. Signal and sampling parameters, narrowband tests.

	Description	Parameter	Value
<b>Common</b>	Sampling frequency	$F_s$	1.024 MHz
	Number of samples	$N$	32
	Signal magnitude	$A_n$	1
<b>First NB Test</b>	Frequencies (Hz)	$f_1$	32,000
		$f_2$	187,500
<b>Second NB Test</b>	Frequencies (Hz)	$f_1$	47,685
		$f_2$	187,500

Having generated received signals that incorporate the properly delayed transmissions, it is possible to attempt recovery of the transmitted signals by solving (2.7) for  $\tilde{\mathbf{S}}$ . The MATLAB left-division operator is used to determine that solution in the `recover_from_delays()` function, included in Appendix C.4. Solving (2.7) yields the frequency-domain description of the transmitted signals. The corresponding time-domain signals are then computed using the inverse fast Fourier transform (IFFT).

### 2.3.3 Performance Evaluation

In addition to a qualitative comparison of the original and recovered signals in both the time and frequency domains, some quantitative assessment of the recovered signals is useful. Those methods are described here.

#### Power Angle

As the test signals used are real-valued, the recovered signals should share that property. By comparing the signal power contained in the real versus the imaginary part of the recovered signal, we can compute a power angle, the orientation of the signal power in the complex plane.

For a sampled signal, the power is given by

$$P = \frac{1}{N} \mathbf{s}^* \mathbf{s} \quad (2.17)$$

where  $N$  is the number of samples in the signal  $\mathbf{s}$ , which is a column vector, and  $\mathbf{s}^*$  is the conjugate transpose of the column, such that  $\mathbf{s}^* \mathbf{s}$  computes the inner product of the signal [19]. Signal power is composed of real and imaginary power. The angle of the power vector in the complex plane is given by

$$\Theta_p = \tan^{-1} \left( \frac{\Im\{\mathbf{s}\}^T \Im\{\mathbf{s}\}}{\Re\{\mathbf{s}\}^T \Re\{\mathbf{s}\}} \right) \quad (2.18)$$

where the real and imaginary parts of the signal are denoted with the  $\Re\{\}$  and  $\Im\{\}$  operators, respectively, and the length factors ( $1/N$ ) from (2.17) cancel. A  $\Theta_p$  or power angle (as referenced below) of zero indicates that the signal power is completely real. Non-zero values indicate that the recovery process resulted in a signal that has some amount of reactive power, which is unexpected, and serves as a first check of the recovered signal.

#### Error Figure

An understanding of the differences between the original and recovered signal is also a useful indicator of performance. Such an understanding is given by the energy or power of the difference between the two signals, particularly when normalized by the energy of the

original signal. This normalized error energy or error figure is given by

$$\text{Error Figure} = \frac{(\hat{\mathbf{s}} - \mathbf{s})^* (\hat{\mathbf{s}} - \mathbf{s})}{\mathbf{s}^* \mathbf{s}} \quad (2.19)$$

where  $\hat{\mathbf{s}}$  represents the recovered signal and  $\mathbf{s}$  the original signal [19]. Zero error figure indicates that there is no energy in  $(\hat{\mathbf{s}} - \mathbf{s})$  — that is, there is no energy in the recovered signal that was not in the original signal, which is the ideal case.

### Scalar Product or Correlation Coefficient

The similarity of two signals can be assessed by computing the scalar product, which is maximal when the signals are proportional [12]. Schwarz's inequality relates the scalar product to the signal powers, such that, in the case of transmitted and recovered signals,  $\mathbf{s}$  and  $\hat{\mathbf{s}}$ ,

$$\hat{\mathbf{s}}^* \mathbf{s} \leq \sqrt{P_{\hat{\mathbf{s}}} P_{\mathbf{s}}}, \quad (2.20)$$

where the power of the discrete time signal is given by (2.17). To facilitate comparison of signals with different power levels, it is desirable to normalize to unit power signals, such that

$$\chi(\hat{\mathbf{s}}, \mathbf{s}) = \frac{\hat{\mathbf{s}}^* \mathbf{s}}{\sqrt{P_{\hat{\mathbf{s}}} P_{\mathbf{s}}}}. \quad (2.21)$$

The correlation coefficient can vary from -1 to 1, where a value of 1 indicates proportional signals, 0 indicates the signals are orthogonal, and -1 indicates that the signals are proportional but with differing sign convention [20].

Carlson [12] identifies that the cross-correlation function is the scalar product of two signals with the second signal delayed by  $\tau$ , and the cross-correlation function measures the similarity of the two signals as a function of that delay. For purposes of this effort, we are interested in the correlation coefficient when  $\tau = 0$ , which corresponds to the scalar product. Signals are described as well correlated when the normalized scalar product approaches one, and correlation is assumed to be at  $\tau = 0$ .

### Subspace Angle

Taking a page from linear algebra, we imagine the sampled signals as vectors in  $N$ -dimensional space. Each vector describes a subspace contained within that  $N$ -dimensional

space. In that context, identical signals are parallel to each other, pointing in the same direction in that  $N$ -dimensional space. The angle between two such vectors is given by

$$\theta = \cos^{-1} \left( \frac{\hat{\mathbf{s}}^* \mathbf{s}}{\|\hat{\mathbf{s}}\| \|\mathbf{s}\|} \right) \quad (2.22)$$

where  $\|\cdot\|$  denotes the function that computes the length or 2-norm of a vector. A  $\theta = 0$  result indicates parallel vectors while a  $\theta = 90^\circ$  indicates completely orthogonal vectors.

Recognizing that  $P_s = \|\mathbf{s}\|^2/N = \mathbf{s}^* \mathbf{s}/N$  shows that subspace angle is the inverse cosine of the normalized scalar product. Throughout this document, the subspace angle is reported in degrees as an alternative perspective to the scalar product.

### 2.3.4 Results

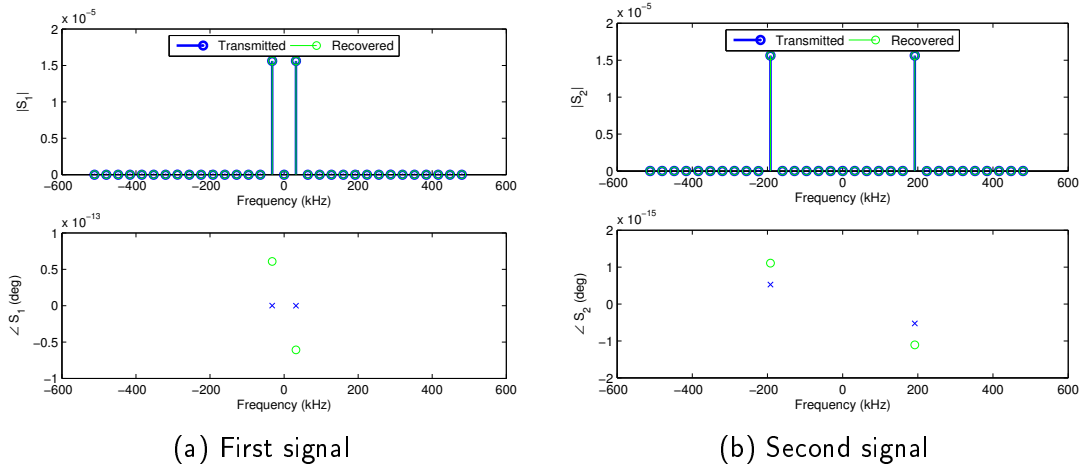


Figure 2.2. Frequency-domain plot of narrowband signals as transmitted and recovered,  $f_1 = 32$  kHz.

Table 2.3. Performance figures for  $f_1 = 32$  kHz.

	Signal 1	Signal 2
Power Angle ( $^\circ$ )	$5.1252 \times 10^{-29}$	$5.3304 \times 10^{-30}$
Error Figure	$1.5111 \times 10^{-26}$	$1.112 \times 10^{-26} + 1.7106 \times 10^{-43}i$
Subspace Angle ( $^\circ$ )	0	$1.8149 \times 10^{-14} - 1.8149 \times 10^{-14}i$
Correlation	1	$1 + 1.0033 \times 10^{-31}i$

The results of the first narrowband test indicate a very strong agreement between the transmitted signals and the numerically recovered transmitted signals. The frequency-domain



plots<sup>2</sup> (including both the magnitude and phase of each) of the transmitted and recovered signals for the first test, with  $f_1 = 32$  kHz, are provided in Figure 2.2. For clarity, the phase plots only include data points for those frequencies whose magnitude is at least 1% of the maximum value in the magnitude plot. Both recovered signals demonstrate good agreement with the transmitted signal, including very small phase error for the non-zero frequency components of the signal. The corresponding performance figures for this test are provided in Table 2.3. The power angle results show that each of the recovered signals is almost entirely real, with imaginary parts on the order of computer rounding error,  $\epsilon_{\text{machine}}$ . Similarly, this test yields very small error figures, indicating that there is very limited power difference between the two signals. Lastly, the angle between these two vectors, when imagined in  $N$ -dimensional space, is very nearly zero, indicating parallel vectors, which is the ideal case. Overall, this indicates that the technique has some promise, and a good correlation coefficient in the time domain is expected.

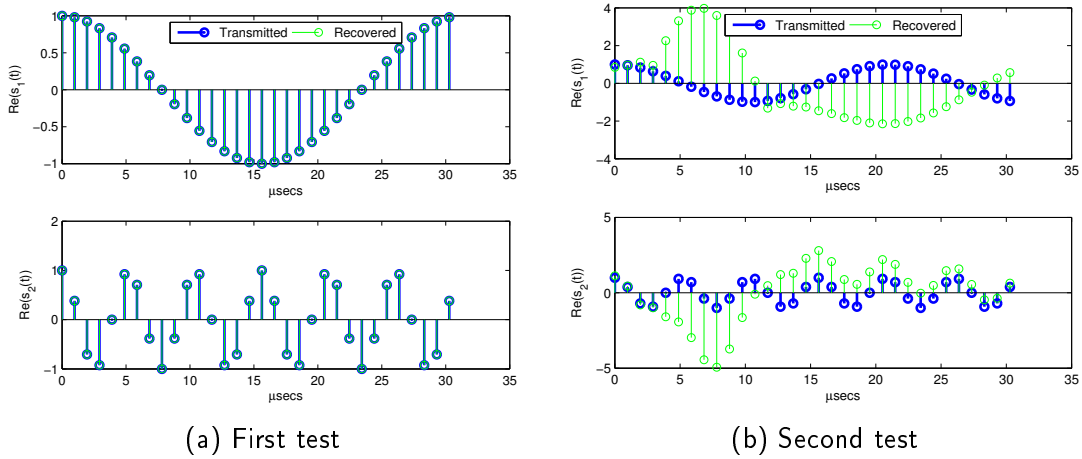


Figure 2.3. Narrowband tests, transmitted and recovered signals.

The time-domain results for the first narrowband test are provided in Figure 2.3a. As expected, the recovered signal is closely matched to the original signal. Similarly, the time-domain signal results from the second test, using  $f_1 = 47,685$  Hz are provided in Figure 2.3b. That case shows considerable disagreement between the original and recovered signals. Examination of the frequency-domain plots, provided in Figure 2.4, provide insight into the problem.

---

<sup>2</sup>All signals throughout the document are simulated and assumed to be either voltage or current. Units are left unspecified in all figures.

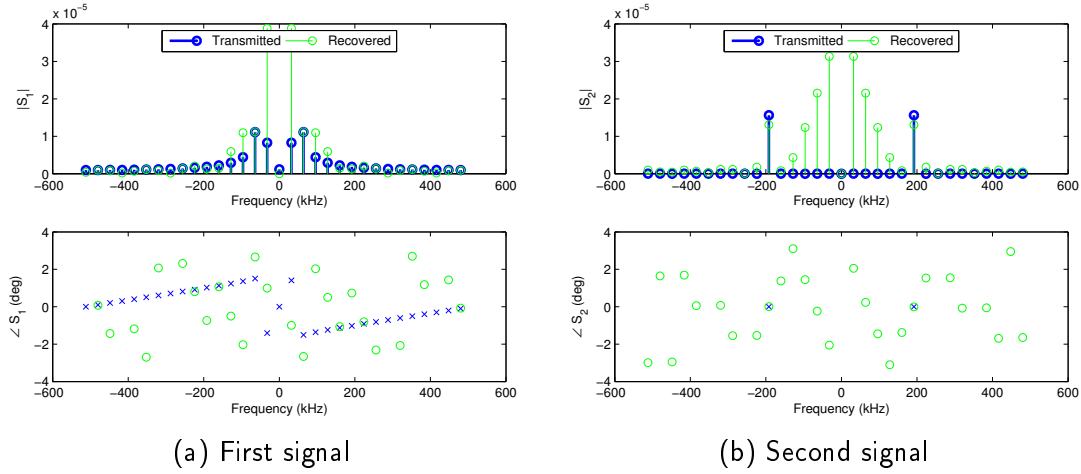


Figure 2.4. Frequency-domain plot of narrowband signals as transmitted and recovered,  $f_1 = 47,685$  Hz.

Table 2.4. Performance figures for  $f_1 = 47,685$  Hz.

	Signal 1	Signal 2
Power Angle ( $^\circ$ )	0.00213	0.0003375
Error Figure	10.34	6.676
Subspace Angle ( $^\circ$ )	$110.5 - 0.01644i$	$72.01 + 2.3432 \times 10^{-17}i$
Correlation	$-0.3497 + 0.0002688i$	$0.3088 - 3.8898 \times 10^{-19}i$

Unlike the first test, in the second test,  $f_1$  is transmitted as a sinusoid that maps onto many DFT indices, since  $f_1 \neq n/T_{\text{samp}}$  (where  $n$  is an integer), and this transmitted signal demonstrates a smooth phase throughout most of the spectrum. (Strum refers to this as *leakage* [21].) The recovered signal lacks this smooth phase, instead yielding a much more erratic phase. While the primary frequency of the second signal appears in the recovered version (though with reduced magnitude), there are a number of other frequency components present in the recovered version that are not present in the transmitted signal. The performance figures, provided in Table 2.4, also indicate poor recovery performance. While the power angle remains low (indicating real valued signals), the error figure, subspace angle, and correlation all indicate little agreement between the original and recovered signals.

## 2.4 Frequency Response Analysis

The approach outlined in Section 2.1 depends upon the fact that a known delay in the time domain translates to a predictable phase shift in the frequency domain and that the Fourier

Transform allows for transition between those domains. While these are known properties of the Fourier Transform, the results described above indicate that there are likely some details of those properties that were not adequately considered.

### 2.4.1 Frequency Response Definition

In order to study the necessary relationship, the delay was considered as a frequency response, such that

$$H(\omega) = \frac{\mathcal{F}[s(t - \tau)]}{\mathcal{F}[s(t)]} = e^{-j\omega\tau} \quad (2.23)$$

where  $\mathcal{F}[\cdot]$  represents the Fourier transform operation. By computing the FFT of a signal and a delayed copy, it is possible to compare the resulting frequency response with the expected  $e^{-j\omega\tau}$  result. As the approach outlined in Section 2.1 is focused on the phase relationships, the frequency response magnitude is less important. Any deviations from unit magnitude are canceled by the IFFT operation. The phase relationship is the critical component, as without a linear phase shift over varying frequency, the approach described in Section 2.1 breaks down quickly. For all of the tests below, the delay is  $\tau = 2T_{\text{samp}}$ , where  $T_{\text{samp}}$  is the sampling interval.

### 2.4.2 Fourier Transform Relationships

The delay property applied in (2.3) and (2.4) is a property of the continuous Fourier transform (CFT). For sampled data, a similar property exists for the discrete time Fourier transform (DTFT). When the sampled data is  $N$ -periodic, the DTFT can be simplified to the DFT, which the FFT implements efficiently and also shares a shifting property that yields a linear phase shift with frequency. The important characteristic of the DFT, however, is that the original samples must be  $N$ -periodic in order for it to be accurately applied in place of the DTFT. Ultimately, this requirement for  $N$ -periodic data means that the shifting property of the DFT is a circular shift [21]. For data that is not  $N$ -periodic, this difference yields a different phase response for the frequency response, and without somehow accounting for this difference, the above approach breaks down. These differences are illustrated below.

### 2.4.3 Narrowband Cases

A narrowband signal of the form described by (2.15) was generated with 32 sampled points. The magnitude and phase of the frequency response are provided in Figure 2.5 along with

a depiction of the signals with two different delay types. The first delay, labeled as “Continuous time shift” was generated by sampling a delayed continuous time signal, while the second delay, labeled as “Circular shift” was computed with a circular shift of the original signal. Both signals were delayed by two sample intervals. Frequency responses for both delay types as well as the ideal response ( $e^{-j\omega\tau}$ ) are provided in Figure 2.5a. Note that while not required in this case, later cases involve magnitude deviations from one on the order of machine error. For consistency, the magnitude plot is plotted as  $|H(\omega)| - 1$  to clearly depict those small deviations.

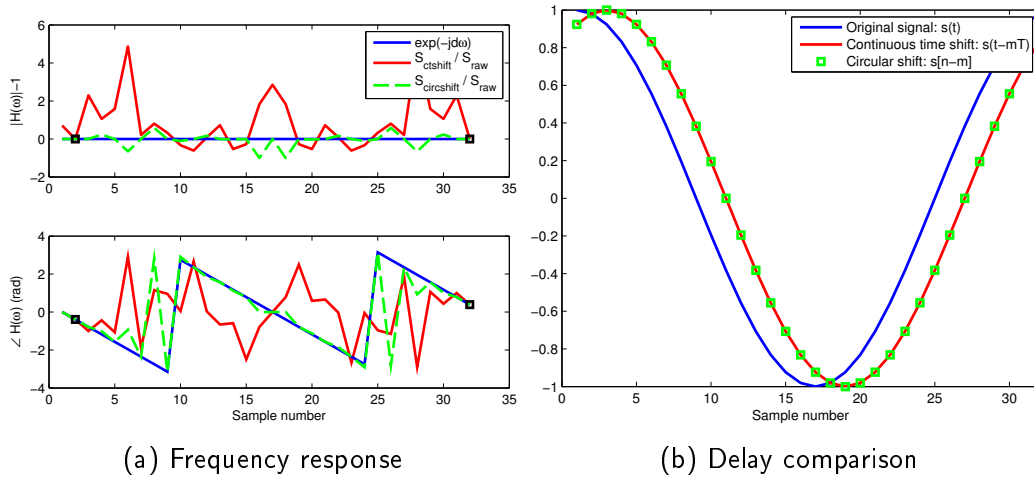


Figure 2.5. Delay analysis of the  $f_1 = 32$  kHz signal.

Recall from Section 2.3.4 that this signal provided excellent recovery performance. While the phase plot does not show good correlation between either of the frequency responses and the ideal response, it is important to recognize that in the frequency domain, ideally this signal has zero magnitude for all but two frequencies. When the frequency response is computed, both the dividend and divisor are approaching  $\epsilon_{machine}$  for all but these two frequencies, and the result shows considerable variation. The two frequencies with non-zero magnitude are marked with small squares, and each of these data points show good agreement across the two delay types and the expected frequency response. The time-domain view of the two delay types shows they yield similar results, as at this frequency and sample rate, the signal is  $N$ -periodic.

The second narrowband case, as shown previously, has a markedly poorer recovery perfor-

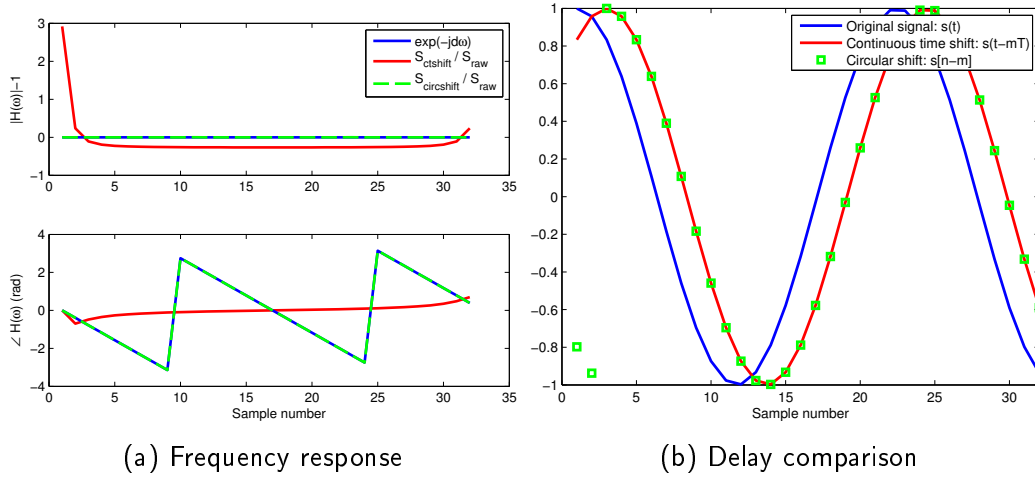


Figure 2.6. Delay analysis of the  $f_1 = 47.7$  kHz signal.

mance, and the frequency response analysis of that case, provided in Figure 2.6, illustrates the problem underlying that performance. As the time-domain signal in this case is not composed of a single component in the discrete frequency domain, the magnitude of the various frequencies is non-zero and, therefore, yields a much less erratic frequency response for both types of shifting. While the circular shift of the signal does appear well correlated with the ideal case, the signal that was shifted in the continuous time domain prior to sampling has a radically different frequency response, particularly with respect to the phase angle. The difference results from the fact that the signal is not  $N$ -periodic, which is clear from the difference in the shifted signals presented in Figure 2.6b. There, two samples (corresponding to the  $\tau = 2T_{\text{samp}}$  delay) of the discrete (or circular) shift are not correlated with the corresponding samples of the continuous time shifted signal. The delayed signals (as received) were generated using a time shift of a function defined in continuous time. A correct solution for  $\bar{\mathbf{S}}$  from (2.7) depends upon a phase shift that would have resulted from a circular shift vice a delay of the continuous time signal. An accurate recovery requires that the effects of the continuous time delay closely resemble those of a circular shift.

#### 2.4.4 Wideband Cases

For comparison to the narrowband case, a wideband test case was also conducted, using an additive white Gaussian noise (AWGN) signal. To facilitate a more direct comparison

between this and the narrowband case, this signal was also generated using 32 sampled values. As AWGN is not a time-dependent signal, the continuous time delay was created by prepending two samples of AWGN to the front of the signal, while the discrete time delay was computed using a circular shift, as in the narrowband case above. Using the same format as above, we provide transfer functions for both delay types as well as the ideal response ( $e^{-j\omega\tau}$ ) in Figure 2.7a. The time-domain plot of the three signals is provided in Figure 2.7b, and as in the second narrowband case, also exhibits two points in the circularly shifted signal that do not match those in the continuous time delayed signal. Despite that difference, the phase plot of Figure 2.7a shows that while the continuous time shift line does exhibit a few points of departure from the ideal and circular shift cases, there is generally much better agreement between the continuous time shift curve and the ideal case than in the narrowband cases, with the overall trend of the curve following that of the ideal curve. This indicates that a wider bandwidth signal might adequately support the signal recovery approach described above.

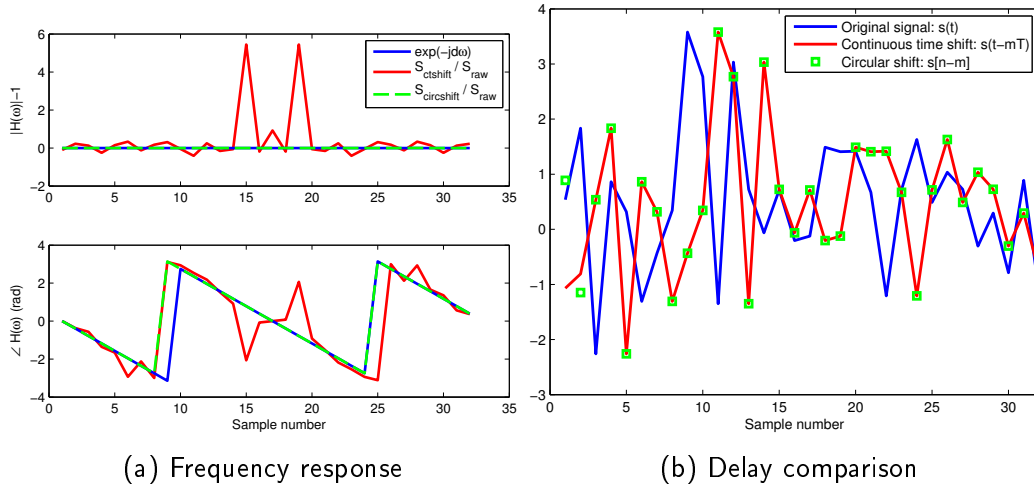


Figure 2.7. Delay analysis of the AWGN signal,  $N = 32$ .

The same test was repeated with additional samples to determine if the performance was a function of the number of samples of the AWGN signal. With additional samples, the number of samples that differ between the continuous delay and circular shift is a smaller fraction of the overall signal. An AWGN signal was generated using  $N = 2048$ , and the plots of the frequency response performance are provided in Figure 2.8a while Figure 2.8b depicts the first 32 samples of the complete time-domain signal in order to more clearly

show the two different points and the overall two-sample delay of the signals. While there is some phase noise present in the continuous time-shifted signal, it is important to recognize that this signal is plotted over the  $[-\pi, +\pi]$  interval which, in some cases, causes what might otherwise be a smaller error to appear more significant. Aside from this artifact, the continuous time plot does appear more closely aligned with the ideal case than any of the previous frequency response tests. This improvement is likely due to the larger number of samples. With more samples, the two points that are impacted by the shift differences are a much smaller fraction of the total signal and have little impact on the frequency response.

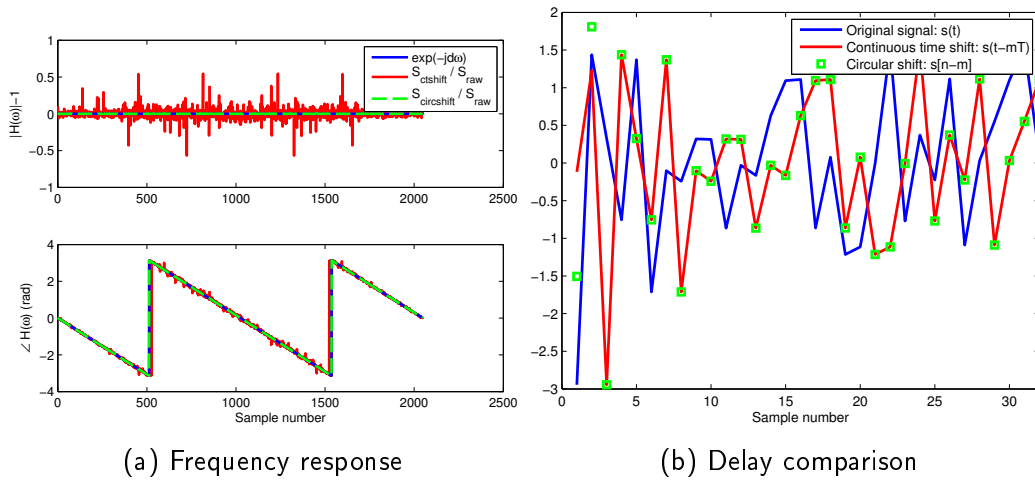


Figure 2.8. Delay analysis of the AWGN signal,  $N = 2048$ .

## 2.4.5 Zero Padding

To further improve the similarity between the delay that occurs in continuous time and the circular shift that is required to realize a  $e^{-j\omega\tau}$  phase shift in the frequency domain of the sampled signal, zero padding and windowing can be applied to the collected signal.

Intuitively, if a signal is transmitted for a limited period of time, a receiver receives no signal while the leading edge of the signal is propagating, and the signal arrives only after the propagation delay  $\tau$ . The causal nature of the linear time invariant (LTI) channel requires that the samples of the signal arrive in the same order in which they were transmitted. Without zero padding, the circular shift associated with that delay in the discrete time domain results in some fraction of the samples from the trailing edge of the signal shifting to the leading edge, which is not representative of the actual signal received after the delay.

By padding a time-limited signal with trailing zeros, the propagation delay results in some fraction of those zeros moving to the start of the signal rather than some portion of the trailing edge of the original signal, preserving the causal nature of the transmission and propagation delay.

Mathematically, for a sampled signal

$$x[n] = x(nT) \quad \text{for } n \in [0, N-1] \quad (2.24)$$

of duration  $N$  and integer sample numbers  $n$ , zero padding yields a signal

$$\bar{x}[n] = x(nT)I_{[0, N-1]}(n) \quad \text{for } n \in [0, N-1], \quad (2.25)$$

where

$$I_A[n] = \begin{cases} 1, & \text{if } n \in A \\ 0, & \text{otherwise} \end{cases} \quad (2.26)$$

is known as the indicator function and  $\bar{N}$  is the new length of the signal. Adequate zero padding requires

$$\bar{N} > \frac{T + \tau_d}{T_{\text{samp}}}, \quad (2.27)$$

where  $T$  is the duration of the signal,  $\tau_d$  is the propagation delay and  $T_{\text{samp}}$  is the sampling interval.

The proceeding evaluation of shifting types was repeated with zero padded AWGN signals for signal lengths of  $N = 32$  and  $N = 2048$ . The signal delay evaluated in this case is ideal, such that it is an integer number of samples, the transmitted signal is time-limited, and the delayed signal incorporates the complete transmitted signal. The comparison of the continuous time shift and circular shift are provided in Figure 2.9 for the  $N = 32$  case and Figure 2.10 for the  $N = 2048$  case. Regardless of signal length, the circular shift and continuous time delay are nearly identical, which demonstrates that under ideal conditions, the continuous time delay that results from signal propagation can be removed through either a circular shift in the discrete time domain or by multiplication of a phase shift in the frequency domain.



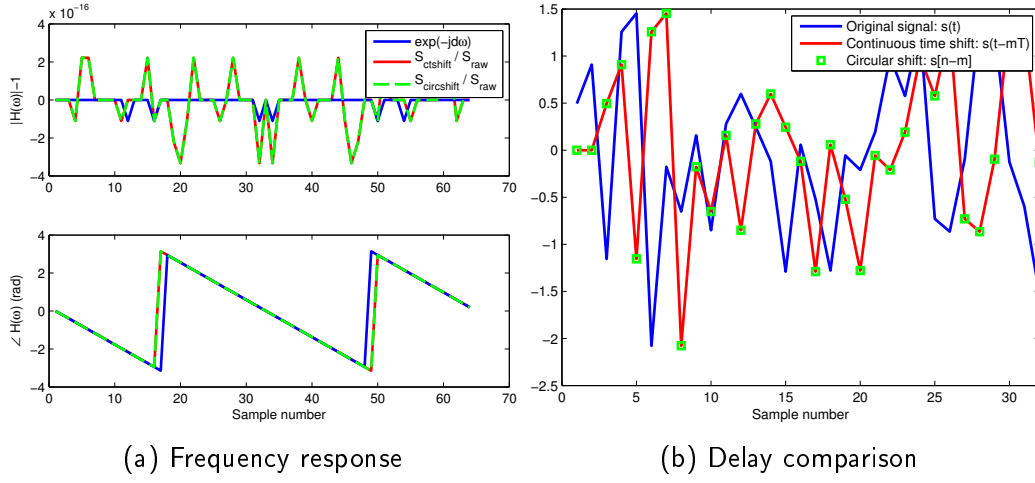


Figure 2.9. Delay analysis of the AWGN signal,  $N = 32$ , with zero-padding.

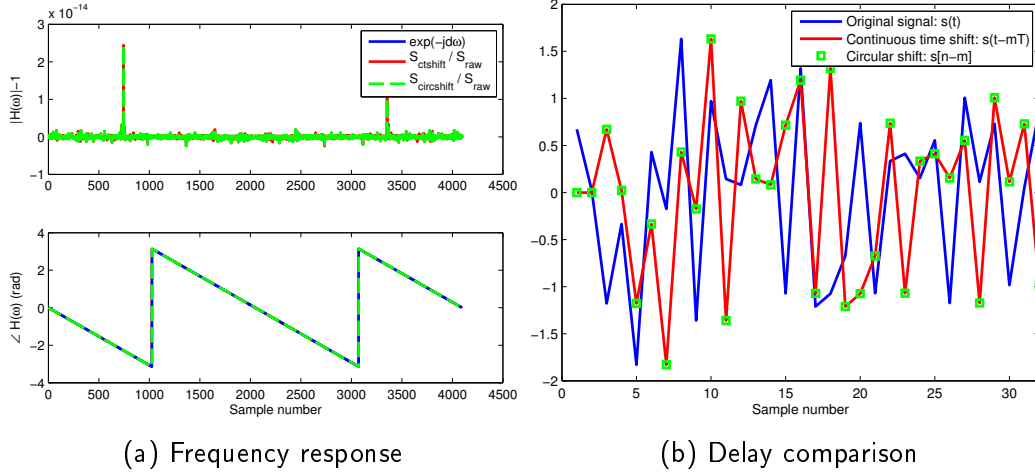


Figure 2.10. Delay analysis of the AWGN signal,  $N = 2048$ , with zero-padding.

## 2.4.6 Phase Error Calculation

Rather than rely simply upon a qualitative assessment, it is preferable to evaluate the phase errors described above quantitatively. For both the continuously shifted and circularly shifted signals, the normalized phase error is given by

$$\text{Phase Error} = \frac{\|\angle H(\omega) - \angle \bar{H}(\omega)\|}{\|\angle \bar{H}(\omega)\|} \quad (2.28)$$

where  $\angle H(\omega)$  is the phase angle of the frequency response for the shifted signal (either continuous time or circularly shifted) and  $\angle \bar{H}(\omega)$  is the phase angle of the ideal transfer function,  $\angle e^{-j\omega\tau} = -\omega\tau$ . Ideally, this phase error is zero. The phase angle results are presented in Table 2.5. Recall that in the narrowband case with  $f = 32$  kHz, both the delay approaches had considerable error as a result of the numerous frequencies with near zero response. Other than that case, the error for the circular shift approach is roughly  $\epsilon_{machine}$ , which confirms the graphical assessment above. For the continuous time delayed signals, in the narrowband cases, the phase error is approximately one, which indicates that the phase error is of the same magnitude as the ideal phase response itself. Some improvement is provided in the wideband,  $N = 32$  case, while the wideband,  $N = 2048$  case shows a considerable improvement, validating the use of additional points with an AWGN signal to mitigate the differences between the continuous and discrete time shifts. Once the signals are zero padded, the continuous time delay precisely mirrors the performance of the circular shift. It is important to recognize that the signals used in the zero padded cases were time limited at the transmitter, such that the initial samples of the received signals are zeros corresponding to the propagation delay and not samples of the signal that had been transmitted before  $t = 0$  at the transmitter.

Table 2.5. Frequency response test normalized phase errors.

	Circular	Continuous
Narrowband, $f = 32$ kHz	0.04727	1.054
Narrowband, $f = 47.7$ kHz	$1.5254 \times 10^{-16}$	1.017
Wideband, $N = 32$	$3.4068 \times 10^{-17}$	0.1097
Wideband, $N = 2048$	$7.6214 \times 10^{-17}$	0.007304
Wideband, $N = 32$ , zero-padded	$1.7453 \times 10^{-16}$	$1.7453 \times 10^{-16}$
Wideband, $N = 2048$ , zero-padded	$1.7632 \times 10^{-16}$	$1.7632 \times 10^{-16}$

## 2.5 Wideband Test

Having identified a signal that possesses the necessary phase relationship between the original signal and one that has been shifted in continuous time, we can evaluate the ability to recover that signal. For continuity, the test geometry remains as described in Section 2.3.1.

### 2.5.1 Signal Generation and Recovery

Sampled baseband AWGN signals were generated for each transmitter. The signals arrive at the different receivers with delays dependent upon the transmitter and geometry. As those delays are based on the specific geometry of the transmitters and receivers, they are not an integer multiple of the sampling interval, and a straightforward circular shift of the discrete time signals is inadequate to incorporate this precise delay. Two methods were considered to incorporate the appropriate delay into the transmitted signals — delay via phase shift in the frequency domain and interpolation of the sampled time-domain AWGN signals. A comparison of those methods is provided in Appendix A, and based upon that evaluation, the delay was applied via phase shift in the frequency domain of the transmitted signal given the small error and low computational complexity.

As discussed in Section 2.4.5, it was necessary to incorporate zero padding in the signals prior to computation of the FFT. The minimum padded signal length is given by (2.27), with  $\tau_d = \max(\tau_{mn})$ . In the interest of FFT computational speed, the signal was padded to the next largest power of two, such that

$$\bar{N} = 2^{\lceil \log_2 \left( \frac{T + \tau_d}{T_{\text{samp}}} \right) \rceil}, \quad (2.29)$$

where  $\lceil \cdot \rceil$  denotes the ceiling, or round up to the nearest integer, operation.

Given the unique copies of the signals with the appropriate delays for each transmitter/receiver pair, the complete received signal is constructed as

$$r_m[n] = \sum_{i=1}^{\ell} \mathcal{F}^{-1} \left\{ S[k] e^{-jk(2\pi/N)(F_s \tau_{mi})} \right\} \quad (2.30)$$

where  $\ell$  is the number of transmitters and  $n$  is the time-domain sample index number.

The MATLAB function `calc_signals_wb()` used for signal generation is provided in Appendix C.5, while the basic signal parameters used are provided in Table 2.6. It is important to note that the received signals constructed by `calc_signals_wb` are delayed copies of a time-limited transmission, as opposed to signals of infinite duration that are

sampled for a specific period in the receiver.<sup>3</sup>

Table 2.6. Signal and sampling parameters, wideband tests.

Description	Parameter	Value
Sampling frequency	$F_s$	1 MHz
Number of signal samples	$N$	2048
Padded signal length	$\bar{N}$	4096
Desired power spectral density	$S_n$	1 W / Hz

Recovery of the transmitted signals from those received is again accomplished by solving (2.7) for  $\bar{\mathbf{S}}$ .

### 2.5.2 Results

Given the large number of points in the transmitted signals, plots similar to those used in the narrowband test are less informative when assessing signal recovery performance. Instead, subsets of the time and frequency domains are provided in Figure 2.11 and Figure 2.12. These show excellent correlation between the two signals, with the exception of the  $f = 0$  points in both Figure 2.12a and Figure 2.12b. Those points are not recovered when solving (2.7) as the equation is singular at  $\Delta(1)$ , which corresponds to 0 Hz.<sup>4</sup> (See (2.8).) Error plots, depicting the difference between the original and recovered signals are presented in Figure 2.13. The recovery error in the frequency domain is

$$\mathbf{S}_\delta = \mathbf{S} - \hat{\mathbf{S}}, \quad (2.31)$$

where  $\mathbf{S}$  is the vector of frequency-domain samples of the original signal and  $\hat{\mathbf{S}}$  is a vector of the frequency-domain samples obtained by the recovery process. Note that in the frequency domain, the error at  $f = 0$  has been omitted from the plot due to the known discrepancy of the recovery process. The recovery error in the time domain is

$$\mathbf{s}_\delta = \mathbf{s} - \hat{\mathbf{s}}, \quad (2.32)$$

where  $\mathbf{s}$  and  $\hat{\mathbf{s}}$  are the vectors of the time-domain samples of the original and recovered signals, respectively.

<sup>3</sup>See Section 5.2 for further discussion.

<sup>4</sup>In the case of both WiMax and LTE, this point corresponds to the DC subcarrier, which both standards specify should be null. The recovery process simply sets this point to zero [7], [22].

The performance metrics identified in Section 2.3.3 are provided in Table 2.7. Note the small Power Angle, Error Figure and Subspace Angle figures, and the correlation coefficient very near one. These all indicate good recovery performance.

Table 2.7. Recovery performance figures for AWGN,  $N = 2048$ .

	Signal 1	Signal 2
Power Angle ( $^\circ$ )	$2.0427 \times 10^{-26}$	$2.073 \times 10^{-26}$
Error Figure	$6.0921 \times 10^{-5}$	$0.0001202 - 1.0917 \times 10^{-44}i$
Subspace Angle ( $^\circ$ )	$0.4472 - 4.263 \times 10^{-12}i$	$0.6283 - 1.6754 \times 10^{-12}i$
Correlation	$1 + 5.8073 \times 10^{-16}i$	$0.9999 + 3.2064 \times 10^{-16}i$

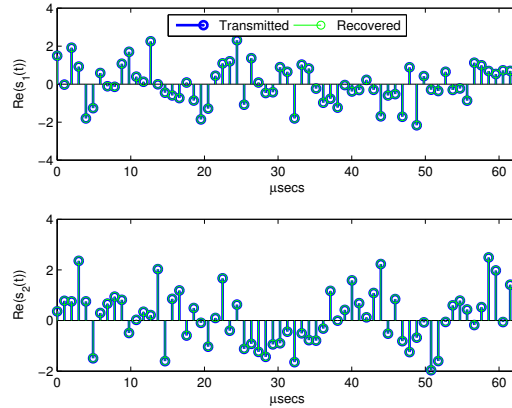


Figure 2.11. Wideband test signal, time domain.

## 2.6 Performance in the Presence of Noise

To be a useful technique, the process described in Section 2.1 must demonstrate reasonable performance in the presence of noise. To evaluate the performance with noise, the above wideband signal test using AWGN signals was repeated with varying levels of AWGN noise at the receivers. No filtering was applied to either the AWGN signal or the AWGN noise.

As above, received signals were constructed using (2.30) with  $\tau_{mn}$  determined by the same transmitter and receiver geometry described in Section 2.3.1. Noise signals  $\eta_m$  were constructed for each receiver as real valued random samples of a Gaussian distribution and scaled by the standard deviation of the samples in order to ensure unit variance of the sampled noise signals.

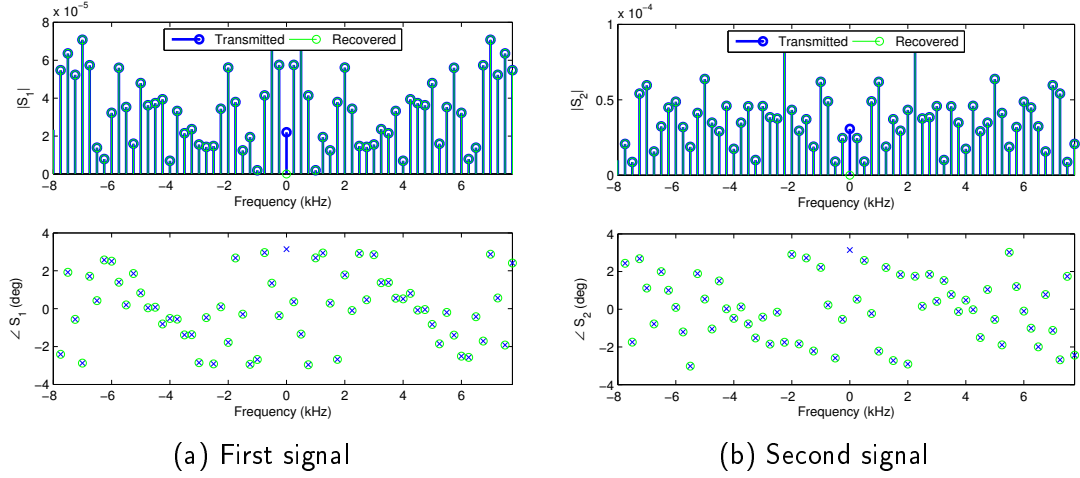


Figure 2.12. Frequency domain of wideband test transmitted and recovered signals.

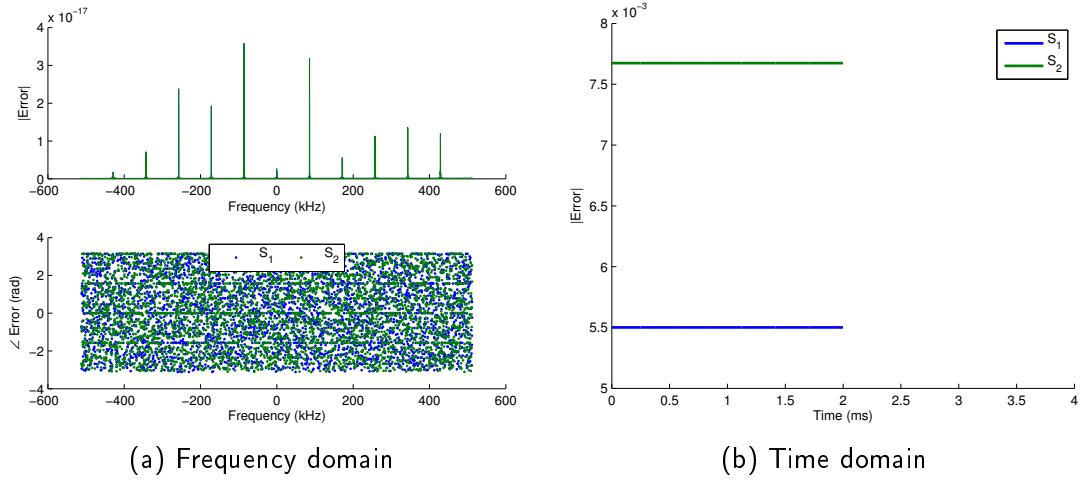


Figure 2.13. Error of recovered signals.

At each signal-to-noise ratio (SNR) test point, the necessary noise power level was computed as

$$\sigma^2 = \frac{P_r}{10^{\text{SNR}/10}}, \quad (2.33)$$

where  $P_r$  is the power in the received signal and the desired SNR level is in decibels (dB). The received signal, at the desired SNR, is

$$\check{r}_m = r_m + \sigma \eta_m. \quad (2.34)$$

The signal recovery process described above was performed and the correlation coefficient between the original and recovered signals  $\chi(\hat{s}, s)$  plotted vs SNR in Figure 2.14. Some performance degradation is expected, as the recovery process solves  $\Delta S = \check{R}$  for the signals  $S$ , while with noise,  $\Delta S + \eta = \check{R}$  is a more accurate model of the received signals. The approach described in Section 2.1 makes no provision for identifying or eliminating noise, and, therefore, even under ideal performance conditions, the recovered signals are noisy versions of the original signals. To facilitate an understanding of how the recovery process compares to what might be considered the ideal case, Figure 2.14 includes curves for the correlation coefficient of the original signal with a noisy version of that signal  $\chi(\check{s}, s)$ , annotated in the legend as “Original”, where

$$\check{s}_m = s_m + \sigma \eta_m. \quad (2.35)$$

As this is intended only to show the impact of noise on the correlation coefficient, there was no attempt to include this noise in the propagation model.

This data indicates that for comparable signal correlation coefficients, the recovery process requires roughly 35 dB higher SNR than is necessary if the recovery process is not utilized. This is a considerable performance degradation, and without mitigation, may limit the utility of this approach. See Section 5.2 for a discussion of means to both assess this performance impact and potential means to mitigate this degradation. Prior to expending the effort to improve performance in the presence of noise, the recovery method should be tested with the OFDM signals used by fourth generation communication systems.

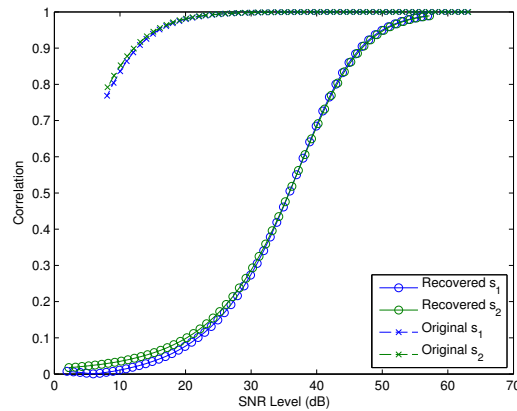


Figure 2.14. Recovery performance versus noise level.

---

## CHAPTER 3:

# Recovery Using Orthogonal Frequency-Division Multiplexing Signals

---

In order to be useful as a co-channel interference mitigation approach, it is necessary to ensure that the process outlined above provides adequate performance with representative signals. OFDM is central to both LTE and WiMax technologies which offer promise as illuminators for a passive SAR imaging process. A brief introduction to the OFDM signal and an assessment of recovery performance with OFDM signals is presented below.

### 3.1 OFDM Signal Generation

Fundamentally, OFDM can be considered an extension of frequency-division multiplexing (FDM). While FDM suffers from the potential for interference between carriers on difference frequencies (due to non-ideal filters), OFDM avoids this with the use of orthogonal frequencies, such that for a symbol duration  $T$  and subcarrier frequencies  $f_k$  [12]

$$\int_0^T \cos(2\pi f_k t) \cos(2\pi f_j t) dt = 0 \quad \forall j, k \text{ where } j \neq k. \quad (3.1)$$

Given the trigonometric identity

$$\cos \theta \cos \phi = \frac{1}{2} [\cos(\theta - \phi) + \cos(\theta + \phi)], \quad (3.2)$$

(3.1) can be rewritten as

$$\int_0^T \cos[2\pi t(f_k - f_j)] + \cos[2\pi t(f_k + f_j)] dt = 0 \quad \forall j, k \text{ where } j \neq k. \quad (3.3)$$

By selecting  $f_{k+1} - f_k = \Delta f = 1/T$ , the  $f_k - f_j$  and  $f_k + f_j$  terms are an integer multiple of  $\Delta f$ , the integrals are zero over the  $[0, T]$  interval and the frequencies are orthogonal.

The signal that represents a single OFDM symbol is assembled from a series of  $K$  subcarriers. Each subcarrier is a sequence of symbols to be transmitted, either from independent



sources or a selection of  $K$  symbols to be transmitted simultaneously from a single stream of data. Each subcarrier is independently modulated (e.g., by using quadrature phase-shift keying (QPSK)) to produce  $K$  streams of complex data  $X_k[n]$ . For a given OFDM symbol, a data element from each subcarrier is further modulated at an orthogonal frequency  $f_k$  and combined with the other modulated subcarrier signals, as in

$$w[n] = \sum_{k=0}^{K-1} X_k[n] e^{j2\pi f_k n} \quad n = 0, 1, \dots, K-1. \quad (3.4)$$

The inverse discrete Fourier transform (IDFT) provides a convenient and elegant means to implement this modulation scheme (see [12] for a detailed discussion), such that

$$w[n] = \text{IDFT}\{X_k[n]\}. \quad (3.5)$$

The total OFDM signal bandwidth is

$$B = K\Delta f. \quad (3.6)$$

## 3.2 Recovery Performance with OFDM

Baseband timelimited OFDM signals were generated using code adapted from the work by Holder [18]. The parameters for each set of test signals are provided in Table 3.1. (Note that the bandwidth listed there is a two-sided bandwidth.) Those signals were delayed and combined as discussed in Section 2.5.1, using the transmitter and receiver geometry detailed in Table 2.1. For consistency with the preceding discussions, the OFDM signals were interpolated and resampled at 1.024 MHz. Relatively low bandwidth OFDM signals (as compared to LTE and WiMax) were used for testing to keep the number of samples required for the signal delay reasonable at this sampling rate. See Section 5.2 for alternative approaches.

Recovery of the transmitted signals was performed by solving (2.7) for  $\bar{S}$ . Results of the recovery process are provided in Table 3.2 through Table 3.5. Note that the OFDM signals are not generally real-valued, and a non-zero power angle is not indicative of a recovery shortfall. A power angle near  $45^\circ$  indicates comparable real and imaginary parts of the

Table 3.1. OFDM test signal parameter summary.

	Set 1	Set 2	Set 3	Set 4
Subcarriers	6	128	128	128
Modulation Scheme	QPSK	QPSK	QPSK	BPSK
Bandwidth (kHz)	600	600	1000	1000
OFDM Symbols	16	4	4	10

signal, which is expected with the OFDM signals. Subsets of the signals from the first parameter set depicted in the time and frequency domains are provided in Figure 3.1 and Figure 3.2. Qualitatively, these indicate good recovery performance with the recovered signal plotted at the same points as the original signal. The singularity at  $f = 0$  Hz is apparent in the frequency-domain plots. Time- and frequency-domain plots of recovery error from the first set of signals are provided in Figure 3.3. The frequency-domain error indicates recovery errors on the order of machine error, with a few exceptional frequencies that have slightly more error than most. The steady-state error in the time domain is likely the result of the singularity at  $f = 0$  Hz. Each set of OFDM parameters demonstrated comparable performance, with some minor differences that are likely the result of the random signal content rather than a function of one of the OFDM parameters. The complete set of OFDM recovery performance plots are provided in Section B.1. This consistent and accurate recovery performance suggests that the method is likely functional across a large collection of OFDM-based signals, including LTE and WiMax transmissions. It is important to recognize that this performance was examined in a single arrangement of transmitters and receivers. As it is useful to understand the potential impact of collection geometry on recovery performance, this is explored further in the following chapter.

Table 3.2. Recovery performance figures for OFDM, set 1.

	Signal 1	Signal 2
Power Angle ( $^{\circ}$ )	47.39	35.82
Error Figure	$0.001054 + 7.7941 \times 10^{-29}i$	$0.001404 - 2.8107 \times 10^{-30}i$
Subspace Angle ( $^{\circ}$ )	$1.86 + 8.1252 \times 10^{-13}i$	$2.147 - 4.5929 \times 10^{-13}i$
Correlation	$0.9995 - 4.6035 \times 10^{-16}i$	$0.9993 + 3.0037 \times 10^{-16}i$

Table 3.3. Recovery performance figures for OFDM, set 2.

	Signal 1	Signal 2
Power Angle (°)	45.45	44.38
Error Figure	$0.0004209 - 1.6937 \times 10^{-28}i$	$0.0004143 + 2.4529 \times 10^{-28}i$
Subspace Angle (°)	$1.176 + 4.1564 \times 10^{-13}i$	$1.166 - 1.7555 \times 10^{-13}i$
Correlation	$0.9998 - 1.4883 \times 10^{-16}i$	$0.9998 + 6.2367 \times 10^{-17}i$

Table 3.4. Recovery performance figures for OFDM, set 3.

	Signal 1	Signal 2
Power Angle (°)	42.56	47.23
Error Figure	$0.0005003 + 2.2331 \times 10^{-28}i$	$0.0004999 + 1.6457 \times 10^{-28}i$
Subspace Angle (°)	$1.282 - 1.9555 \times 10^{-12}i$	$1.281 + 3.2425 \times 10^{-14}i$
Correlation	$0.9997 + 7.6339 \times 10^{-16}i$	$0.9998 - 1.2653 \times 10^{-17}i$

Table 3.5. Recovery performance figures for OFDM, set 4.

	Signal 1	Signal 2
Power Angle (°)	45.54	42.5
Error Figure	$0.0001 - 2.2446 \times 10^{-30}i$	$0.0001001 - 1.7213 \times 10^{-29}i$
Subspace Angle (°)	$0.573 + 1.1413 \times 10^{-13}i$	$0.5732 - 1.3908 \times 10^{-12}i$
Correlation	$0.9999 - 1.9919 \times 10^{-17}i$	$0.9999 + 2.4284 \times 10^{-16}i$

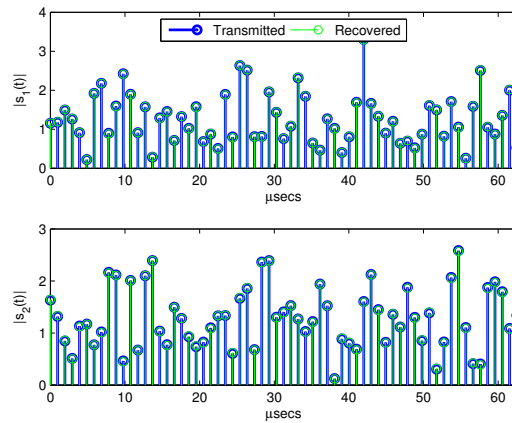
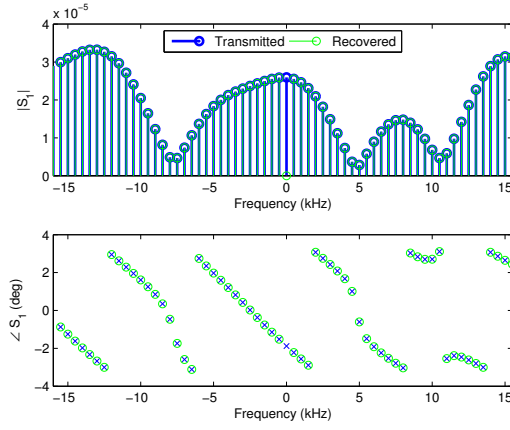
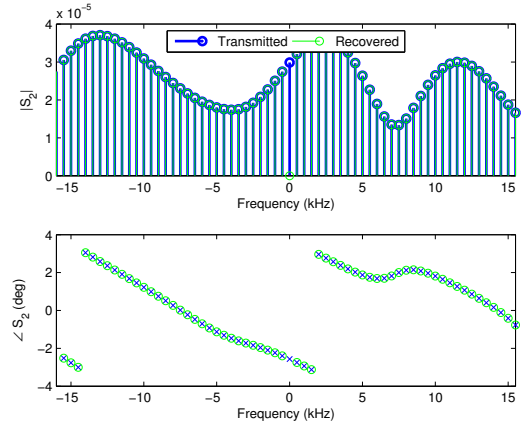


Figure 3.1. OFDM test signal, time domain.

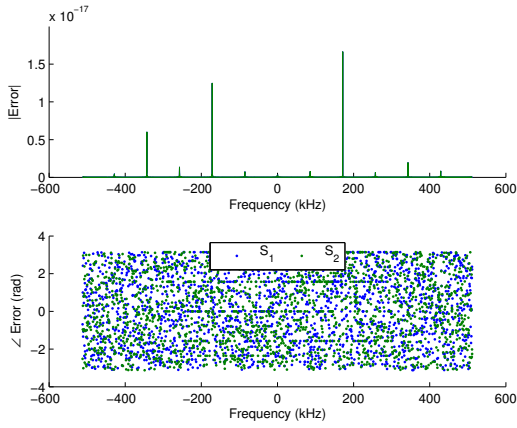


(a) First signal

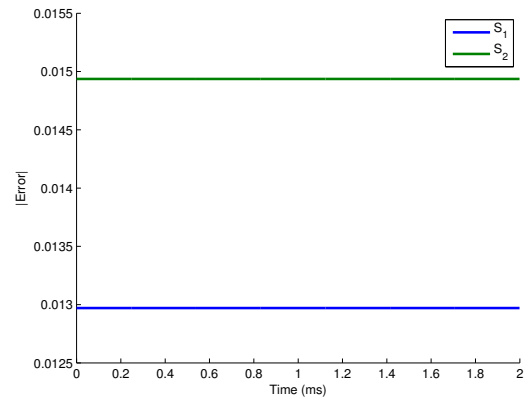


(b) Second signal

Figure 3.2. Frequency domain of OFDM test transmitted and recovered signals.



(a) Frequency domain



(b) Time domain

Figure 3.3. Error of recovered OFDM signals.

THIS PAGE INTENTIONALLY LEFT BLANK

---

## CHAPTER 4:

### Collection Geometry Analysis

---

The recovery method in Section 2.1 depends upon an invertible  $\mathbf{\Delta}$  matrix in  $\mathbf{\Delta}\mathbf{S} = \mathbf{R}$ , as identified in Section 2.2. In addition to an equal number of transmitters and receivers ( $m = n$ ) such that  $\mathbf{\Delta}$  is square, the collection geometry plays a significant role in the invertibility of this matrix, as each element of the  $\mathbf{\Delta}(i)$  block is of the form  $e^{-j2\pi\frac{i-1}{N}f_s\tau_{mn}}$  and depends upon the propagation delay  $\tau_{mn}$ . A means to assess a given collection geometry and an initial analysis of the impact of several such geometries upon the recovery performance is provided in this section.

#### 4.1 Geometry Assessment

In linear algebra, the sensitivity of  $\mathbf{x}$  to small perturbations in  $\mathbf{b}$  when solving the  $\mathbf{A}\mathbf{x} = \mathbf{b}$  problem is described by the *condition number* of the  $m \times m$   $\mathbf{A}$  matrix,

$$\kappa(\mathbf{A}) = \frac{\sigma_1}{\sigma_m} \quad (4.1)$$

where  $\sigma_1$  is the largest singular value and  $\sigma_m$  is the smallest [23]. (Both are computed via the singular value decomposition of  $\mathbf{A}$ .) A matrix with a small condition number is described as *well-conditioned*, while a matrix with a large condition number is described as *ill-conditioned*. A singular matrix is often indicated by  $\kappa(\mathbf{A}) = \infty$  [24]. Condition numbers that yield acceptable or unacceptable results are very dependent upon the details of the specific problem. See [23] or [24] for a more complete discussion of the condition number and singular value decomposition.

In the case of (2.7), the  $\mathbf{\Delta}$  matrix is a block diagonal matrix consisting of the  $\mathbf{\Delta}(i)$  blocks associated with each frequency  $\omega$ , as defined in (2.6). As each of these blocks is independent of the other blocks in the  $\mathbf{\Delta}$  matrix, it is possible to assess the condition numbers of the blocks independently, for the given frequency associated with that block, rather than simply evaluating the condition of the complete  $\mathbf{\Delta}$  matrix. This assessment provides insight as to the recovery performance at each frequency used in the recovery calculation and is provided in conjunction with the frequency-domain recovery error plot for each of the

layouts presented in the following section.

## 4.2 Layout Overview and Test Signal

Four transmitter and receiver geometries are evaluated, in addition to the layout used in the preceding sections, which is included as a reference layout (Layout 1). The transmitter locations remain constant throughout the analysis. Layout 2 extends the separation between the receivers to 500 km from the previous 50 km. Layout 3 uses this same extended receiver baseline and increases the altitude of the second receiver from 400 km to 800 km. Layout 4 moves the second receiver such that it appears at roughly five degrees above the transmitters' horizon. Those receivers have an altitude of 200 km. Lastly, Layout 5 evaluates the possibility of co-locating receivers on a single platform using a 1-meter receiver separation. These layout parameters are provided in Table 4.1, with parameters that vary from the reference layout indicated in bold font. An illustration (not to scale) of the five layouts is provided in Figure 4.1, which includes a red outline of the reference layout.

To facilitate comparison across test layouts, a single set of OFDM signal parameters was utilized for all tests. Those signal parameters (Set 1 from Section 3.2) are provided in Table 4.2. Additionally, in order to minimize any variation in the recovery performance and facilitate comparison across the various geometries, the content of each transmitter's signal was maintained as a constant across each of the layouts.

## 4.3 Results

Correlation coefficient values for each recovered signal are provided for the various layouts in Table 4.3. The complete set of metrics discussed in Section 2.3.3 are provided in Appendix B.2. Each case has a correlation coefficient at or very near one, and with one exception, all have imaginary parts on the order of  $\epsilon_{\text{machine}}$ . The only exception is with Layout 5, with the two receivers on the same collection platform, and in that case the imaginary part is between two and three orders of magnitude larger than  $\epsilon_{\text{machine}}$  but remains on the order of  $10^{-13}$ .

Frequency-domain recovery error (as described in Section 2.5.2) and condition number plots are provided for each layout in Figure 4.2 through Figure 4.6. The condition number plots provide both an overview of the full spectrum used for recovery, as well as a view of

Table 4.1. Transmitter and receiver geometries, by layout. (In kilometers.)

	Element	$x$	$y$	$alt$
Layout 1 (Reference)	Tx 1	0	0	0
	Tx 2	0	30	0
	Rx 1	146.2	0	400
	Rx 2	146.2	50	400
Layout 2	Tx 1	0	0	0
	Tx 2	0	30	0
	Rx 1	146.2	0	400
	Rx 2	146.2	<b>500</b>	400
Layout 3	Tx 1	0	0	0
	Tx 2	0	30	0
	Rx 1	146.2	0	400
	Rx 2	146.2	<b>500</b>	<b>800</b>
Layout 4	Tx 1	0	0	0
	Tx 2	0	30	0
	Rx 1	146.2	0	400
	Rx 2	<b>1113</b>	50	<b>200</b>
Layout 5	Tx 1	0	0	0
	Tx 2	0	30	0
	Rx 1	146.2	<b>50.001</b>	400
	Rx 2	146.2	50	400

Table 4.2. Geometry analysis test signal parameter summary.

	Value
Subcarriers	6
Modulation Scheme	QPSK
Bandwidth (kHz)	600
Symbols	16

a subset of the lower frequencies, depicted on a logarithmic y-axis. (The area contained in the subset view is indicated in the plot of the full spectrum with a red box.) This provides a better understanding of the periodic nature of the condition number that occurs with some geometries. As the condition number of the  $\Delta(0)$  block is known to be infinite, it has been omitted from the plots. In each layout, there is a clear correlation between the condition number at a given frequency and the frequency-domain recovery error depicted in the corresponding figure. It is also worth noting that the largest condition number (which occurs in the Layout 5 case) is also correlated with the largest recovery error. Even in that



case, with a condition number on the order of  $10^7$ , the frequency-domain recovery error only approaches  $6 \times 10^{-14}$ , and the correlation coefficients for that layout remain close to one, indicating excellent recovery performance.

The complete set of signal and error plots for each of the layouts is provided in Appendix B.2. Note that Layouts 2, 3, and 4 involve larger propagation delays than Layouts 1 and 5 and require additional zero padding in the time domain. That additional zero padding results in samples at a closer interval in the frequency domain, which is apparent in the associated figures.

Table 4.3. Correlation coefficient summary by layout number.

	Signal 1	Signal 2
Layout 1	$0.9987 - 2.6904 \times 10^{-17}i$	$0.9991 - 2.496 \times 10^{-16}i$
Layout 2	$0.9994 + 1.9458 \times 10^{-16}i$	$0.9995 - 7.809 \times 10^{-16}i$
Layout 3	$0.9994 - 6.9239 \times 10^{-17}i$	$0.9995 - 5.1021 \times 10^{-16}i$
Layout 4	$0.9994 - 2.9356 \times 10^{-17}i$	$0.9995 + 1.2612 \times 10^{-16}i$
Layout 5	$0.9987 - 2.2326 \times 10^{-12}i$	$0.9991 + 6.5599 \times 10^{-13}i$

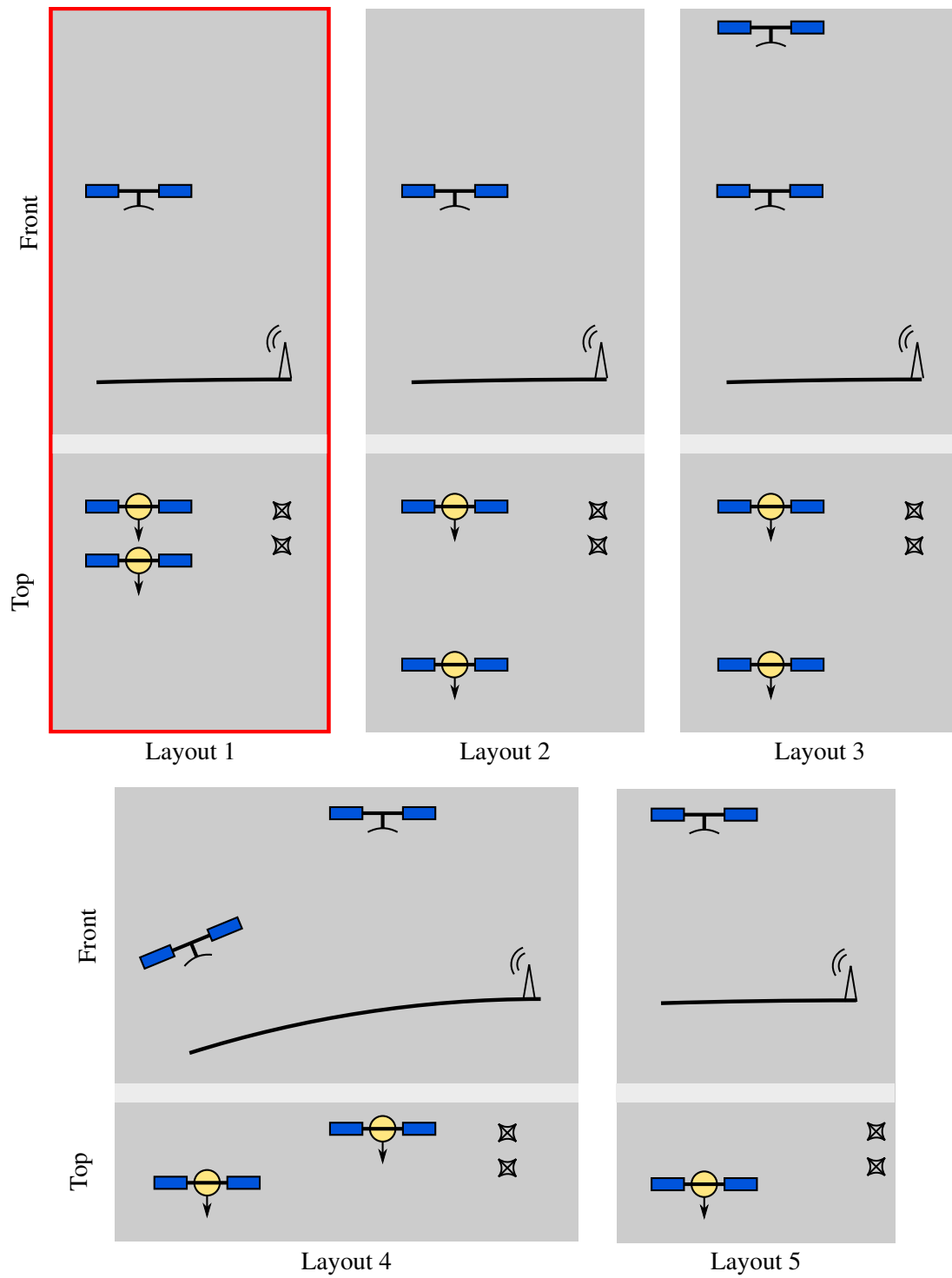
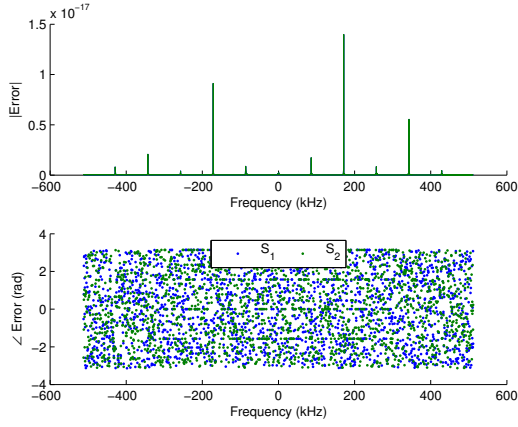
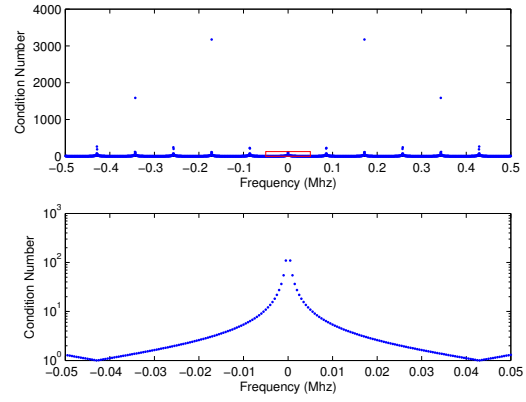


Figure 4.1. Overview of geometry test laydowns.

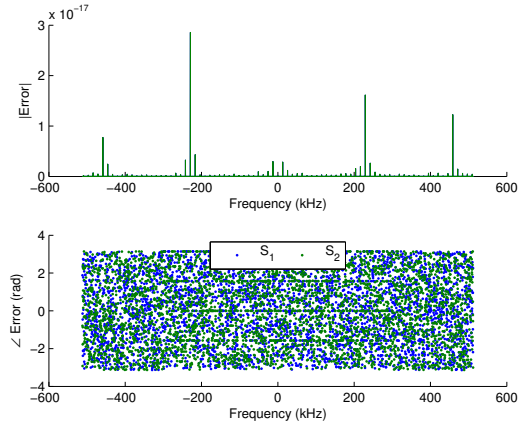


(a) Frequency-domain error

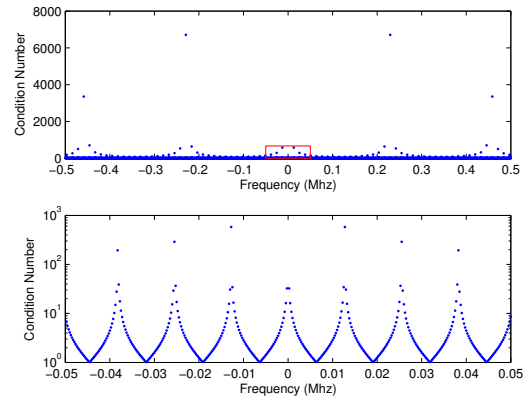


(b) Condition number

Figure 4.2. Geometry induced recovery errors, layout 1.

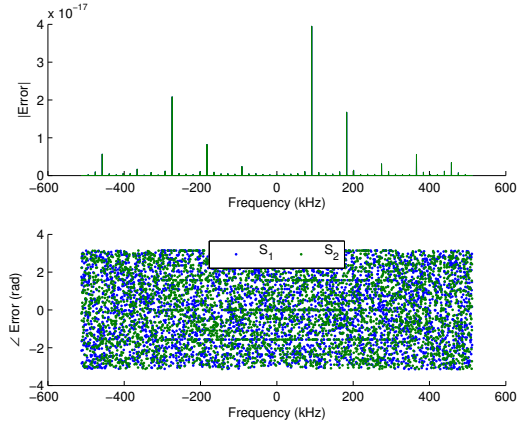


(a) Frequency-domain error

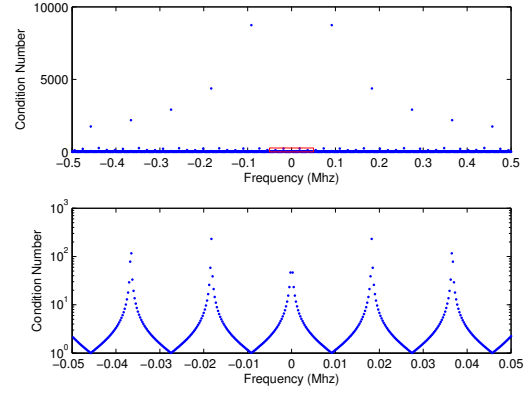


(b) Condition number

Figure 4.3. Geometry induced recovery errors, layout 2.

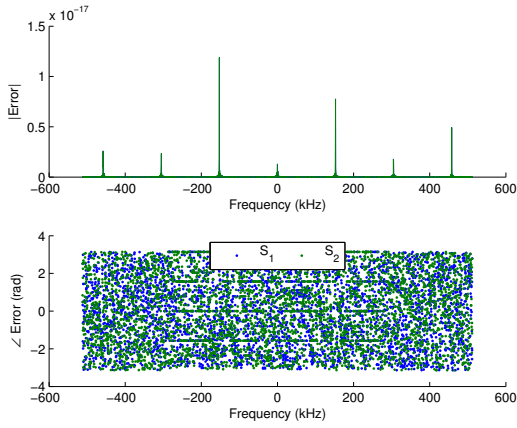


(a) Frequency-domain error

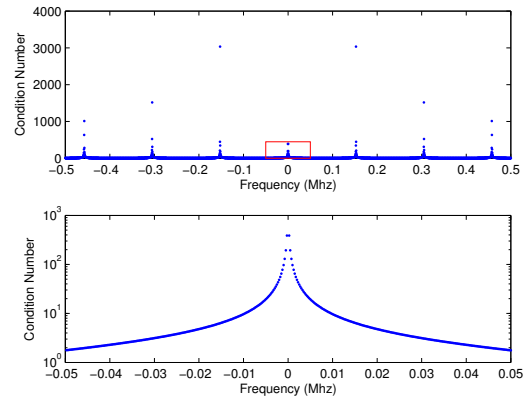


(b) Condition number

Figure 4.4. Geometry induced recovery errors, layout 3.

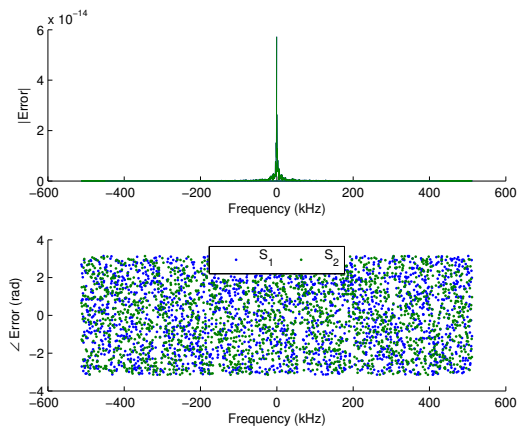


(a) Frequency-domain error

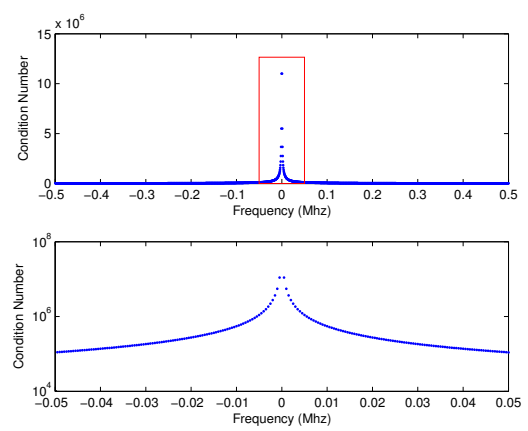


(b) Condition number

Figure 4.5. Geometry induced recovery errors, layout 4.



(a) Frequency-domain error



(b) Condition number

Figure 4.6. Geometry induced recovery errors, layout 5.

---

## CHAPTER 5:

### Conclusion

---

An approach to signal recovery based upon the known propagation delays between a set of known transmitters and receivers was described in this thesis. While results with narrowband signals do not offer much initial promise for the approach, by considering the frequency response associated with delayed signals and the need for the delay in continuous time to resemble the circular shift associated with discrete time signals, admirable performance was demonstrated with the wideband signals typical of fourth generation cellular transmissions.

### 5.1 Summary of Results and Identified Limitations

Examination of recovery results with several OFDM signals as well as in a variety of geometries indicates that the proposed method is worth further consideration and study. The recovery approach produced correlation coefficients approaching one for the various OFDM signal parameters evaluated as well as the variety of collection geometries. The use of the condition number to evaluate prospective collection geometries offers insight into potential errors in the frequency domain of the recovered signals and the viability of a potential collection from a geometry perspective.

A number of limitations exist that must be addressed before the approach is viable for real-world signal recovery. Performance in the presence of noise is a considerable limitation. The above results indicate the need for an additional 35 dB of SNR, a considerable margin under any realistic circumstances. The known singularity at  $f = 0$  Hz may also be a limitation if applied to a signal that has a non-zero DC subcarrier. Computational complexity must also be considered, given the potential size of the  $\mathbf{\Delta}$  matrix. These limitations and potential solutions are further described in the following section.

### 5.2 Future Work

There are a number of areas that merit additional study, either to address identified shortcomings of the approach as it currently exists or to extend the work in order to ensure

adequate performance in the intended application.

### 5.2.1 Received Signal Model Improvement

As discussed in Section 2.5.1, the model currently constructs wideband signals as the sum of delayed copies of time-limited transmissions. For small differences in delay times, this results in a small fraction of each received signal that only contains signal from a single transmitter, as, due to differences in the propagation delays between the transmitter and receiver pairs, the signals from the other transmitters have either not yet arrived or have completely arrived. For longer propagation delays coupled with shorter signals, this can potentially result in the signals arriving at the receiver at distinctly different times.

While the recovery process does not take advantage of this difference in arrival times, it is more likely that a base-station transmitter would exhibit a much larger transmit duty cycle and a more accurate model would ensure that each sample of the received signal contained a contribution from each of the transmitters. This would require the generation of longer duration signals and the application of a windowing or indicator function such as (2.26), where the indicator domain  $A$  is limited to a period of time when all signals are present in the receiver.

### 5.2.2 Computational Complexity

In (2.7), the  $\Delta$  matrix is  $mN \times nN$ , where  $m$  and  $n$  are the numbers of receivers and transmitters, respectively. The parameter  $N$  is the number of discrete frequencies, which is a function of the desired signal duration, sampling rate and amount of zero padding required for the given signal delay. Increasing the sample rate in order to accommodate higher bandwidth signals or the extending the buffer length when zero padding signals with larger propagation delays has the potential to dramatically increase the size of the  $\Delta$  matrix and the computation time associated with signal recovery as a result. Of note, in this work, this limitation required a lower altitude for the off-nadir receiver in Layout 4 of the geometry test. It may be possible to use the difference in propagation time across the various transmitter/receiver pairs vice the absolute time, which, in some geometries would offer a considerable savings in the amount of zero padding required.

Some improvement may also be available as a result of the fact that the  $\Delta$  matrix is particularly sparse. Use of MATLAB's sparse matrix tools should both decrease memory

requirements and decrease computation time given that the number of non-zero entries in the  $\mathbf{\Delta}$  matrix grows as  $O(N)$  while size grows as  $O(N^2)$ . Similarly, as currently defined, it is possible to break the  $\mathbf{\Delta S} = \mathbf{R}$  equation into a set of  $\mathbf{\Delta}(i)\mathbf{S}(i) = \mathbf{R}(i)$  equations for each discrete frequency  $i$  and solve those independently. This would complicate approaches that leverage any potential correlation between adjacent frequencies to improve performance with noise or in the  $m < n$  case. (See below.)

### 5.2.3 Accuracy of Delay Knowledge

The preceding work is entirely dependent upon and assumes completely accurate knowledge of the delays associated with signal propagation between each transmitter and receiver pair and uses double precision variables for the associated computations. There is no error included in any transmitter or receiver position data, either when constructing the received signals or when solving for the signals as originally transmitted.

Such levels of accuracy are not available when using real-world transmitters and receivers, and it is necessary to evaluate performance under varying accuracy conditions. That analysis should likely include both an analytical evaluation of the pertinent recovery equations to quantify the impact of a small change in the expected signal delay on the recovered signals as well as a Monte Carlo simulation with varying error levels to confirm that analysis.

The matter is complicated by the interactions between the different delays in the  $\mathbf{\Delta}$  matrix. If each transmitter and receiver has an associated position error, the geometric arrangement of those antennas will have a different effect on the delay between each transmitter and receiver. Those various errors are then combined in the  $\mathbf{\Delta}$  matrix and impact the recovered signal. It would be useful to understand the impact of a positional error associated with a single transmitter or receiver as well as a set of comparable errors across the complete set of transmitters and receivers.

### 5.2.4 Noise

As identified in Section 2.6, noise poses a considerable problem for the recovery process as it solves the  $\mathbf{\Delta S} = \check{\mathbf{R}}$  equation while  $\mathbf{\Delta S} + \eta = \check{\mathbf{R}}$  is a more accurate model of the received signals. One potential approach to mitigating the impact of the noise on signal recovery relies upon the fact that the signals of interest are transmitting digital data in accordance with published standards, such as [7].



Those standards include a specific symbol library, and forcing the recovery signal to adhere to the library may mitigate some of the impacts of noise. After an initial attempt at signal recovery, the recovered signals might be processed as they would by a typical commercial receiver, including the detection process, yielding channel symbols [25]. By re-encoding those recovered channel symbols, the resulting signal is effectively a clean version of the recovered signal (precisely what was transmitted, in the ideal case), and any noise-induced differences between the recovered symbol and the re-encoded symbol are eliminated. While this does not protect against any difference that effectively results in an incorrect channel symbol, it may offer some performance improvement over the existing recovery process. While it likely involves a considerable increase in complexity, it may be possible to extend this decoding/re-encoding process to leverage any error correction coding present in the signal-of-interest, further mitigating the impact of noise on the recovered signal.

It is also important to recognize that the condition number serves as an indicator of the sensitivity of the recovered signal to small perturbations in the received signals. When the condition number is larger, the noise in the received signals will have a greater impact on the recovered signal than in those cases with smaller condition numbers. With further study, it may be possible to develop an empirical understanding of the cases when a larger condition number requires some alternative recovery approach or noise mitigation strategy prior to or as part of the recovery process.

### **5.2.5 Evaluation of Recovered Signals as Bistatic Illuminators**

Ultimately, the signal recovery process is intended to support bistatic SAR imaging, with a recovered signal serving as the illuminator for the imaging process. It is important to understand the implications to the imaging process when a recovered signal is utilized vice the more typical case employing a known pulse shape. Holder [18] developed a model of a monostatic SAR system which could be extended to accommodate bistatic signals and then used to evaluate the impact of the recovery process.

There are two fundamental changes to the existing model necessary to support that evaluation. First, the model needs to be extended to accommodate bistatic imaging, including the incorporation of bistatic delay calculations for the layout of targets. In the monostatic case,

the round-trip fast-time delay is [2]

$$t = \frac{2\sqrt{x^2 + (y-u)^2}}{c}, \quad (5.1)$$

where  $x$  and  $y$  describe the target position,  $u$  is the radar's position along the  $y$ -axis, and  $c$  is the speed of light. In the bistatic case, this delay calculation must account for the location of the transmitter and is no longer a round trip time. In that case, the delay is given by

$$t = \frac{1}{c} \left[ \sqrt{(x-p)^2 + (y-q)^2} + \sqrt{x^2 + (y-u)^2} \right], \quad (5.2)$$

where  $p$  and  $q$  describe the location of the transmitter. These delay calculations are then used to construct the signals received during the collection process.

The SAR model described by Holder uses Spatial Frequency Interpolation for the image reconstruction process, which converts the received signals to a recognizable image. This algorithm requires two-dimensional, frequency-domain matched filtering [2]

$$S(\omega, k_u) S_0^*(\omega, k_u), \quad (5.3)$$

where  $S(\omega, k_u)$  is the frequency-domain representation of the received SAR signal and  $S_0^*(\omega, k_u)$  is the two-dimensional matched filter frequency response. While Soumekh [2] describes the derivation of  $S_0^*(\omega, k_u)$  for the monostatic case, it will be necessary to adapt that to the bistatic case in order to create the SAR images required to properly evaluate signal recovery performance. The recovered signal is used directly in that matched filtering process and is referred to as the reference signal in both [2] and [18].

The ability to study the impact of using recovered signals for SAR image formation then allows further examination of the impact of noise and positional errors on the overall system. While both of those can be worked somewhat independently, that work ultimately impacts the quality of the SAR image, and understanding the impacts of both noise and positional error on the image quality is critical to the utility of the approach.

### 5.2.6 Adaptation to $m < n$ Scenarios

Given the proliferation of LTE and WiMax transmitters, coupled with the fiscal constraints and limited resource availability, a signal recovery approach that functions when there are more transmitters than receivers is particularly desirable. This is a classical example of an *underdetermined* problem, as given the resulting shape of the  $\Delta$  matrix, there is not enough information available to yield a single solution to the  $\Delta \mathbf{S} = \mathbf{R}$  matrix equation. Common approaches to this underdetermined problem such as seeking the solution that contains the most zero elements or that minimizes an error function (often referred to as the method of Least Squares) do not seem well suited to this particular problem, as there is no expectation that the original waveforms adhered to either of those paradigms.

By oversampling the received signals, it is possible to develop some redundant information in those signals. In the frequency domain, this means that the adjacent samples are no longer independent. By incorporating that assumption into the construction of the  $\Delta$  matrix, such that the solution for a given point in the frequency-domain representation of the signal is dependent upon other surrounding values, it may be possible to develop a better approximation for the original signal.

---

## APPENDIX A:

### Signal Interpolation

---

In order to evaluate the signal isolation approach described in Section 2.1, it is necessary to generate a collection of signals that contains a set of original signals at various delays. This is straightforward in the narrowband case which uses signals defined over a time limited period  $t$  of the form

$$s_n(t) = A_n \cos(\omega_n t) \quad (\text{A.1})$$

as the cosine is a continuous function and the required delays can be computed as  $s_n(t - \tau_{mn})$ . In the wideband case, which simply uses time-limited AWGN as the signal-of-interest, one approach to computing the various delays is to interpolate the original signal at the necessary delayed sample times. This interpolation is commonly performed using Ideal Low Pass Filter Interpolation. As an alternative, an approach utilizing a phase shift in the frequency domain was evaluated. Both are described below with a comparison of results of the two approaches.

### A.1 Ideal Low Pass Filter Interpolation

Interpolation allows recovery of information from the original continuous time signal that is not immediately available after the sampling process. This approach to interpolation utilizes a low pass filter to counter the effects of the sampling process. The sampling process and its effects in the time and frequency domain are reviewed below prior to an explanation of interpolation using an ideal low pass filter.

#### A.1.1 Sampling in the Time Domain

Ideal sampling of a continuous time signal  $s(t)$  can be considered as the product of that signal with a train of unit impulses

$$p(t) = \sum_{k=-\infty}^{+\infty} \delta(t - nT), \quad (\text{A.2})$$

yielding the sampled signal

$$\begin{aligned}
 x_s(t) &= x(t)p(t) \\
 &= \sum_{n=-\infty}^{+\infty} x(t)\delta(t-nT) \\
 &= \sum_{n=-\infty}^{+\infty} x(nT)\delta(t-nT)
 \end{aligned} \tag{A.3}$$

as a train of pulses with area determined by the signal at each sample interval. For convenience, the notation  $x[n]$  is used to represent a discrete time equivalent of  $x(nT)$ . This process is illustrated in Figure A.1a. Once sampled, the continuous time information is no longer directly available — interpolation is required to recover signal information at other than the sampled instants.

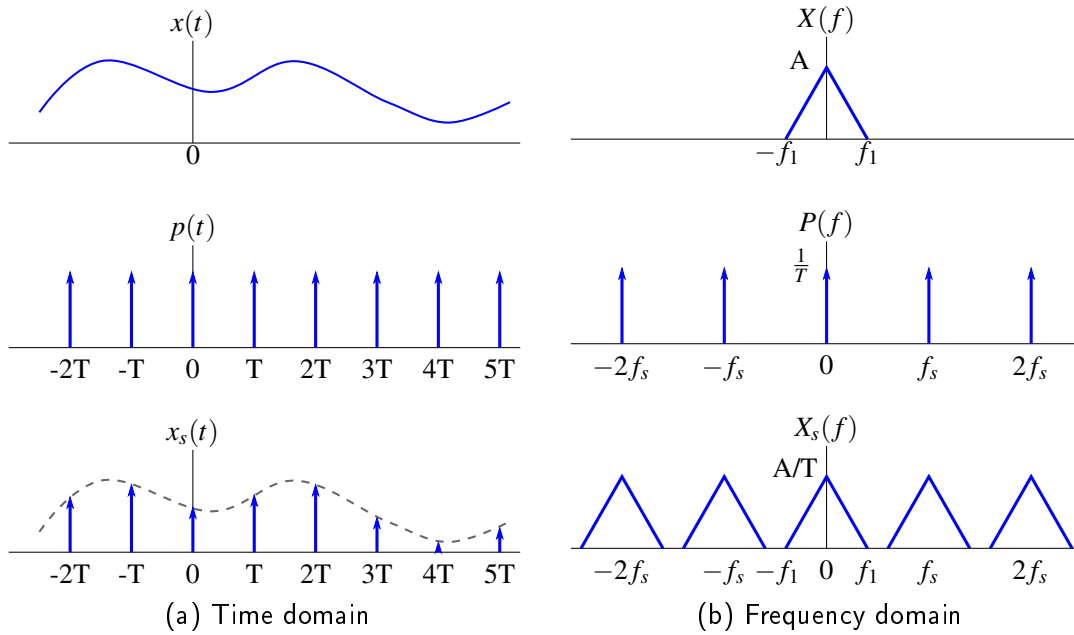


Figure A.1. Sampling a continuous time signal, after [19].

### A.1.2 Frequency-domain Perspective

In the frequency domain, depicted in Figure A.1b, the impulse train used for sampling is also an impulse train, and taking  $f_s = 1/T$ , is described by

$$P(f) = f_s \sum_{k=-\infty}^{+\infty} \delta(f - kf_s). \quad (\text{A.4})$$

The multiplication of  $s(t)$  and  $p(t)$  in the time domain corresponds to convolution in the frequency domain, such that

$$\begin{aligned} X_s(f) &= X(f) * P(f) \\ &= f_s \sum_{k=-\infty}^{+\infty} X(f) * \delta(f - kf_s) \\ &= f_s \sum_{k=-\infty}^{+\infty} X(f - kf_s), \end{aligned} \quad (\text{A.5})$$

which is a train of the original spectrum repeated at multiples of  $f_s$  in the frequency domain [19], [21]. As long as the sampling rate exceeds that required by the Nyquist sampling theorem, aliasing is avoided.

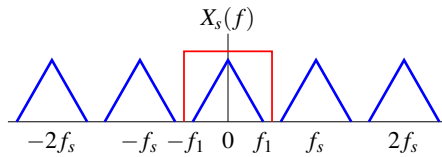


Figure A.2. Ideal low pass filter.

### A.1.3 Interpolation in the Frequency Domain

In the absence of aliasing, in order to recreate the original continuous time signal, the original frequency spectrum can be obtained by applying an ideal low pass filter to isolate the spectrum of the original signal, as depicted in Figure A.2 [12]. The ideal low pass filter is described by

$$H_{\text{ILPF}}(f) = K \prod \left( \frac{f}{2B} \right) \quad (\text{A.6})$$

where

$$\Pi(x) = \begin{cases} 1 & \text{if } |x| < 1/2 \\ 0 & \text{otherwise} \end{cases} \quad (\text{A.7})$$

is known as the rectangle function. Applying the ideal low pass filter to (A.5) gives

$$Y(f) = H_{\text{ILPF}}(f)X_s(f) = Kf_sX(f), \quad (\text{A.8})$$

and selecting  $K = 1/f_s$  gives  $Y(f) = X(f)$ . The inverse Fourier transform can then be used to recover the original time-domain signal.

#### A.1.4 Interpolation in the Time Domain

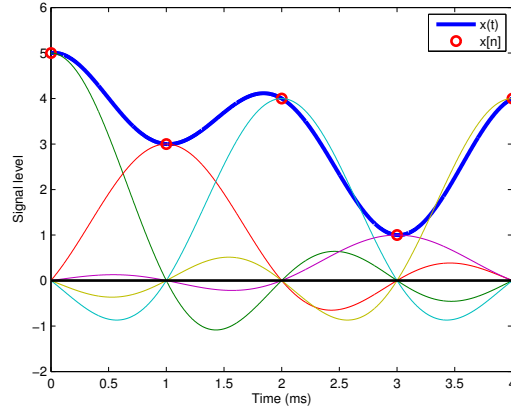


Figure A.3. Signal interpolation as a sum of scaled and shifted sinc() pulses.

The multiplication of  $X_s(f)$  by the ideal low pass filter's frequency response in (A.8) is convolution in the time domain, such that  $y(t) = h_{\text{ILFP}}(t) * x_s(t)$ . Substituting (A.3) then gives

$$\begin{aligned} y(t) &= h_{\text{ILFP}}(t) * \sum_n x[n] \delta(t - nT) \\ &= \sum_n x[n] h_{\text{ILFP}}(t) * \delta(t - nT) \\ &= \sum_n x[n] h_{\text{ILFP}}(t - nT). \end{aligned} \quad (\text{A.9})$$

Given the Fourier transform relationship

$$K \Pi\left(\frac{f}{2B}\right) \stackrel{\mathcal{F}}{\Leftrightarrow} 2BK \operatorname{sinc}(2Bt), \quad (\text{A.10})$$

and choosing  $B = f_s/2$  and  $K = 1/f_s$ , (A.9) becomes

$$y(t) = \sum_n x[n] \operatorname{sinc}(f_s t - n) \quad (\text{A.11})$$

which is a sum of shifted  $\operatorname{sinc}()$  pulses, each scaled by a corresponding coefficient from the  $x[n]$  vector [12]. This is illustrated in Figure A.3, which depicts the constituent  $\operatorname{sinc}()$  functions that are added to construct the  $x(t)$  signal. Each  $\operatorname{sinc}()$  pulse is zero at all multiples of  $T$  other than the peak, and each sample point only receives a contribution from a the single  $\operatorname{sinc}()$  that corresponds to that particular  $x[n]$  value. (Note that all but one of the  $\operatorname{sinc}()$  curves are zero below each of the red circles corresponding to a sample in  $x[n]$ .) All other points in the  $x(t)$  signal are composed of contributions from each of the  $\operatorname{sinc}()$  pulses. MATLAB code to perform this interpolation function is provided in Appendix C.6 as the function `interp_time.m`. As MATLAB works with sampled signals, this code returns the signal resampled at new time values, which are specified as an argument to the function.

### A.1.5 Error Analysis

As a baseline for later sections, it is useful to understand the amount of error induced by this interpolation process. As a challenging case, a signal  $x(t)$  consisting of AWGN was sampled to create  $x[n]$ . A sampled version of  $x(t - \tau)$  was generated by interpolating  $s[n]$  at a delayed point in time, where  $\tau$  is an integer multiple of the sampling interval and a significant fraction of the overall signal duration to make the delay apparent in the following figures. For comparison, a circular shift corresponding to  $\tau$  was applied to the same sampled AWGN signal. Those signals are presented in Figure A.4, along with the difference between those two signals (plotted on a separate y-axis to emphasize the dramatic difference in scale.) The total energy in both shifted signals was computed as

$$E_i = \mathbf{x}_i^* \mathbf{x}_i T_{\text{samp}}, \quad (\text{A.12})$$



where  $\mathbf{x}_i$  is a column vector of the signal-of-interest with sampling interval  $T_{\text{samp}}$ , and  $\mathbf{x}_i^*$  is the conjugate transpose of the column, such that  $\mathbf{x}_i^* \mathbf{x}_i$  computes the inner product of the signal. This was compared to the energy in the original  $x[n]$ . The differences in energy are presented in Table A.1 and show error on the order of  $\epsilon_{\text{machine}}$ , which indicates that shifting via interpolation is a viable option.

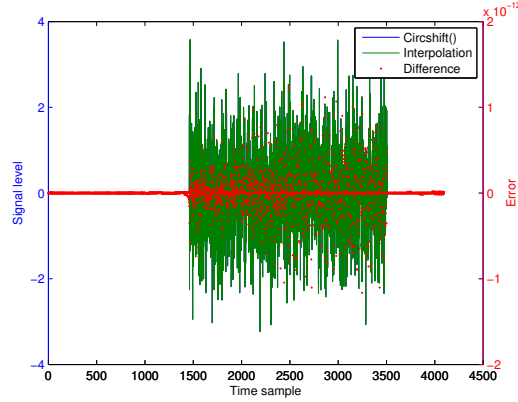


Figure A.4. Signals and error from shifting via interpolation.

Table A.1. Energy summary for shifting via interpolation.

	Energy Error (J)
Circular Shift	$4.3368 \times 10^{-19}$
Interpolation	$2.4286 \times 10^{-17}$

## A.2 Fourier Phase Shifting for Interpolation

In the continuous time domain, the Fourier transform has a property that relates a shift in the time domain to a phase shift in the frequency domain [19], such that

$$x(t) \xrightarrow{\mathcal{F}} X(\omega) \quad (\text{A.13})$$

$$x(t - t_d) \xrightarrow{\mathcal{F}} X(\omega) e^{-j\omega t_d}. \quad (\text{A.14})$$

In the discrete time domain, the discrete Fourier transform has a similar property such that a circular shift in the discrete time domain results in a phase shift in the frequency

domain [21]. That is,

$$x[n] \xLeftrightarrow{\text{DFT}} X[k] \quad (\text{A.15})$$

$$x[n \oplus m] \xLeftrightarrow{\text{DFT}} X[k] e^{j(2\pi/N)(km)} \quad (\text{A.16})$$

where  $n$  is the index or sample number,  $\oplus$  represents the left circular shift operation,  $m$  is the integer number of samples to shift by,  $N$  is the total number of samples, and  $k$  is the discrete frequency index. With adequate zero padding, this circular shift resembles the time delay from the continuous time domain, where the delay is given by  $t_d = mT_{\text{samp}}$  and  $T_{\text{samp}}$  is the sampling interval. This allows for shifting of signals by integer multiples of the sampling interval by applying the FFT, multiplying by the appropriate phase shift in the frequency domain, and returning to the time domain with the IFFT. While this convenient for signals that are already in the frequency domain, it is likely excessive effort for a signal in the time domain, as a circular shift operation is accomplished with a straightforward manipulation of the index numbers.

For comparison to other cases, plots of the delayed signals and associated error between this method and the circular shift in the time domain are provided in Figure A.5. As this method involves multiplication by complex terms, plots of both the real and imaginary parts of the signal are provided. Similarly, the energy difference between the phase shifted and circularly shifted signals are provided in Table A.2, which also includes entries for both the real and imaginary portions of the error. Each is well below  $\epsilon_{\text{machine}}$ .

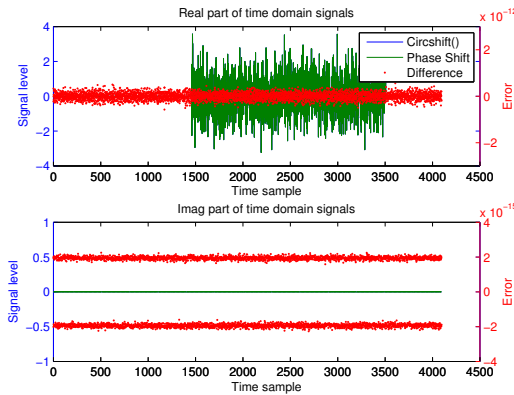


Figure A.5. Signals and error from integer phase shifts in the frequency domain.

Table A.2. Energy summary for integer phase shifts in the frequency domain.

	Energy (J)
Error	$8.9355 \times 10^{-29}$
Real(Error)	$8.934 \times 10^{-29}$
Imag(Error)	$1.51 \times 10^{-32}$

### A.2.1 Fractional Delays

The opportunity to use non-integer or fractional delays for shifting is appealing as it accomplishes an interpolation to get the new set of values of  $x(t)$  that are required but not available directly in  $x[n]$ . The plots of the signals and error that result from such an attempt are provided in Figure A.6. As the circular shift does not accommodate fractional shift amounts, an interpolation was used as the baseline signal for comparison and when computing both the error plot and energy errors, which are presented in Table A.3. The error levels in this case are much more significant than those with integer shift amounts, and, more significantly, the error in the imaginary portion of the signal is an order of magnitude larger than that of the real portion. Intuitively, as the process begins with a real signal and the intent is to merely delay the signal in time, the result should not have an imaginary portion.

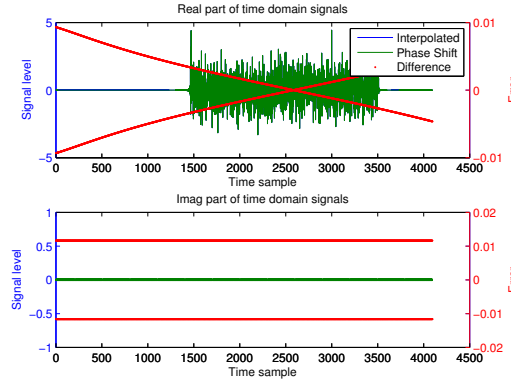


Figure A.6. Signals and error from fractional phase shifts in the frequency domain.

Table A.3. Energy summary for fractional phase shifts in the frequency domain.

	Energy (J)
Error	$6.1483 \times 10^{-7}$
Real(Error)	$7.2528 \times 10^{-8}$
Imag(Error)	$5.423 \times 10^{-7}$

## Error Source

The Fourier transform, in both the continuous and discrete forms, has a number of properties that are helpful when considering this error. In particular, when  $x(t)$  is real, the frequency-domain description of the same signal  $X(f)$  will be conjugate symmetric, such that  $X(-f) = X^*(f)$  [19]. The inverse is also true, such that a signal must be conjugate symmetric in the frequency domain in order to be real in the time domain.

Recall that in the case of discrete signals, the frequency domain is periodic. In that case, conjugate symmetry requires that  $X[n] = X^*[N - n]$  where the signal is periodic over  $N$  points,  $n < N$ , and the first point is  $n = 0$ . (In MATLAB, indices begin at  $n = 1$ , so in that case conjugate symmetry requires  $X[n] = X^*[N + 2 - n]$ . The remainder of this discussion will assume the first index is  $n = 0$ .) Two of these points are significant —  $n = 0$  and  $n = N/2$ . When  $n = 0$ , the above relationship requires conjugate symmetry with the point at  $n = N$ , which exceeds the length of the sampled signal but corresponds to itself when the periodic nature of the DFT frequency domain is considered. The same is true for  $n = N/2$ , which must also be conjugate symmetric with itself, or, more simply, real.

When shifting a signal by a fraction of the sampling interval, the  $e^{-j\omega\tau}$  term must be conjugate symmetric in order for the resulting signal to be real-valued in the time domain. That requires that both the  $n = 0$  and  $n = N/2$  values in that term to be real valued, which is not the case when shifting by fractions of a sampling interval. In that case the  $n = N/2$  value will be complex, and the resulting signal will have an imaginary part in the time domain.

## Forcing Conjugate Symmetry

As a real valued result is expected, the  $n = N/2$  point can be artificially forced to a real value by eliminating the imaginary portion of that sample prior to applying the  $e^{-j\omega\tau}$  term. In that case, the phase shift term is conjugate symmetric, and the resulting signal should be shifted in the time domain without incurring an imaginary portion. Results of that process are provided in Figure A.7, which again depicts errors relative to a signal delayed via interpolation. The error in the signal energy is presented in Table A.4, which shows the energy in the imaginary portion has been reduced to zero as expected.

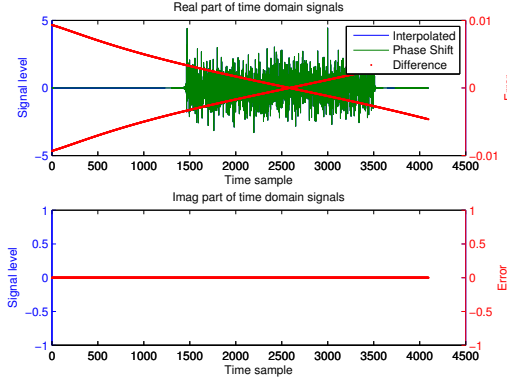


Figure A.7. Signals and error from fractional phase shifts with forced symmetry.

Table A.4. Energy summary for fractional phase shifts with forced symmetry.

	Energy (J)
Error	$7.2528 \times 10^{-8}$
Real(Error)	$7.2528 \times 10^{-8}$
Imag(Error)	0

### A.3 Computation Time Comparison

If speed is a consideration, and the application can tolerate the anticipated error, delay by the fractional phase shift method, including a correction to eliminate the imaginary portion of the result, should be considered. The interpolation method requires repeated computation of the `sinc()` function, which, for a large number of samples in the signal or desired points of interpolation, can be computationally intensive. The phase shift method requires computation of the FFT and IFFT. A comparison of the times required for the above evaluation is provided in Table A.5. While this is just a small data set for a single signal, it is clear that the interpolation requires considerably more time to compute than the delays via phase shift in the frequency domain. Little more should be extracted from this data, given the minimal number of runs to evaluate performance.

### A.4 Summary

When shifting an integer number of time-domain samples, a circular shift operation (e.g. using `circshift()` in MATLAB) is a straightforward option, as this simply involves adjusting the index numbers of the sampled data and should yield minimal, if not zero, error.

Table A.5. Calculation times for various shifting methods.

	Calculation time (ms)
Circular Shift	3.3
Interpolation (integer)	355.2
Interpolation (fractional)	358.2
Phase Shift (integer)	1.7
Phase Shift (fractional)	2.0
Phase Shift (fractional w/ correction)	4.4

For fractional shifts, options include either interpolation at the delayed time or use of a fractional phase shift in the frequency domain. As discussed above, there is some error between those two methods, and while a true “control” for that error is not available, it is reasonable to attribute the discrepancy to the fractional phase shift method, as it involves a departure from the typical case while interpolation accuracy should not be affected by the times at which the signal is interpolated. Depending upon the application, computation time might be a considerable argument for use of the delay via phase shift in the frequency domain.

THIS PAGE INTENTIONALLY LEFT BLANK

---

## APPENDIX B:

### Additional Analysis Tables and Figures

---

#### B.1 OFDM Signal Recovery

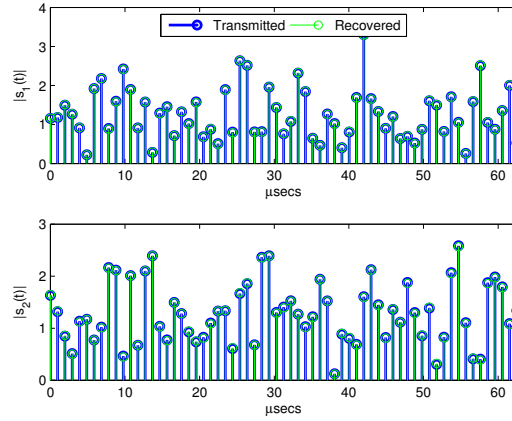


Figure B.1. OFDM test signal, time domain, parameter set 1.

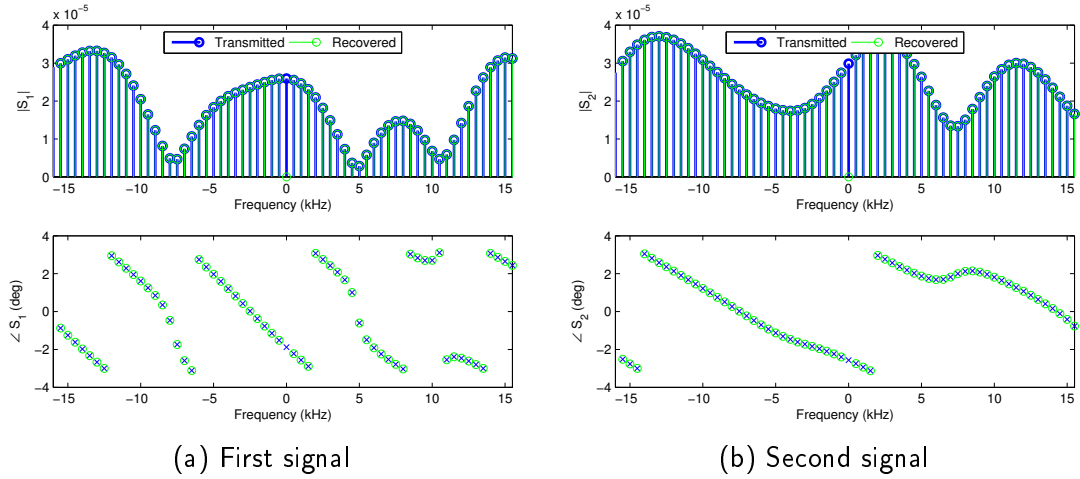
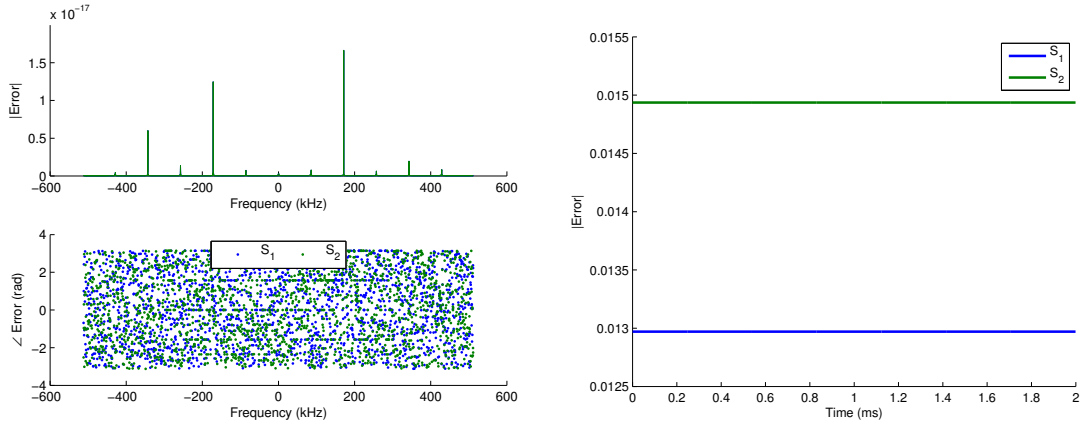


Figure B.2. Frequency domain of OFDM test transmitted and recovered signals, parameter set 1.





(a) Frequency domain (b) Time domain  
Figure B.3. Error of recovered OFDM signals, parameter set 1.

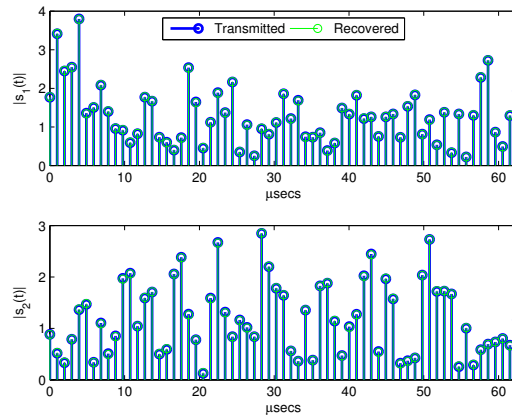
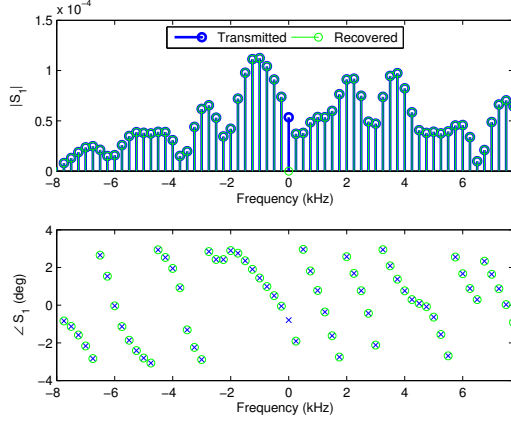
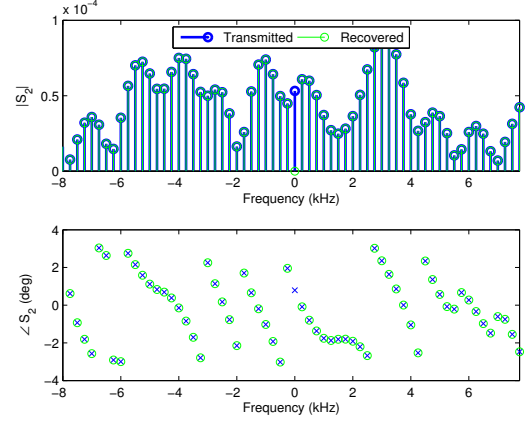


Figure B.4. OFDM test signal, time domain, parameter set 2.

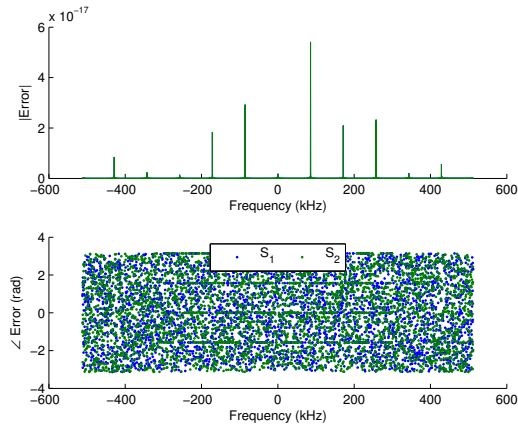


(a) First signal

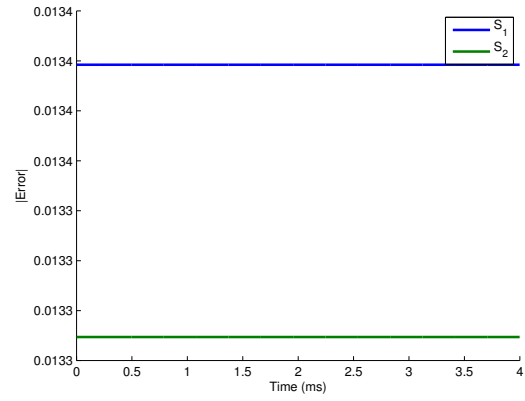


(b) Second signal

Figure B.5. Frequency domain of OFDM test transmitted and recovered signals, parameter set 2.



(a) Frequency domain



(b) Time domain

Figure B.6. Error of recovered OFDM signals, parameter set 2.

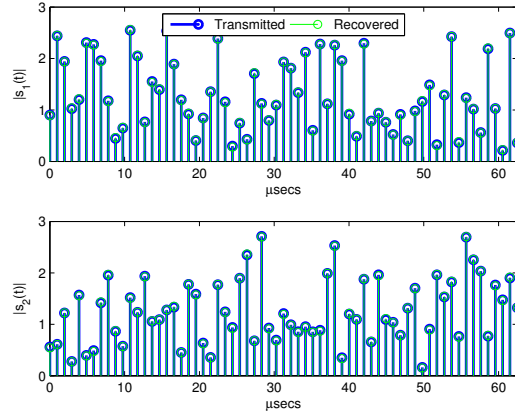
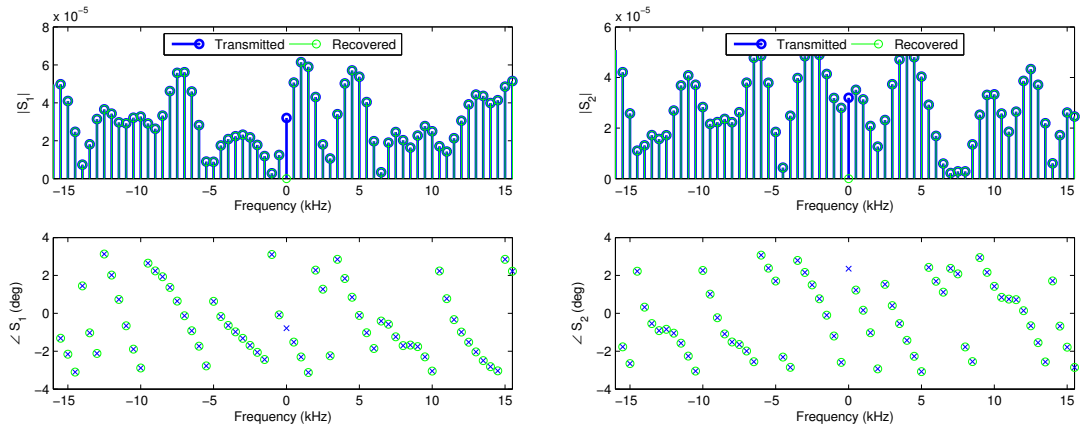


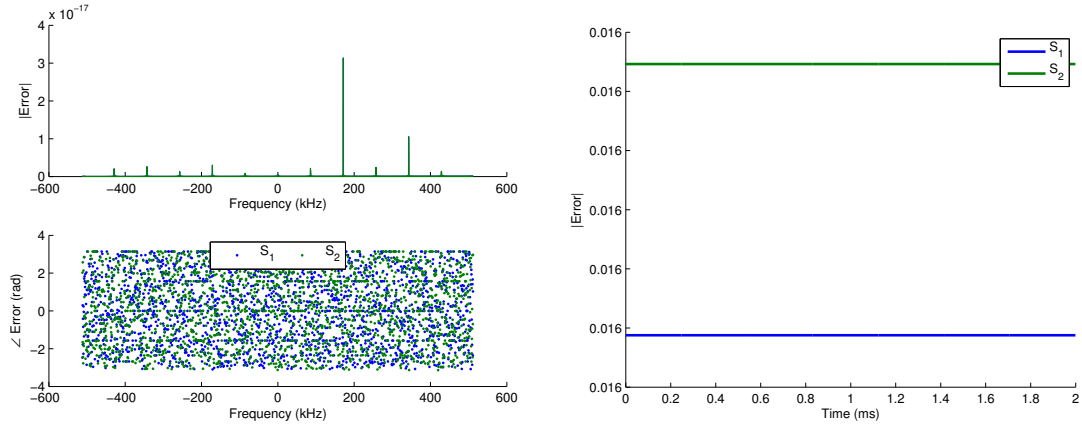
Figure B.7. OFDM test signal, time domain, parameter set 3.



(a) First signal

(b) Second signal

Figure B.8. Frequency domain of OFDM test transmitted and recovered signals, parameter set 3.



(a) Frequency domain (b) Time domain  
Figure B.9. Error of recovered OFDM signals, parameter set 3.

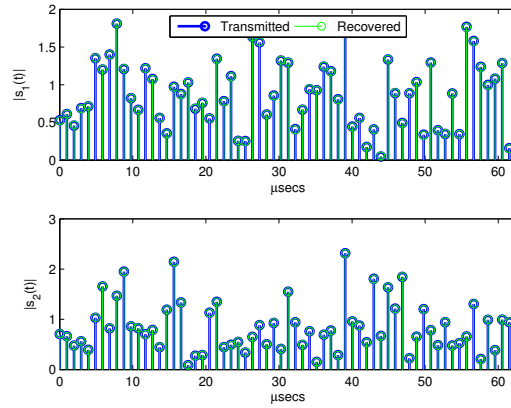
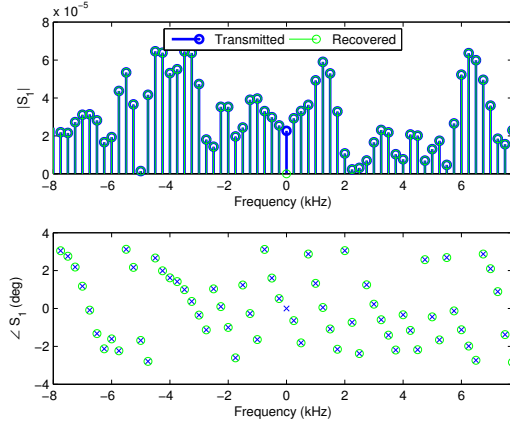
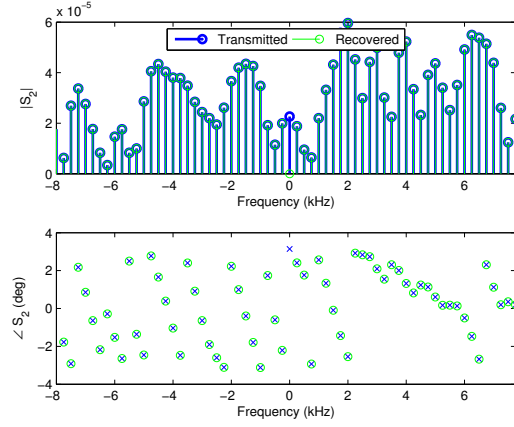


Figure B.10. OFDM test signal, time domain, parameter set 4.

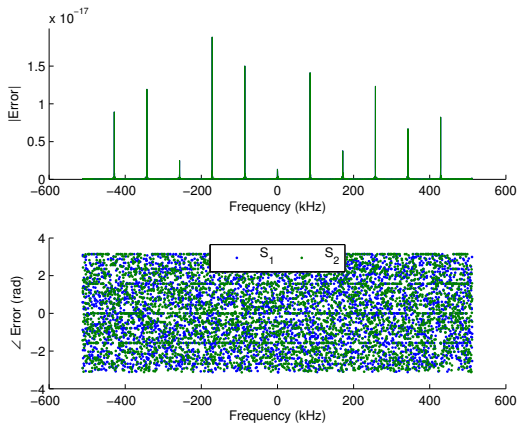


(a) First signal

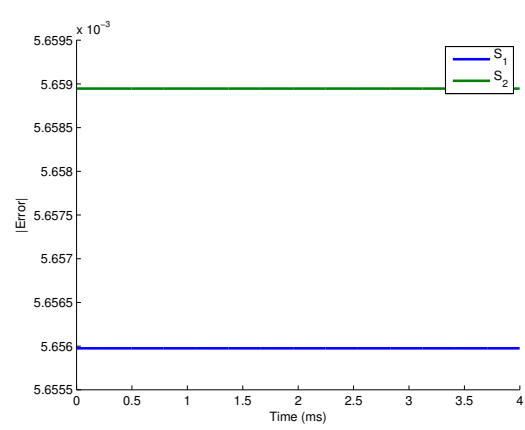


(b) Second signal

Figure B.11. Frequency domain of OFDM test transmitted and recovered signals, parameter set 4.



(a) Frequency domain



(b) Time domain

Figure B.12. Error of recovered OFDM signals, parameter set 4.

## B.2 Geometry Analysis

Table B.1. Recovery performance figures for layout 1.

	Signal 1	Signal 2
Power Angle ( $^{\circ}$ )	39.17	48.65
Error Figure	$0.002572 - 9.5719 \times 10^{-29}i$	$0.001851 + 9.2041 \times 10^{-29}i$
Subspace Angle ( $^{\circ}$ )	$2.907 + 3.0395 \times 10^{-14}i$	$2.466 + 3.3244 \times 10^{-13}i$
Correlation	$0.9987 - 2.6904 \times 10^{-17}i$	$0.9991 - 2.496 \times 10^{-16}i$

Table B.2. Recovery performance figures for layout 2.

	Signal 1	Signal 2
Power Angle ( $^{\circ}$ )	39.11	48.65
Error Figure	$0.001286 - 3.2622 \times 10^{-28}i$	$0.0009253 + 1.4881 \times 10^{-28}i$
Subspace Angle ( $^{\circ}$ )	$2.055 - 3.1089 \times 10^{-13}i$	$1.743 + 1.4709 \times 10^{-12}i$
Correlation	$0.9994 + 1.9458 \times 10^{-16}i$	$0.9995 - 7.809 \times 10^{-16}i$

Table B.3. Recovery performance figures for layout 3.

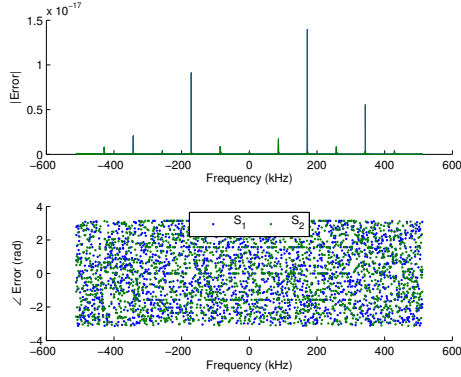
	Signal 1	Signal 2
Power Angle ( $^{\circ}$ )	39.11	48.65
Error Figure	$0.001286 - 2.6708 \times 10^{-28}i$	$0.0009253 + 6.2858 \times 10^{-28}i$
Subspace Angle ( $^{\circ}$ )	$2.055 + 1.1063 \times 10^{-13}i$	$1.743 + 9.6102 \times 10^{-13}i$
Correlation	$0.9994 - 6.9239 \times 10^{-17}i$	$0.9995 - 5.1021 \times 10^{-16}i$

Table B.4. Recovery performance figures for layout 4.

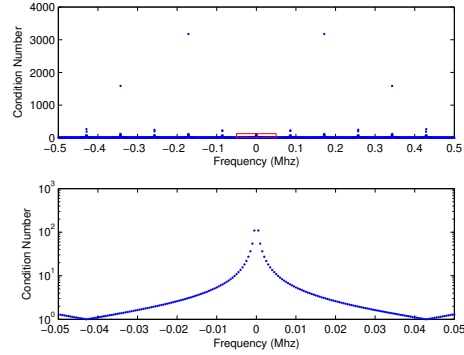
	Signal 1	Signal 2
Power Angle ( $^{\circ}$ )	39.11	48.65
Error Figure	$0.001286 - 2.9969 \times 10^{-30}i$	$0.0009253 + 2.2486 \times 10^{-29}i$
Subspace Angle ( $^{\circ}$ )	$2.055 + 4.6904 \times 10^{-14}i$	$1.743 - 2.3755 \times 10^{-13}i$
Correlation	$0.9994 - 2.9356 \times 10^{-17}i$	$0.9995 + 1.2612 \times 10^{-16}i$

Table B.5. Recovery performance figures for layout 5.

	Signal 1	Signal 2
Power Angle ( $^{\circ}$ )	39.17	48.65
Error Figure	$0.002572 + 5.2147 \times 10^{-23}i$	$0.001851 - 3.0583 \times 10^{-21}i$
Subspace Angle ( $^{\circ}$ )	$2.907 + 2.5224 \times 10^{-9}i$	$2.466 - 8.7371 \times 10^{-10}i$
Correlation	$0.9987 - 2.2326 \times 10^{-12}i$	$0.9991 + 6.5599 \times 10^{-13}i$

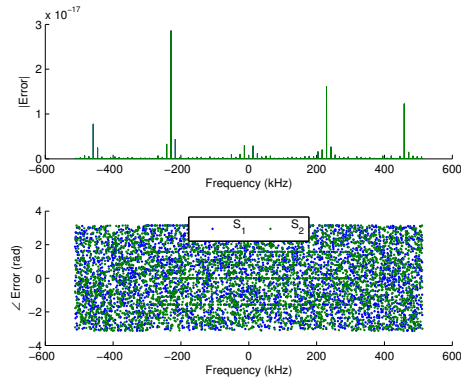


(a) Frequency-domain error

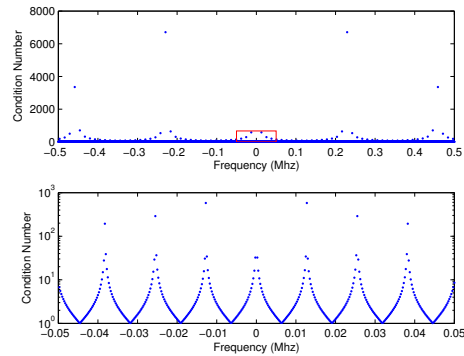


(b) Condition number

Figure B.13. Geometry induced recovery errors, layout 1.

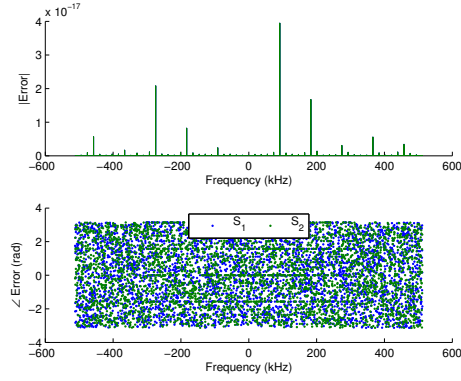


(a) Frequency-domain error

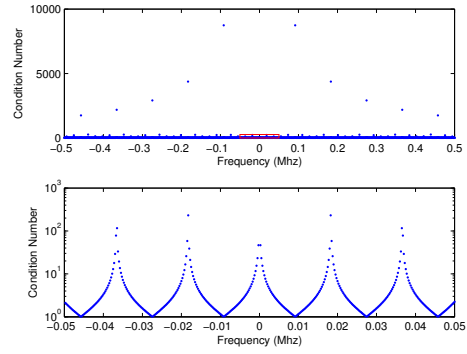


(b) Condition number

Figure B.14. Geometry induced recovery errors, layout 2.

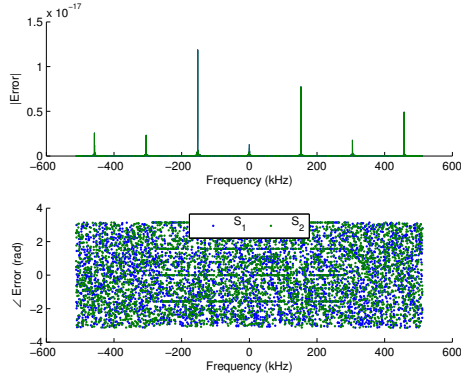


(a) Frequency-domain error

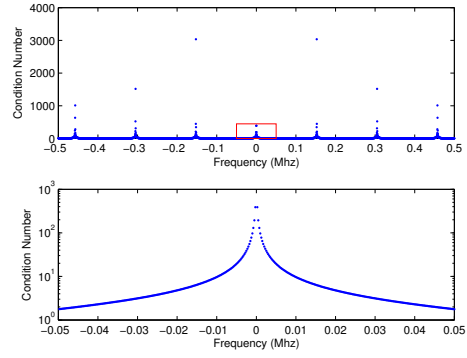


(b) Condition number

Figure B.15. Geometry induced recovery errors, layout 3.

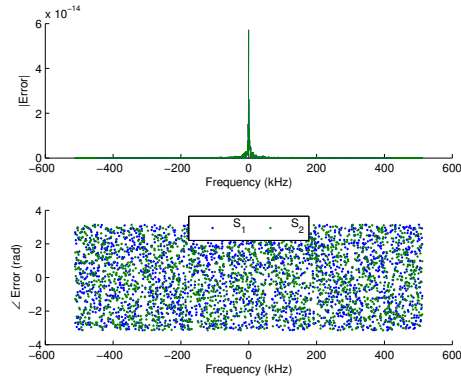


(a) Frequency-domain error

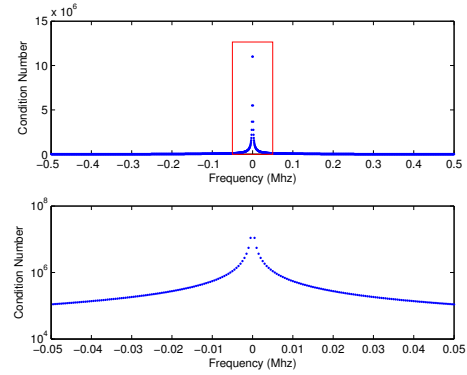


(b) Condition number

Figure B.16. Geometry induced recovery errors, layout 4.



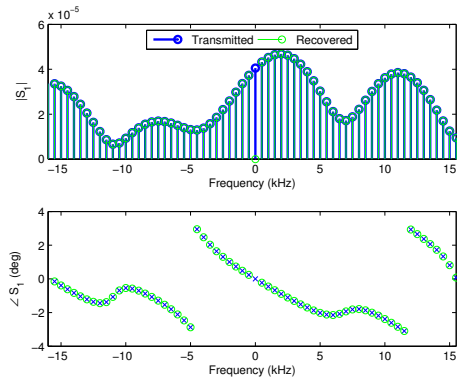
(a) Frequency-domain error



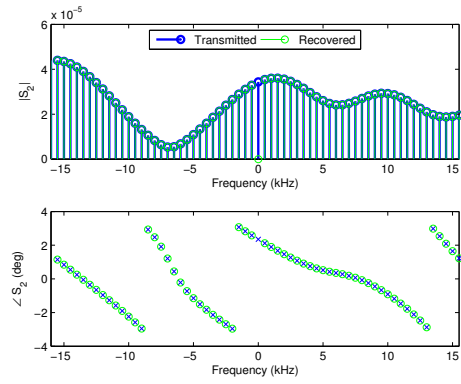
(b) Condition number

Figure B.17. Geometry induced recovery errors, layout 5.



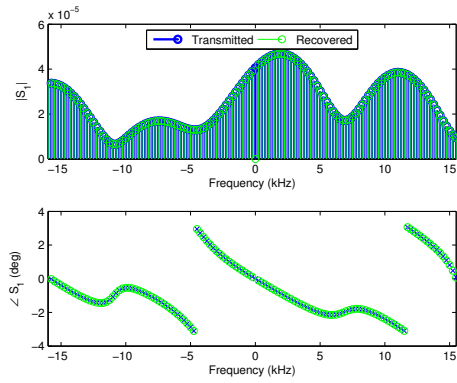


(a) First signal

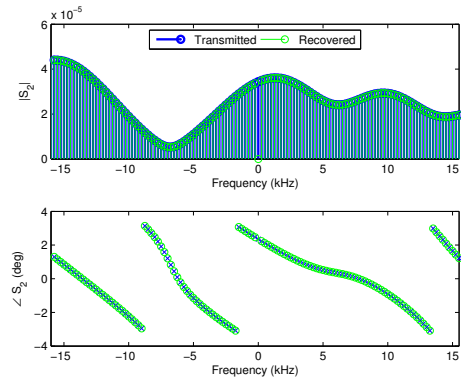


(b) Second signal

Figure B.18. Frequency domain of recovered signals, layout 1.

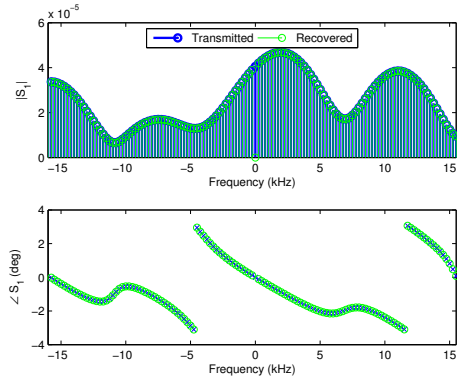


(a) First signal

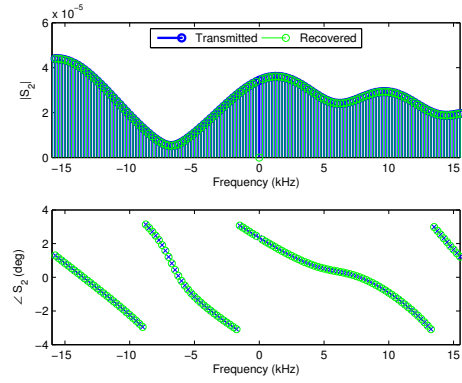


(b) Second signal

Figure B.19. Frequency domain of recovered signals, layout 2.

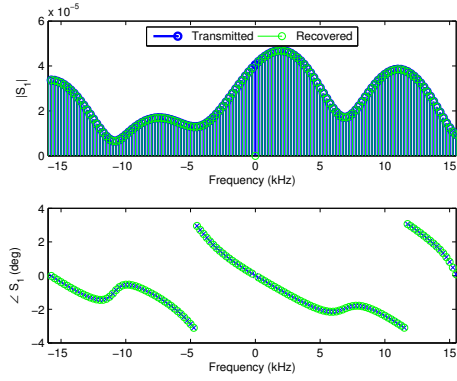


(a) First signal

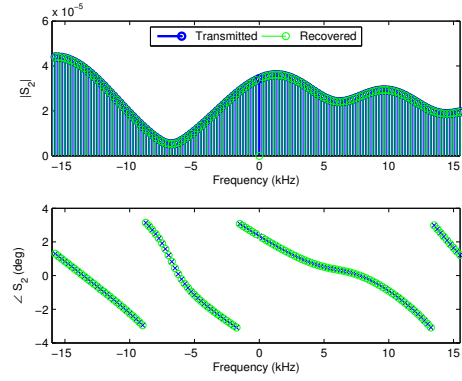


(b) Second signal

Figure B.20. Frequency domain of recovered signals, layout 3.

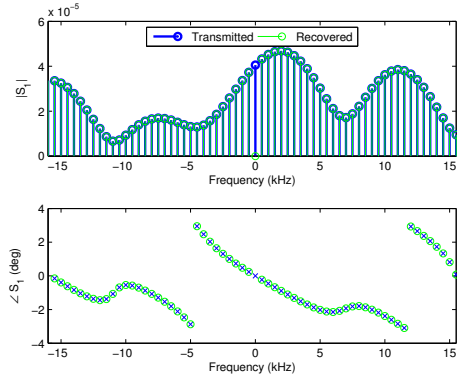


(a) First signal

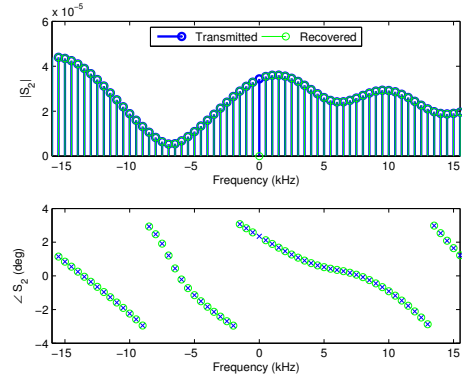


(b) Second signal

Figure B.21. Frequency domain of recovered signals, layout 4.

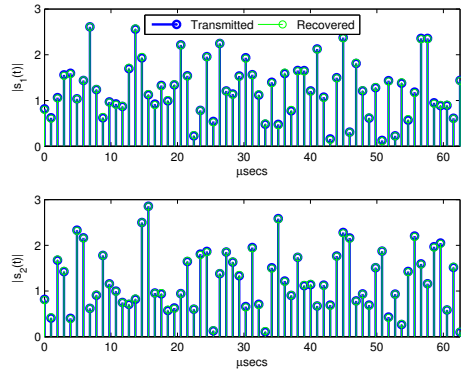


(a) First signal

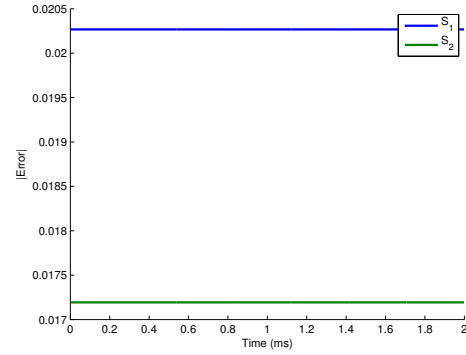


(b) Second signal

Figure B.22. Frequency domain of recovered signals, layout 5.

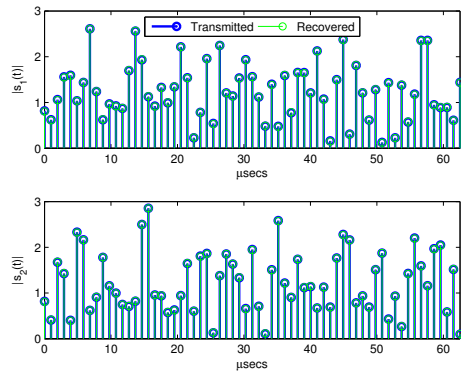


(a) Time-domain signals

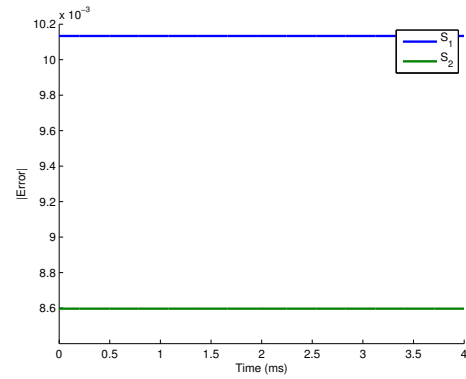


(b) Time-domain error

Figure B.23. Time-domain signals and error, layout 1.

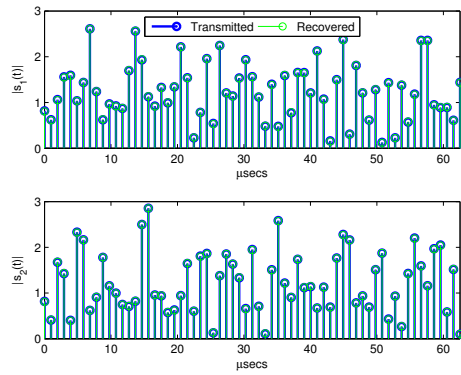


(a) Time-domain signals

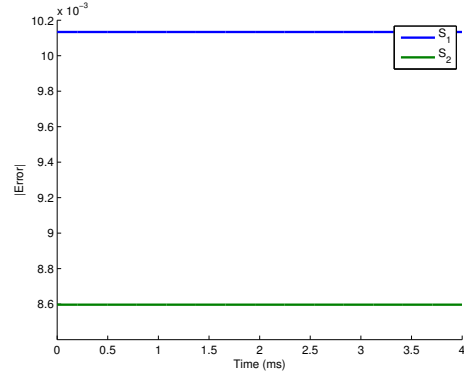


(b) Time-domain error

Figure B.24. Time-domain signals and error, layout 2.

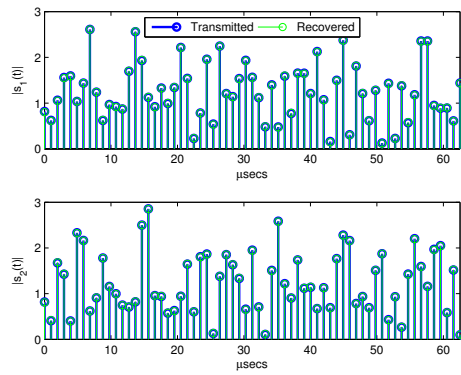


(a) Time-domain signals

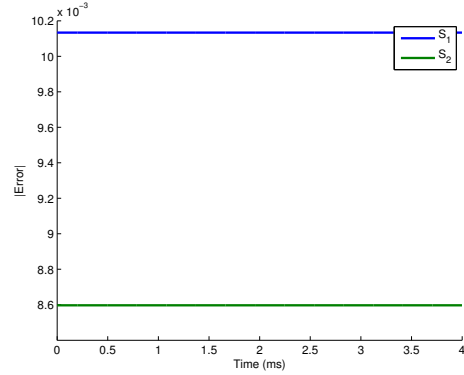


(b) Time-domain error

Figure B.25. Time-domain signals and error, layout 3.

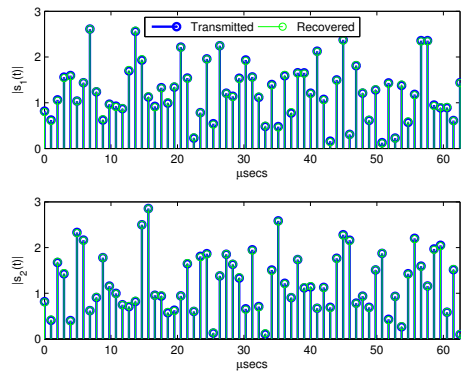


(a) Time-domain signals

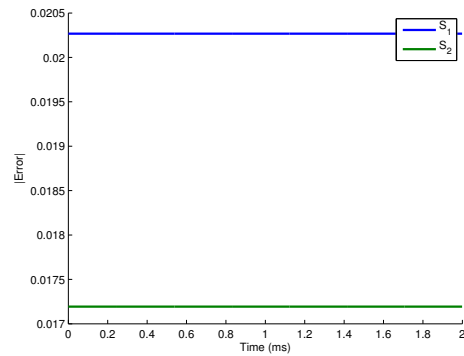


(b) Time-domain error

Figure B.26. Time-domain signals and error, layout 4.



(a) Time-domain signals



(b) Time-domain error

Figure B.27. Time-domain signals and error, layout 5.

THIS PAGE INTENTIONALLY LEFT BLANK

---

## APPENDIX C:

### Code Listings

---

#### C.1 delays\_from\_laydown.m

```
1 function [ tau ] = delays_from_laydown( L )
2 % DELAYS_FROM_LAYDOWN Compute the delay matrix TAU from laydown L
3 %   Compute signal delays from a set of transmitters to a set of
4 %   receivers, with geometric laydown as specified in L.
5
6 Re = 6371e3; % m
7
8 num.recv = length(L.r.x);
9 num.xmit = length(L.t.x);
10
11 % loop to compute all elements
12 for m = 1:num.recv
13     for n = 1:num.xmit
14         theta = (L.r.x(m) - L.t.x(n)) / Re * 180/pi;
15
16         % Law of cosines to get from theta to d(1,1)
17         dx = sqrt( (L.r.alt(m)+Re)^2 + Re^2 - ...
18                 2*(L.r.alt(m)+Re)*Re*cosd(theta) );
19         d(m,n) = dx / cos(atan2(L.r.y(m)-L.t.y(n),dx));
20     end
21 end
22
23 % Convert from distance to time, using an approximation of the speed of
24 % light
25 tau = d ./ 3e8;
26
27 end
```

#### C.2 block\_deltas\_from\_delays.m

---

```

1 function [ D, cond_num ] = block_deltas_from_delays( tau, omega )
2 %BLOCK_DELTAS_FROM_DELAYS Build the block diagonal matrix of delays
3 % [D, cond_num] = BLOCK_DELTAS_FROM_DELAYS returns the block diagonal
4 % delay matrix using the propagation delays found in TAU and the
5 % frequencies from OMEGA.
6 %
7 % The condition number matrix allows checking for degenerate cases
8
9 [num.recv, num.xmit] = size(tau);
10 N = length(omega);
11
12 D = exp( -1j .* reshape(tau,[num.xmit*num.recv 1]) * omega);
13 D = num2cell(reshape(D, [num.recv num.xmit N]), [1 2]);
14 cond_num = squeeze(cellfun(@cond,D));
15 D = blkdiag(D{:});
16
17 end

```

### C.3 calc\_signals\_nb.m

```

1 function [ s, r ] = calc_signals_nb( signal_spec, t, tau )
2 %CALC_SIGNALS_NB Calculate sampled narrowband xmit and recv signals
3 %
4
5 [num.recv, num.xmit] = size(tau);
6 N = length(t);
7 dt = t(2);
8
9 % Only want to preserve the fundamental freqs and magnitudes
10 s = struct('mag', signal_spec.mag, 'f', signal_spec.f);
11
12 for n = 1:num.xmit
13     s.func{n} = @(t) (s.mag(n)*cos(2*pi*s.f(n)*t));
14     s.time(n,:) = s.func{n}(t);
15     s.freq(n,:) = fft(s.func{n}(t))*dt;
16 end
17
18

```

```

19 % Received signals - "r"
20 r.time = zeros(num.recv,N);
21 for m = 1:num.recv
22     for n = 1:num.xmit
23         r.time(m,:) = r.time(m,:) + s.func{n}(t - tau(m,n));
24     end
25 end
26 r.sig_power = sum(r.time.^2,2)/N;
27
28 end

```

## C.4 recover\_from\_delays.m

```

1 function [ s_recovered ] = recover_from_delays( num, D, sig_freq, dt, ...
2     error_check)
3 %RECOVER_FROM_DELAYS Use signal delay to recover original signal
4 %
5 %   Recover the original signals from a set of co-channel signals
6 %   received at a separated set of receivers, given the known delays
7 %   between the transmitters and receivers.
8 %
9 %   s_recovered = recover_from_delays( num, D, sig_freq, dt,
10 %   error_check ) returns the original signals in s_recovered. D is a
11 %   mN x nN matrix of the signal delays where m is the number of
12 %   receivers, n is the number of transmitters, and N is the number of
13 %   discrete frequencies. sig_freq is the matrix of frequency
14 %   samples, generally the result of fft(time_domain_samples). dt is
15 %   the sampling interval in the time domain and error_check is a
16 %   boolean that controls an extra level of error checking in the
17 %   recovery process, useful for understanding errors at discrete
18 %   frequencies due to poorly conditioned blocks in the D matrix.
19
20 N = length(sig_freq);
21
22 R = reshape(sig_freq, [num.recv*N,1]);
23
24 % remove the rows and columns that correspond to omega(1) = 0
25 D = D(num.recv+1:end,num.xmit+1:end);

```



```

26 R = R(num.recv+1:end);
27
28 % preallocate S for speed and proper dimension,
29 % necessary to account for the missing elements per above
30 S = zeros(num.xmit*(N-1), 1);
31
32 if error_check
33     % cycle through the blocks to ensure independent calculation
34     % there are N-1 blocks, after the removal completed above
35     for blk_num = 1:N-1
36         index = 2*(blk_num-1) + (1:num.xmit);
37         if cond(D(index,index)) > 300
38             fprintf('Bad condition number at indices: [%d %d]\n', ...
39                 index+num.xmit) %adjust for missing block
40             disp(D(index,index))
41         end
42         S(index) = D(index,index) \ R(index);
43     end
44
45     if (~all(D * S - R < eps) | ~all(D \ R - S < eps))
46         warning('Recovery had errors greater than epsilon.')
47     end
48 else
49     S = D \ R;
50 end
51
52 S = reshape(S, num.xmit, []);
53
54 % Insert zeros for the known singularity at f=0 and return to time domain
55 s_recovered.freq = [zeros(num.xmit,1) S];
56 s_recovered.time = ifft(s_recovered.freq, [], 2)/dt;
57 s_recovered.sig_power = diag(s_recovered.time * s_recovered.time') / N;
58 s_recovered.N = length(s_recovered.time);
59 end

```

## C.5 calc\_signals\_wb.m

```

1 function [ s, r ] = calc_signals_wb( signal_spec, tau )

```

```

2 % CALC_SIGNALS_WB Calculate sampled wideband transmit and receive
3 % signals
4 % [ s, r ] = CALC_SIGNALS_WB(SIGNAL_SPEC, TAU) returns the
5 % transmitted (S) and received (R) signals, with delays specified by
6 % TAU incorporated in the received signals.
7 %
8 % SIGNAL_SPEC is a structure that includes SIGNAL_SPEC.TYPE, which
9 % may be either 'noise' or 'impulse' for a AWGN signal, or a time
10 % domain impulse, which has a constant response in the frequency
11 % domain. The impulse is useful when testing. SIGNAL_SPEC.N is the
12 % number of points, and SIGNAL_SPEC.dt is the inter-sample interval,
13 % or 1/Fs.
14 %
15 % CALC_SIGNALS_WB() with SIGNAL_SPEC.TYPE = 'noise' returns a signal
16 % with power spectral density equal to 1.
17 %
18 % If defined, SIGNAL_SPEC.RNG_STATE is used to set the state of the
19 % RNG prior to signal generation. This ensures consistent signal
20 % contents across multiple calls to CALC_SIGNALS_WB().
21
22 s = signal_spec;
23 dt = signal_spec.dt;
24
25 % Use a seed for the RNG, if requested — keeps signal contents
26 % constant
27 if isfield(signal_spec, 'rng_state')
28     rng(signal_spec.rng_state)
29 end
30
31 [num.recv, num.xmit] = size(tau);
32 buffer_len = ceil(max(reshape(tau, [num.recv*num.xmit 1])) / dt);
33
34 %%
35
36 for n = 1:num.xmit
37     switch(lower(signal_spec.type))
38         case 'noise'
39             N = signal_spec.N;
40             N_hat = 2.^nextpow2(N+buffer_len);

```

```

41         s.time(n,:) = randn(1,N);
42         s.freq(n,:) = fft(s.time(n,:), N_hat, 2)*dt;
43
44     case 'impulse'
45         N = signal_spec.N;
46         N_hat = 2.^nextpow2(N+buffer_len);
47         s.freq(n,:) = ones(1,N_hat);
48         s.time(n,:) = ifft(s.freq(n,:), N_hat, 2)/dt;
49
50     case 'ofdm'
51         signal = ofdm_signal(s.ofdmParams{:});
52
53         % The OFDM signal needs to be interpolated dt time domain
54         N = ceil(signal.duration / dt); % new number of samples
55         N_hat = 2.^nextpow2(N+buffer_len);
56         t = (0:N_hat-1)*dt; % new time domain, based on dt
57         s.time(n,:) = interp_time(t, signal.sig, signal.Tsamp);
58         s.freq(n,:) = fft(s.time(n,:), N_hat, 2)*dt;
59     end
60 end
61
62 df_hat = 1 / (N_hat*dt);
63 fprintf('s.time energy: %f\t%f\n', diag(s.time * s.time')*dt)
64 fprintf('s.freq energy: %f\t%f\n', diag(s.freq * s.freq')*df_hat)
65
66 %%
67 % create a new omega vector for the longer time vector
68 k = (0:N_hat-1) - N_hat/2;
69 omega = fftshift(2*pi*k / (N_hat*dt));
70
71 %%
72 % Delayed signals (as though received independently at the receivers)
73 for m = 1:num.recv
74     for n = 1:num.xmit
75         delayed.freq(m,n,:) = s.freq(n,:) .* exp(-1j*omega*tau(m,n));
76     end
77 end
78 delayed.time = ifft(delayed.freq, N_hat, 3)/dt;
79

```

```

80 for m = 1:num.recv
81     for n = 1:num.xmit
82         del.t = squeeze(delayed.time(m,n,:));
83         del.f = squeeze(delayed.freq(m,n,:));
84         fprintf('delayed.time(%d,%d) energy: %g\n', ...
85             m,n,diag(del.t' * del.t)*dt)
86         fprintf('delayed.freq(%d,%d) energy: %g\n', ...
87             m,n,diag(del.f' * del.f)*df_hat)
88     end
89 end
90
91 %%
92 for m = 1:num.recv
93     for n = 1:num.xmit
94         corr_plot(s.time(n,:), ...
95             permute(squeeze(delayed.time(m,n,:)), [2 1]));
96     end
97 end
98
99 %%
100 % Received signals - "r"
101 r.time = zeros(num.recv,N_hat);
102 for m = 1:num.recv
103     for n = 1:num.xmit
104         r.time(m,:) = r.time(m,:) + ...
105             permute(squeeze(delayed.time(m,n,:)), [2 1]);
106     end
107 end
108 %r.time = r.time(:,1:N);
109 r.freq = fft(r.time, N_hat, 2)*dt;
110
111 fprintf('r.time energy: %f\t%f\n', diag(r.time * r.time')*dt)
112 fprintf('r.freq energy: %f\t%f\n', diag(r.freq * r.freq')*df_hat)
113
114
115 %%
116 % Signal powers
117 s.sig_power = diag(s.time * s.time') /N_hat;
118 r.sig_power = diag(r.time * r.time') /N;

```

```
119
120 end
```

## C.6 interp\_time.m

```
1 function output = interp_time( t, x, Tsamp )
2 % INTERP_TIME Interpolate using the ideal low pass filter.
3 %   INTERP_TIME( t0, x, Tsamp ) returns an interpolated estimate of
4 %   x(t0) where t0 is the time of the desired point for interpolation,
5 %   x contains samples of the function x() such that x[n] = x(n*Tsamp)
6 %   and Tsamp is the sampling interval.
7 %
8 %   INTERP_TIME( t, x, Tsamp ) returns a column vector of interpolated
9 %   values, where interpolation is performed at times specified in t.
10 %
11 %   Authored by Ned Patterson
12
13 n = 0:length(x)-1;
14 n = ones(length(t),1) * n;
15 t = reshape(t, [], 1); % Ensure that t is a column vector
16 t = t * ones(1, length(x));
17
18 % Assume we have sampled at the nyquist rate
19 B = 1/(2*Tsamp);
20
21 h = sinc( t/Tsamp - n );
22 x = reshape(x, [], 1); % Ensure that x is a column
23
24 % Compute the sum of the product using the inner product
25 output = h * x;
```

---

## List of References

---

- [1] American Society for Photogrammetry and Remote Sensing, *Manual of Remote Sensing*, 3rd ed., R. A. Ryerson, Ed. New York: J. Wiley, 1998.
- [2] M. Soumekh, *Synthetic Aperture Radar Signal Processing with MATLAB Algorithms*. New York: J. Wiley, 1999.
- [3] M. I. Skolnik, *Radar Handbook*, 3rd ed. New York: McGraw-Hill, 2008.
- [4] J. R. Gutierrez del Arroyo, "Passive synthetic aperture radar imaging using commercial OFDM communication networks," Ph.D. dissertation, Graduate School Eng. Manage., Air Force Inst. Technology, Wright-Patterson Air Force Base, OH, 2012. [Online]. Available: <http://oai.dtic.mil/oai/oai?verb=getRecord&metadataPrefix=html&identifier=ADA564648>
- [5] N. J. Willis, *Bistatic Radar*. Silver Spring, MD: Technology Service Corp., 1995.
- [6] J. R. Gutierrez del Arroyo and J. A. Jackson, "Collecting and processing WiMAX ground returns for SAR imaging," in *2013 IEEE Radar Conference*. Ottawa, ON: IEEE, 2013, pp. 1–6. [Online]. Available: [http://ieeexplore.ieee.org/xpls/abs\\_all.jsp?arnumber=6586157](http://ieeexplore.ieee.org/xpls/abs_all.jsp?arnumber=6586157)
- [7] "IEEE Standard for Air Interface for Broadband Wireless Access Systems," *IEEE Std. 802.16*, 2012. [Online]. Available: <http://ieeexplore.ieee.org/servlet/opac?punumber=6272297>
- [8] "Long term evolution (LTE): A technical overview," Motorola, Inc., Technical White Paper, 2007. [Online]. Available: [http://www.motorola.com/mcne/TechDocs/LTE\\_Technical.pdf](http://www.motorola.com/mcne/TechDocs/LTE_Technical.pdf)
- [9] J. R. Gutierrez Del Arroyo and J. A. Jackson, "WiMAX OFDM for passive SAR ground imaging," *IEEE Trans. Aerosp. Electron. Syst.*, vol. 49, no. 2, pp. 945–959, 2013. [Online]. Available: [http://ieeexplore.ieee.org/xpls/abs\\_all.jsp?arnumber=6494391](http://ieeexplore.ieee.org/xpls/abs_all.jsp?arnumber=6494391)
- [10] N. Levanon and E. Mozeson, *Radar Signals*. Hoboken, NJ: John Wiley & Sons, Inc., 2004. [Online]. Available: <http://dx.doi.org/10.1002/0471663085>
- [11] J. Eberspächer, H.-J. Vögel, C. Bettstetter, and C. Hartmann, *GSM– Architecture, Protocols and Services*. Chichester, UK: John Wiley & Sons, Ltd, Dec. 2008. [Online]. Available: <http://doi.wiley.com/10.1002/9780470741719>

- [12] A. B. Carlson, *Communication Systems: An Introduction to Signals and Noise in Electrical Communication*, 5th ed. Boston: McGraw-Hill, 2010.
- [13] J. V. Stone, *Independent Component Analysis: A Tutorial Introduction*. Cambridge, Mass: MIT Press, 2004.
- [14] S. T. Roweis, "One microphone source separation," 2000. [Online]. Available: <http://www.ece.uvic.ca/~bctill/papers/singchan/onemic.pdf>
- [15] S. C. Douglas, "Fixed-point algorithms for the blind separation of arbitrary complex-valued non-gaussian signal mixtures," *EURASIP J. Advances Signal Process.*, 2007.
- [16] L. G. T. Corporation, "CBSS Toolbox," 2010.
- [17] B. J. Fason, "Modeling and simulation of synthetic aperture radars in MATLAB," M.S. Thesis, Dept. Elec. and Comp. Eng., Naval Postgraduate School, Monterey, CA, 2013. [Online]. Available: <http://calhoun.nps.edu/public/handle/10945/34661>
- [18] S. A. Holder, "Linear frequency modulated signals VS orthogonal frequency division multiplexing signals for synthetic aperture radar systems," M.S. Thesis, Dept. Elec. and Comp. Eng., Naval Postgraduate School, Monterey, CA, 2014. [Online]. Available: <http://oai.dtic.mil/oai/oai?verb=getRecord&metadataPrefix=html&identifier=ADA608045>
- [19] A. V. Oppenheim, *Signals and Systems*. Englewood Cliffs, N.J: Prentice-Hall, 1983.
- [20] A. Papoulis, *Probability, Random Variables, and Stochastic Processes*, 2nd ed. New York: McGraw-Hill, 1984.
- [21] R. D. Strum, *First Principles of Discrete Systems and Digital Signal Processing*. Reading, Mass: Addison-Wesley, 1988.
- [22] "LTE; Evolved Universal Terrestrial Radio Access (E-UTRA); Physical channels and modulation," *3GPP TS 36.211 version 12.3.0*, Oct. 2014. [Online]. Available: [http://www.etsi.org/deliver/etsi\\_ts/136200\\_136299/136211/12.03.00\\_60/ts\\_136211v120300p.pdf](http://www.etsi.org/deliver/etsi_ts/136200_136299/136211/12.03.00_60/ts_136211v120300p.pdf)
- [23] G. Strang, *Introduction to Linear Algebra*. Wellesely, MA: Wellesley-Cambridge Press, 2003.
- [24] L. N. Trefethen, *Numerical Linear Algebra*. Philadelphia: Society for Industrial and Applied Mathematics, 1997.
- [25] B. Sklar, *Digital Communications: Fundamentals and Applications*, 2nd ed. Upper Saddle River, N.J: Prentice-Hall PTR, 2001.

---

## Initial Distribution List

---

1. Defense Technical Information Center  
Ft. Belvoir, Virginia
2. Dudley Knox Library  
Naval Postgraduate School  
Monterey, California